

Doctoral Thesis in Physics

Ferrimagnetic Heusler Compounds

From first principles to thin films

Markus Meinert

October 2011

Bielefeld University
Department of Physics

This work was done by myself. Text and figures were partly taken from corresponding publications, which originate directly from this work.

(Markus Meinert)

Reviewers:

Prof. Dr. Günter Reiss

Prof. Dr. Jürgen Schnack

Copyright © 2011 Markus Meinert

Bielefeld University, Department of Physics

Thin Films and Physics of Nanostructures

Typeface Palladio and Pazo Math 10 pt.

System L^AT_EX 2_ε and KOMA-Script.

"What I cannot compute, I do not understand."

- adapted from Richard P. Feynman

Publications

Publications included in this thesis

- *Ab initio prediction of ferrimagnetism, exchange interactions and Curie temperatures in Mn_2TiZ Heusler compounds*
M. MEINERT, J.-M. SCHMALHORST, AND G. REISS
J. Phys. Condens. Matter **23**, 063001 (2011)
- *Exchange interactions and Curie temperatures of Mn_2CoZ compounds*
M. MEINERT, J.-M. SCHMALHORST, AND G. REISS
J. Phys. Condens. Matter **23**, 116005 (2011)
- *Electronic structure of fully epitaxial Co_2TiSn thin films*
M. MEINERT, J. SCHMALHORST, H. WULFMEIER, G. REISS,
E. ARENHOLZ, T. GRAF, AND C. FELSER
Physical Review B **83**, 064412 (2011)
- *Ferrimagnetism and disorder of epitaxial $Mn_{2-x}Co_xVAI$ Heusler compound thin films*
M. MEINERT, J.-M. SCHMALHORST, G. REISS, AND E. ARENHOLZ
J. Phys. D: Appl. Phys. **44**, 215003 (2011)
- *Itinerant and local magnetic moments in ferrimagnetic Mn_2CoGa thin films probed by x-ray magnetic linear dichroism: Experiment and ab initio theory*
M. MEINERT, J.-M. SCHMALHORST, C. KLEWE, G. REISS,
E. ARENHOLZ, T. BÖHNERT, K. NIELSCH
Physical Review B **84**, 132405 (2011)

Publications not included in this thesis

- *Influence of tetragonal distortion on the magnetic and electronic properties of the Heusler compound Co_2TiSn from first principles*
M. MEINERT, J.-M. SCHMALHORST, AND G. REISS
Appl. Phys. Lett. **97**, 012501 (2010)

Conference contributions

- *Electronic structure of fully epitaxial Co_2TiSn thin films*
M. MEINERT, J. SCHMALHORST, H. WULFMEIER, G. REISS,
E. ARENHOLZ, T. GRAF, AND C. FELSER
DPG Frühjahrstagung Dresden 2011, Talk, MA52.1
- *Ferrimagnetism and disorder in epitaxial $(\text{Mn}_{1-x}\text{Co}_x)_2\text{VAI}$ thin films*
M. MEINERT, J.-M. SCHMALHORST, G. REISS, AND E. ARENHOLZ
DPG Frühjahrstagung Dresden 2011, Poster, MA63.27
- *Magnetic Spectroscopy of Ferrimagnetic Heusler Compounds*
M. MEINERT, J. SCHMALHORST, G. REISS,
E. ARENHOLZ, R. LASKOWSKI
CECAM Workshop, X-ray Spectroscopy: Recent Advances
in Modelling and New Challenges, Zürich, Poster
- *Itinerant and localized Mn moments in ferrimagnetic Mn_2CoGa thin films identified with x-ray magnetic linear dichroism*
M. MEINERT, J.-M. SCHMALHORST, C. KLEWE, G. REISS,
E. ARENHOLZ, T. BÖHNERT, K. NIELSCH
56th Annual Conference on Magnetism & Magnetic Materials,
Scottsdale, Talk, DE-11

Contents

1	Introduction	9
2	Experimental Methods	14
2.1	Sample Preparation	14
2.2	Structural Characterization	15
2.3	Chemical Composition Analysis by X-Ray Fluorescence	18
2.4	Soft X-Ray Absorption Spectroscopy	20
2.5	Other Techniques	23
3	Theoretical Methods	24
3.1	Density Functional Theory	24
3.2	Implementations of DFT Used in This Work	30
3.3	Curie Temperatures from an Effective Heisenberg Model	35
3.4	X-Ray Absorption Spectra from Electronic Structure	37
4	Ferrimagnetism, exchange and Curie temperatures in Mn_2TiZ	43
4.1	Introduction	43
4.2	Results	45
5	Exchange and Curie temperatures of Mn_2CoZ compounds	56
5.1	Introduction	56
5.2	Results	57
6	Electronic structure of fully epitaxial Co_2TiSn thin films	66
6.1	Introduction	66
6.2	Experimental results	70
6.3	Electronic structure	81
7	Ferrimagnetism and disorder of epitaxial $Mn_{2-x}Co_xVAI$	85
7.1	Introduction	85
7.2	Methods	86
7.3	Experimental results and discussion	87

8 Itinerant and local magnetic moments in ferrimagnetic Mn₂CoGa	95
8.1 Introduction	95
8.2 Results	96
9 Concluding remarks	103
Bibliography	106
Acknowledgements	114

1 Introduction

The Heusler compounds are a class of intermetallic compounds with the general chemical formula X_2YZ , where X, Y are transition metals, and Z is a main group element. They crystallize by definition in the $L2_1$ structure (Fig. 1.1), a face centered cubic structure (space group $Fm\bar{3}m$) with a four atom basis. The coordinates of these four sites A, B, C , and D , are given by $A = (0, 0, 0)$, $B = (\frac{1}{4}, \frac{1}{4}, \frac{1}{4})$, $C = (\frac{2}{4}, \frac{2}{4}, \frac{2}{4})$, $D = (\frac{3}{4}, \frac{3}{4}, \frac{3}{4})$. The structure has inversion symmetry, making two sites (A and C) equivalent. These are occupied by the X element. In the Wyckoff notation, the A and C sites are named $8c$, and the other two sites are denoted as $4a, 4b$.

The prototype of the Heusler compounds is Cu_2MnAl , which was discovered by Friedrich Heusler in 1903 [1]. The compound, the crystal structure of which was determined by Bradley and Rodgers in 1934 [2], is a ferromagnet with a high Curie temperature, though none of its constituents is ferromagnetic by itself.

Today, we know more than 1000 Heusler compounds [3], which have a multitude of different properties. Most known quantum mechanical ground states

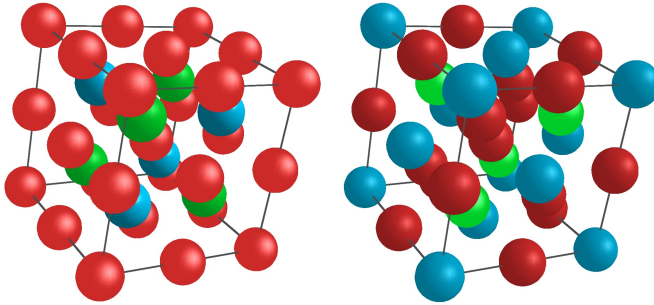


Figure 1.1: Left: Conventional (cubic) unit cell of the $L2_1$ (Heusler) structure. Right: Conventional (cubic) unit cell of the XA (inverse Heusler) structure. X sites are red, Y and Z sites are blue and green respectively.

of solids are represented within this class. Just to mention a few, there are ferromagnets (Cu_2MnAl [1]), ferrimagnets (Mn_2VAl [4]), semiconductors (Fe_2VAl [5]), heavy fermion systems (Cu_2CeIn [6]), and superconductors (Ni_2ZrGa [7]).

One particularly intriguing property, which is predicted for a number of magnetic Heusler compounds, is half-metallic ferro-/ferrimagnetism (HMF): for either the majority or minority density of states a gap is present around the Fermi energy. Thus, the material behaves metallic for one spin species, and semiconducting or insulating for the other one. The half-metallic ferromagnetism of a Heusler compound was first predicted by Kübler *et al.* for Co_2MnSi [8]. The Co_2 -based half-metallic Heusler compounds have a gap for the minority states. This property is particularly interesting for spin-electronic, or spintronic, applications, which make use of spin-polarized currents. These include in particular giant and tunnel magnetoresistive devices. The full spin polarization of the current carriers in a HMF gives rise to large magnetoresistive effects.

A half-metallic ferrimagnet has advantages over the well-known half-metallic ferromagnets: due to the internal spin compensation it has a rather low magnetic moment, while the Curie temperature remains fairly high. A low magnetic moment gives rise to low stray fields, which is desired for spintronics, as is a high Curie temperature and thus a good thermal stability of the compound [9]. The most prominent Heusler compound out of this class is Mn_2VAl , which has been studied thoroughly by experiment and theory [4, 10, 11, 12, 13]. Several other material classes have been proposed to be half-metallic ferrimagnets, e.g., $\text{Cr}_{0.75}\text{Mn}_{0.25}\text{Se}$ and $\text{Cr}_{0.75}\text{Mn}_{0.25}\text{Te}$ in the zinc blende structure [14], or Cr antisites in CrAs , CrSb , CrSe , and CrTe , having the zinc blende structure [15].

Ideally, an electrode material for spintronics would be a half-metal with zero net moment. This can not be achieved with antiferromagnets because of the spin-rotational symmetry (resulting in zero polarization), but well chosen half-metallic ferrimagnets can be tuned to zero moment. This property is also known as half-metallic antiferromagnetism, and has been first predicted for Mn and In doped FeVSb [16]. Among others, La_2VMnO_6 and related double perovskites [17] and certain diluted magnetic semiconductors have been later predicted to be half-metallic antiferromagnets as well [18]. However, half-metallic antiferromagnetism is limited to zero temperature and a small macroscopic net moment is expected at elevated temperature—in particular near the Curie temperature—because of the inequivalent magnetic sublattices [19].

Structure of this work

A major focus of this work is put on the direct comparison of theoretical and experimental properties of thin films of various ferrimagnetic Heusler compounds. Parts of this work are purely theoretical, aimed toward a basic understanding of the properties of ferrimagnetic Heusler compounds. Other parts combine experimental work and theoretical approaches to explain the data or to test predictions. The basic and most used experimental and theoretical methods are outlined in Chapters 2 and 3.

Predicting new ferrimagnetic Heusler compounds

A very interesting class of Heusler compounds that has received considerable theoretical, but only few experimental attention to date, are the half-metallic ferrimagnets Mn_2YZ , where $Y = V, Cr, Mn$ and Z is a group III, IV, or V element [20, 21, 22]. Following the Slater-Pauling rule connecting the magnetic moment m and the number of valence electrons N_V via $m = N_V - 24$ in the half-metallic Heusler compounds [23], it is expected to find another series of ferrimagnetic half-metals in the Mn_2TiZ system with -3 to $-1 \mu_B$ per formula unit (f.u.). The negative moment indicates that the half-metallic gap would appear for the *majority states*, just as in the case of Mn_2VAI . These compounds could—if they are half-metals—provide another series of potential electrodes for spin-dependent applications and could also become a starting point for half-metallic antiferromagnetism.

Chapter 4 discusses the properties of this newly predicted class of ferrimagnetic Heusler compounds.

Explaining the exchange interactions of inverse Heusler compounds

Closely related to the Heusler compounds are the so-called inverse Heusler compounds, which have a similar lattice structure (see Fig. 1.1), but miss the inversion symmetry (space group $F\bar{4}3m$, prototype Hg_2CuTi). Here, sites B and C are occupied by the same element. These compounds are Heusler compounds in a generalized sense, i.e., a face-centered cubic structure with the above given atomic positions. This occupation is preferred with respect to the Heusler structure if X has less valence electrons than Y [24, 25].

Recently, the Mn_2YZ inverse compounds have attracted considerable theoretical and experimental activities, where $Y = \text{Fe, Co, Ni, Cu}$ [25, 26, 27, 28, 29, 30, 31, 32, 33, 34, 35, 36, 37]. Half-metallic ferrimagnetism has been predicted for numerous compounds from this class [28]. The Mn_2YZ compounds also follow the Slater-Pauling rule connecting the magnetic moment m and the number of valence electrons N_V via $m = N_V - 24$ in half-metallic Heusler compounds [23].

The computed exchange interactions and associated properties of the Mn_2CoZ compounds are discussed in Chapter 5.

A weak cobalt-based ferrimagnet

The material class of Co_2YZ Heusler compounds has been the subject of extensive studies in the context of spintronics during the last decade. These compounds are of interest because many of them are predicted as half-metallic ferromagnets with full spin polarization at the Fermi edge.

The Heusler compound Co_2TiSn (CTS) is predicted to be a half-metallic ferrimagnet with a magnetic moment of $2 \mu_B/\text{f.u.}$ and it has a high formation energy of the Co-Ti site-swap defect [38, 39]. Usually, disorder destroys the half-metallicity. Hence, making use of Heusler compounds which exhibit low disorder or high tolerance of the ground state properties against disorder is highly desired.

In Chapter 6 the electronic structure of thin films of the weak ferrimagnet Co_2TiSn is discussed.

Achieving full magnetic compensation

Galanakis *et al.* pointed out that it may be possible to synthesize a HMF_i by substituting Co for Mn in the Heusler compound Mn_2VAI [40]. Mn_2VAI is a (potentially half-metallic) ferrimagnet with antiparallel coupling of Mn and V moments and a total moment of $-2 \mu_B$ per formula unit. The high Curie temperature of 760 K makes it interesting for practical applications. Numerous experimental [4, 10, 11, 41, 42] and theoretical [12, 13, 20, 43, 44] studies are found in the literature. Following the Slater-Pauling rule for Heusler compounds, $m = N_V - 24$ [23], the magnetic moment m is to be taken as negative, because the number of valence electrons N_V is 22. Thus, by adding effectively two electrons per unit cell, the magnetization should vanish. This can be achieved by substituting one Mn with one Co atom, which has two

additional electrons. *Ab initio* simulations were carried out on this system in the $L2_1$ structure with Mn and Co randomly spread across the Wyckoff 8c sites and V and Al on the 4a and 4b sites. Indeed, a HMF_i is found with magnetic moments of: -1.388 (Mn), 0.586 (Co), 0.782 (V), 0.019 (Al) [40]. It was shown by Luo *et al.* that the site occupation preference in Mn_2YAl depends on the number of valence electrons of Y: if it is lower than the one of Mn, Y would preferentially occupy the 4a/b sites, but if it is higher, Y would rather occupy the 8c sites together with Mn, changing the structure to the Hg_2CuTi type [45]. Accordingly, one can expect an occupation as proposed by Galanakis *et al.* in $Mn_{2-x}Co_xVAl$ (MCVA).

Chapter 7 focusses on the synthesis and characterization of thin films of the ferrimagnetic $Mn_{2-x}Co_xVAl$ system.

The first thin films of an inverse Heusler compound

To date, the inverse Heusler compounds were studied only in the bulk. For many practical applications, such as in tunnel or giant magnetoresistance (TMR, GMR) devices, thin films are necessary.

Additionally, it can be very difficult to prepare high-quality single crystals of (inverse) Heusler compounds, so preparation of epitaxial thin films provides an attractive alternative route to study anisotropic properties of these materials.

The final Chapter 8 deals with the relation between the inverse Heusler compound Mn_2CoGa and the Heusler compounds Mn_2VGa and Co_2MnSi .

2 Experimental Methods

Within this work, thin films have been prepared and characterized. This chapter gives a brief introduction into the main techniques of preparation and characterization. All samples were prepared by DC and RF magnetron co-sputtering and electron beam evaporation. The structural characterization of the films was performed by x-ray diffraction and reflectivity. The chemical composition analysis was done by hard x-ray fluorescence. Element- and site-resolved measurements of the electronic and magnetic structure of the samples were carried out by soft x-ray absorption spectroscopy.

2.1 Sample Preparation

All thin film samples presented in this work were deposited by DC and RF magnetron co-sputtering [46] on MgO substrates with (001) orientation. The apparatus used for the deposition is a customly designed machine built by BESTEC, BERLIN. Its ultra-high vacuum recipient is equipped with (at the time of writing) seven three-inch magnetron sputter sources and an electron beam evaporator. The sources are placed in a confocal geometry, with the substrate carrier in the focus, see Fig. 2.1. Five of the sources are driven by DC generators, the other two sources are driven by an RF generator, operated at 13.56 MHz. This allows to co-sputter metals and insulators. The sample carrier can be rotated to obtain homogenous thickness and stoichiometry across a diameter of about 100 mm. It can be radiatively heated with a ceramic heater with a power of up to 1000 W, yielding a sample carrier temperature of over 900°C. High purity (6N) argon is used as the sputter gas, typically at a pressure of $2 \cdot 10^{-3}$ mbar. A reactive gas (oxygen or nitrogen) can be added if desired.

The electron beam evaporator is mostly used to deposit a protective MgO film on top of the sample, in order to protect the film below from oxidation. It is usually operated at 6 kV and a beam current of 10 mA (for MgO). The deposition process can be calibrated and monitored with a film thickness sensor.

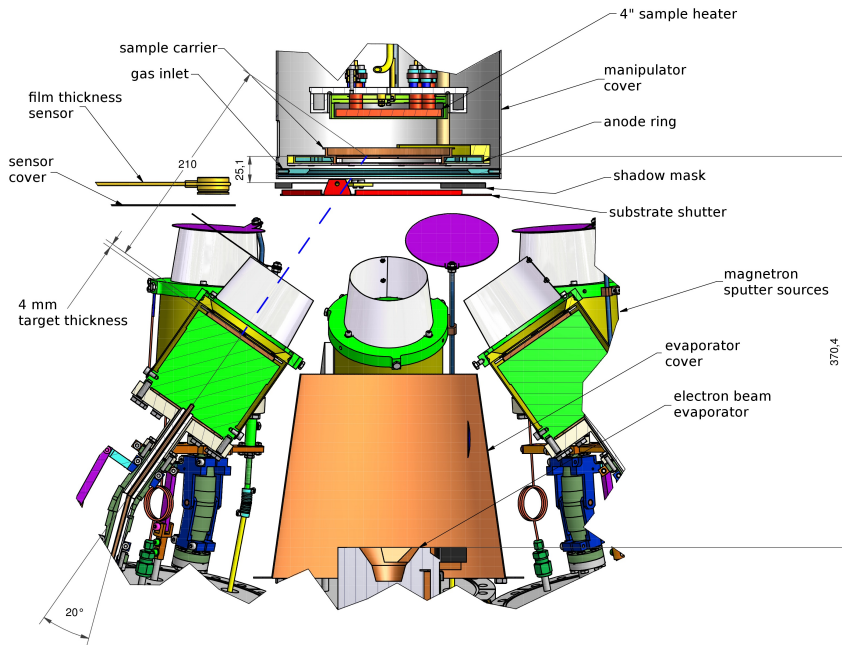


Figure 2.1: Technical drawing (cross section) of the BESTEC sputter machine [47].

2.2 Structural Characterization

2.2.1 X-Ray Diffraction

The diffraction of x-rays is a well known and versatile tool to determine the structure of a crystalline solid [48]. Bragg's law relates the lattice spacing d , the wavelength λ and the diffraction angle θ via

$$\lambda = 2d \sin \theta. \quad (2.1)$$

In a cubic material, the lattice spacing can be expressed with Miller's indices h, k, l and the lattice constant a , such that one can express Bragg's law as

$$\sin \theta_{hkl} = \frac{\lambda}{2a} \sqrt{h^2 + k^2 + l^2}. \quad (2.2)$$

Bragg's law describes at which diffraction angles one can possibly find an x-ray reflection, but it does not predict the intensity. The intensity $I(hkl)$ of an x-ray

reflection from the (hkl) plane of a thin film on a substrate is given by

$$I(\theta_{hkl}) \propto |F(hkl)|^2 \text{LP}(\theta_{hkl}) \text{DW}(\theta_{hkl}) \text{ODF}_{hkl}(\varphi, \psi). \quad (2.3)$$

The structure factor $F(hkl)$ contains the information on the crystal structure. It is derived as a Fourier transform of the charge density of the solid, giving

$$F(hkl) = \sum_j f_j(\theta_{hkl}) e^{2\pi i (hx_j + ky_j + lz_j)}, \quad (2.4)$$

where $f_j(\theta_{hkl})$ is the atomic form factor and x_j, y_j, z_j are the coordinates of site j in the unit cell. $f_j(\theta_{hkl})$ equals the atomic number in the long wavelength ($\lambda \rightarrow \infty$) or forward scattering ($\theta \rightarrow 0$) limit.

The Lorentz-Polarization factor includes the diffraction geometry and polarization effects from the diffraction. For a powder or powder-like film it is given as

$$\text{LP}(\theta_{hkl}) = \frac{1 + \cos^2 2\theta_{hkl}}{\sin^2 \theta_{hkl} \cos \theta_{hkl}}, \quad (2.5)$$

where the numerator describes the polarization and the denominator the diffraction geometry (the Lorentz term). The temperature or Debye-Waller factor $\text{DW}(\theta_{hkl})$ takes into account lattice vibrations, which are negligible in the cases discussed in this work. Finally, the pole density or orientation distribution function $\text{ODF}_{hkl}(\varphi, \psi)$ describes the distribution of crystal orientations with respect to the Euler angles φ, ψ . It accounts for texture and epitaxial growth and it can be interpreted as a set of two-dimensional rocking curves.

Disorder is accounted for by appropriate weighting of $f_i(\theta_{hkl})$ with the site occupancies. Further, in a more general expression the atomic form factor contains anomalous scattering corrections which depend on the energy E :

$$f(\theta, E) = f_0(\sin \theta / \lambda) + f_1(E) + i f_2(E), \quad (2.6)$$

where $E = hc / \lambda$. These corrections are important close to atomic absorption edges. They are tabulated or computed with the Cromer-Lieberman method [49, 50]. Therefore, expression (2.3) is most conveniently evaluated numerically.

For Heusler compounds, we can divide all possible x-ray reflections (those allowed by the extinction rules for the face centered cubic lattice) into three groups with three different structure factors [51]:

- h, k, l all odd ((111), (311), (331), (333), (511), (531),...)

$$|F(111)|^2 = 16 \left[(f_A - f_C)^2 + (f_B - f_D)^2 \right] \quad (2.7)$$

- $h + k + l = 2(2n - 1)$, $n = 1, 2, \dots$ ((200), (222), (420), (600), (442),...)

$$|F(200)|^2 = 16 [(f_A + f_C) - (f_B + f_D)]^2 \quad (2.8)$$

- $h + k + l = 4n$, $n = 1, 2, \dots$ ((220), (400), (422), (440), (620), (444),...)

$$|F(400)|^2 = 16 [f_A + f_B + f_C + f_D]^2 \quad (2.9)$$

The structure factors are given here neglecting the anomalous correction terms. The third group of reflections is independent of chemical disorder on the four sublattices, making it a fundamental reflection. The other two groups depend on disorder; the first group vanishes if B - D order is not present, i.e., the structure is equivalent to the B2 structure (a primitive cubic structure with two atoms in the basis). The second group vanishes, if additionally A/C - B/D order is missing, such that the structure becomes equivalent to the A2 structure (a primitive body-centered cubic structure). In the latter case, the four sublattices are randomly occupied.

The width of the reflections has contributions from the instrument itself, from the size of the crystallites and from strain within the crystallites. With a Gaussian instrumental peak broadening and a Lorentzian convolution of grain size and strain effects, one separates the contributions by

$$B_{\text{obs}}^2 = B_{\text{inst}}^2 + B_{\text{ss}}^2, \quad (2.10)$$

where

$$B_{\text{ss}} \cdot \cos \theta = \frac{k\lambda}{D} + 4\varepsilon_{[hkl]} \sin \theta. \quad (2.11)$$

B_{obs} is the observed integral width, B_{inst} the instrumental width, B_{ss} the size-strain width, the shape factor $k = 0.9$, the coherence length (grain size) D and the averaged $[hkl]$ component of the strain tensor $\varepsilon_{[hkl]}$. This scheme is called Williamson-Hall analysis [52]. The instrument used for this work, a PHILIPS X'PERT PRO MPD, is equipped with Bragg-Brentano optics, collimator point-focus optics, and an open Euler cradle. It is operated with Cu K_{α} radiation ($\lambda = 1.5419 \text{ \AA}$).

2.2.2 X-Ray Reflection

For very small angles of incidence, a crystal can be described as an effective medium, i.e., in terms of optical theory. It is convenient to write the refractive

index in the x-ray regime as $n = 1 - \delta + i\beta$, where δ, β are small positive numbers. The refractive index is smaller than unity for x-rays, so the phase velocity of x-rays is slightly larger in the medium than in vacuum. This gives rise to a total external reflection of the x-rays up to a critical angle θ_c . Neglecting absorption ($\beta = 0$) one finds

$$\theta_c = \sqrt{2\delta} \propto \sqrt{n_a \text{Re } f(0)} \propto \sqrt{n_a Z} \propto \sqrt{\rho}, \quad (2.12)$$

with the number of atoms per volume n_a , the forward scattering limit of the atomic form factor $f(0)$, the nuclear charge Z and the mass density ρ [53]. Therefore, one can determine the mass density of a film by determining the critical angle. For a compound, the stoichiometry has to be known approximately in order to apply the proper anomalous scattering corrections. Above the critical angle, the reflectivity drops quickly as $1/\theta^4$.

Penetration of x-rays into a thin film on a substrate gives rise to partial reflections at the interfaces. These add up coherently and produce an interference pattern similar to the Fabry-Perot effect, the Kiessing fringes. From the spacing of the maxima or minima $\theta_{m+1} - \theta_m$ one can determine the film thickness d :

$$d \approx \frac{\lambda}{2} \frac{1}{\theta_{m+1} - \theta_m}, \quad \theta \gg \theta_c. \quad (2.13)$$

Roughness reduces the amplitude of the oscillations and can complicate the determination of the film density. In practice, an x-ray reflectivity measurement is fit numerically with the Parratt formalism, which includes absorption and roughness and allows to fit multiple layers [54].

2.3 Chemical Composition Analysis by X-Ray Fluorescence

Hard x-ray fluorescence is a widely used tool for chemical composition analysis of elements heavier than sodium. A photon interacting with an atom can promote an electron to the continuum if the photon's energy is higher than the electron's binding energy. Figure 2.2 (left) shows the term scheme of the lowest absorption edges, the K-edge and the $L_{1,2,3}$ -edges. The created vacancy (the core-hole) is filled by electrons from higher levels, either via the Auger process emitting another electron, or radiatively by emission of a photon. The latter process is the x-ray fluorescence, and its probability (the fluorescence yield)

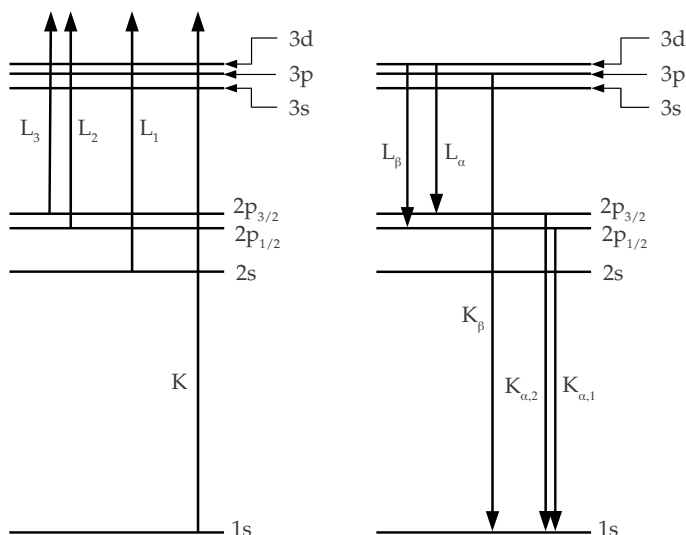


Figure 2.2: Left: x-ray absorption from core levels. Right: some x-ray emission transitions. Spin-orbit splitting of 3p and 3d states is omitted.

depends on the shell and the binding energy: the higher the binding energy, the larger the fluorescence yield. Figure 2.2 (right) gives an overview of the high-energy x-ray emission lines. The energies are characteristic for the emitting atom, which is why they are called characteristic radiation. The intensities are nearly independent on the chemical environment, so the characteristic radiation can be used for stoichiometry analysis of solids.

During this work, an energy dispersive x-ray detection system has been implemented into the x-ray diffractometer. It consists of an AMPTEK XR-100CR Si-PIN detector¹ and a digital pulse processor. The detector is located within a He enclosure with Kapton windows, to allow analysis of light elements, the characteristic radiation of which is otherwise attenuated by air.

A (thin film) sample is excited by the continuous bremsstrahlung from the Cu anode tube, operated at 40 kV. If necessary, a 400 μm thick Al foil removes the characteristic Cu radiation from the excitation spectrum, which is modeled with Ebel's model [55]. The fluorescence spectrum of the sample is post-

¹Trivia: The same type of detector was on the NASA Pathfinder mission to Mars.

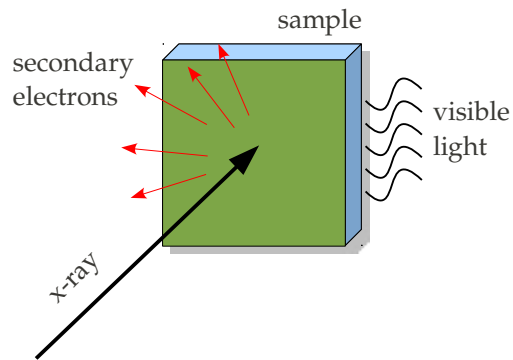


Figure 2.3: Detection modes of soft x-ray absorption: (total) electron yield and substrate luminescence.

processed to remove escape and sum peaks, smoothed, and the background is removed. Finally, a fundamental parameters analysis based on a non-linear fitting procedure is performed by the analysis software shipped with the detector.

The fundamental parameters analysis is carried out entirely without the need for standards. The geometry, filters, environments and properties of the source and the detector are supplied, everything else is based on tabulated atomic parameters and accurate physical modeling of the setup. Effects of re-absorption and secondary fluorescence are taken into account in dependence on the sample thickness.

2.4 Soft X-Ray Absorption Spectroscopy

Soft x-rays (≈ 100 eV - 2000 eV) absorbed by the $2p$ levels of $3d$ transition metals allow to probe the unoccupied $3d$ and $4s$ states. The absorption is detected either by the sample drain current, which is proportional to the total electron yield (TEY) of secondary electrons [56], or by measuring the substrate visible light luminescence [57], see Fig. 2.3. In the first case, one has a very surface sensitive measurement, because the secondary electrons have a typical escape length of 2 - 3 nm. In the latter case, a thickness integrated measurement is obtained, but the film thickness is limited to about 50 nm.

2.4.1 X-Ray Absorption Near Edge Structure

The unoccupied states in a solid (or in a molecule) give rise to resonant absorption, and result in an x-ray absorption near edge structure (XANES, also near edge x-ray absorption fine structure (NEXAFS)). This can be used to extract information on hybridizations or orientation dependence of orbitals. Several dichroic effects can be observed in x-ray absorption, some of which are associated with magnetism; these are presented in the following.

2.4.2 X-Ray Magnetic Circular Dichroism

X-ray magnetic circular dichroism (XMCD) occurs if the spin-up and spin-down final states are different, i.e., if the system is ferromagnetic. A circularly polarized (with a single photon helicity) x-ray beam is absorbed by the sample, which is magnetized parallel or antiparallel to the beam direction, see Fig. 2.4. The resulting spectra, $\mu^+(E)$ and $\mu^-(E)$, can be combined to the average x-ray absorption and the difference spectrum,

$$\text{XAS}(E) = \frac{1}{2} (\mu^+(E) + \mu^-(E)) \quad (2.14)$$

$$\text{XMCD}(E) = \mu^+(E) - \mu^-(E). \quad (2.15)$$

These spectra can be evaluated with the XMCD sum rules to obtain spin and orbital moments of the absorber [58]. One defines integrals p , q and r as

$$\begin{aligned} p &= \int_{L_3} dE (\mu^+ - \mu^-) \\ q &= \int_{L_3+L_2} dE (\mu^+ - \mu^-) \\ r &= \int_{L_3+L_2} dE \left(\frac{\mu^+ + \mu^-}{2} - S \right) \end{aligned}$$

A no-free-parameter two-step-like background function S with thresholds set to the points of inflection on the low energy side of the L_3 and L_2 resonance and step heights of $2/3$ (L_3) and $1/3$ (L_2) of the average absorption coefficient in the post-edge region ("post-edge jump height η ") is introduced here. It accounts for the absorption into delocalized, s -like states.

Sufficiently far away from the absorption edges, interactions among the atoms in the samples can be neglected [59] and the post-edge jump height η is proportional to $\sum_i X_i \sigma_{ai}$, where X_i is the relative concentration of atom i

in the sample and σ_{ai} is its total atomic absorption cross section. As pointed out by Stöhr [60], the number of unoccupied $3d$ states N_h is proportional to the integral r via $r = CN_h\eta$. The constant C depends on the transition matrix elements connecting the core and valence states involved in the $2p - 3d$ transitions and has been analyzed by Scherz for different $3d$ transition metals ($C^{\text{Ti}} = 5.4 \text{ eV}$, $C^{\text{V}} = 5.3 \text{ eV}$, $C^{\text{Cr}} = 5.7 \text{ eV}$, $C^{\text{Mn}} \approx 6.0 \text{ eV}$, $C^{\text{Fe}} = 6.6 \text{ eV}$, $C^{\text{Co}} = 7.8 \text{ eV}$, $C^{\text{Ni}} = 8.1 \text{ eV}$; the Mn value is interpolated between the other data) [61]. When neglecting the spin magnetic dipole term $\langle T_Z \rangle$ in the XMCD sum rules, the spin and orbital magnetic moments m_{spin} and m_{orb} and their ratio are then given as

$$m_{\text{orb}} = -\frac{1}{P_{hv} \cos \theta} \frac{4q}{6C\eta} \quad (2.16)$$

$$m_{\text{spin}} = -\frac{1}{P_{hv} \cos \theta} \frac{(6p - 4q)}{2C\eta} \quad (2.17)$$

$$\frac{m_{\text{orb}}}{m_{\text{spin}}} = \frac{2q}{9p - 6q} \quad (2.18)$$

with the elliptical polarization degree P_{hv} and the angle θ between magnetization and x-ray beam direction.

2.4.3 X-Ray Magnetic Linear Dichroism

X-ray magnetic linear dichroism (XMLD) arises as the difference between parallel and perpendicular orientation of x-ray polarization and magnetization when using linearly polarized light (see Fig. 2.4):

$$\text{XMLD}(E) = \mu^{\parallel}(E) - \mu^{\perp}(E). \quad (2.19)$$

Because XMLD is essentially given as the difference between $\Delta m = 0$ and the averaged $\Delta m = \pm 1$ transitions, it is a sensitive probe of the local crystal field. For systems with m degeneracy, i.e., spherical symmetry, it is approximately given by $\text{XMLD}(E) \approx \mp 0.1 \Delta \frac{d}{dE} \text{XMCD}(E)$. Δ describes the core-level exchange splitting due to the local magnetic field. Δ and the XMCD scale with the local spin magnetic moment, which gives rise to a quadratic dependence on the local spin moment [62, 63, 64]. In contrast to XMCD, XMLD is only sensitive to the direction of the spin moments, not their orientation. This allows to probe antiferromagnetic and ferrimagnetic materials with XMLD. For

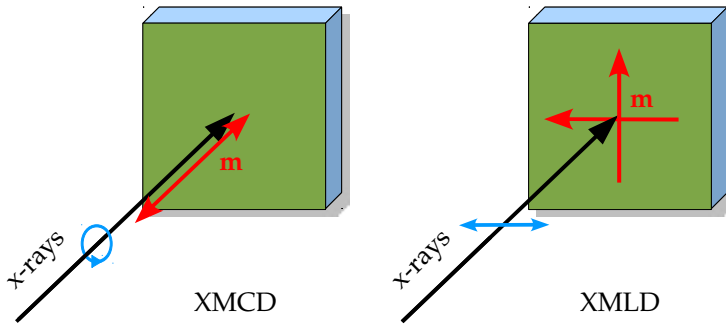


Figure 2.4: X-ray magnetic circular dichroism and x-ray magnetic linear dichroism. For XMCD light of constant helicity is used; the magnetization is switched between parallel and antiparallel to the beam. For XMLD linearly polarized light is used. The magnetization is switched between parallel and perpendicular to the polarization direction.

local moments, the core-level exchange splitting is stronger than for itinerant moments, which leads to an enhanced XMLD amplitude. Therefore, XMLD can be used as a probe for the locality of magnetic moments by comparison with reference systems. In contrast to XAS and XMCD, the magnetic linear dichroism is strongly anisotropic in cubic systems [62].

2.5 Other Techniques

Additional characterization of some samples involved magnetic characterization with superconducting quantum interference devices (SQUID) and chemical analysis with inductively coupled plasma optical emission spectroscopy (ICP-OES).

Electrical four-point transport measurements in dependence on the sample temperature down to about 20 K were performed in a cryostat. Magnetoresistance was measured using a variable permanent magnet (coaxial Halbach cylinder configuration, Magnetic Solutions Multimag) with a maximum field strength of 10 kOe in the cryostat. Measurements up to 500 K were done in a vacuum furnace. For these measurements, the samples were prepared by standard photolithographic techniques.

3 Theoretical Methods

The theoretical parts of this work have been carried out with computer codes based on density functional theory (DFT). Different implementations of DFT come with individual advantages and disadvantages. As a user, one has to decide which implementation is best suited for the problem to be investigated. This choice depends to a large part on the feature set of the various computer codes, but also on the suitability of the basis set for the problem. For this work, the full-potential linearized augmented plane waves (FP-LAPW) method, the spin-polarized relativistic Korringa-Kohn-Rostoker (SPRKKR) method, and the real-space relativistic full multiple scattering method (implemented in FEFF9) have been used.

In this chapter, the basic ideas of DFT are outlined following Richard Martin's textbook [65]. The descriptions of the computer codes involve details of the basis sets and the solution methods. Particular focus is put on the relevant features provided in the codes. Two important methods, the calculation of Curie temperatures within an effective Heisenberg model and the computation of x-ray absorption spectra, are discussed in individual sections. Atomic units ($e^2 = \hbar = m_e = 1$) are used throughout this chapter.

3.1 Density Functional Theory

Density functional theory as formulated by Hohenberg and Kohn in 1964 [66] is an exact theory of an interacting electron gas in an external potential. In the case of a solid or a molecule, the external potential is the Coulomb potential of the nuclei, which are assumed as fixed (Born-Oppenheimer-Approximation). The Hamiltonian of the many-electron system can be written as

$$\hat{H} = -\frac{1}{2} \sum_i \nabla_i^2 + \frac{1}{2} \sum_{i \neq j} \frac{1}{|\mathbf{r}_i - \mathbf{r}_j|} + \sum_i V_{\text{ext}}(\mathbf{r}_i) + E_{nn} \quad (3.1)$$

in which the first term is the kinetic energy, the second term is the Coulombic repulsion between electron pairs, and the third term describes the energy of the electrons in the external potential. E_{nn} is the classical interaction of the nuclei

and also contains all other contributions to the energy that do not influence the electrons. The stationary solution of the N -electron Schrödinger equation has the form $\Psi(\mathbf{r}_1, \dots, \mathbf{r}_N)$. The electron density $n(\mathbf{r})$ is given by the expectation value of the density operator $\hat{n}(\mathbf{r}) = \sum_{i=1,N} \delta(\mathbf{r} - \mathbf{r}_i)$:

$$n(\mathbf{r}) = \frac{\langle \Psi | \hat{n}(\mathbf{r}) | \Psi \rangle}{\langle \Psi | \Psi \rangle}. \quad (3.2)$$

The total energy is the expectation value of the Hamiltonian:

$$E = \langle \hat{H} \rangle := \frac{\langle \Psi | \hat{H} | \Psi \rangle}{\langle \Psi | \Psi \rangle}. \quad (3.3)$$

3.1.1 The Hohenberg-Kohn Theorems

Hohenberg and Kohn proved the following theorems:

- **Theorem I:** For any system of interacting particles in an external potential $V_{\text{ext}}(\mathbf{r})$, this potential is determined uniquely up to an additive constant by the ground state particle density $n_0(\mathbf{r})$. Since the Hamiltonian is thus fully determined up to a constant shift of the energy, it follows that the many-electron wavefunctions are determined. Therefore all properties of the system are completely determined by the ground state density $n_0(\mathbf{r})$.
- **Theorem II:** A universal functional for the energy $E[n]$ in terms of the density $n(\mathbf{r})$ can be defined, valid for any external potential $V_{\text{ext}}(\mathbf{r})$. For any particular $V_{\text{ext}}(\mathbf{r})$, the exact ground state energy of the system is the global minimum value of this functional, and the density $n(\mathbf{r})$ that minimizes the functional is the exact ground state density $n_0(\mathbf{r})$. The functional $E[n]$ alone is sufficient to determine the exact ground state energy and density.

In short, the Hohenberg-Kohn theorems state that there is a one-to-one correspondence between the ground-state density and the ground-state potential, and that the ground-state density is the global minimum of the energy functional $E[n]$. Thus, it can be determined from a variational calculation.

In analogy to the many-electron Hamiltonian (3.1), the Hohenberg-Kohn total energy functional $E_{\text{HK}}[n]$ is

$$E_{\text{HK}}[n] = T[n] + E_{\text{int}}[n] + \int d^3r V_{\text{ext}}(\mathbf{r})n(\mathbf{r}) + E_{\text{nn}} \quad (3.4)$$

where $T[n]$ is the electron kinetic energy and $E_{\text{int}}[n]$ is the interaction energy among the electrons. These terms can be gathered in a universal functional of the density, i.e., one that is the same for all electron systems:

$$F_{\text{HK}}[n] := T[n] + E_{\text{int}}[n]. \quad (3.5)$$

If this functional was known, one could find the ground state by minimization of the total energy with respect to the density $n(\mathbf{r})$.

A generalization to spin-polarized systems is easily possible. A Zeeman term is added to the Hamiltonian, which is different for spin up and down electrons in the presence of a magnetic field. In this case, two densities, one for each spin, are defined and satisfy the Hohenberg-Kohn-Theorems individually. Then the density is $n(\mathbf{r}) = n(\mathbf{r}, \uparrow) + n(\mathbf{r}, \downarrow)$, and the spin density is given by $s(\mathbf{r}) = n(\mathbf{r}, \uparrow) - n(\mathbf{r}, \downarrow)$.

3.1.2 The Kohn-Sham Ansatz

Although it is in principle sufficient to find the density of a given material to understand its properties, there is no way known how to extract them from the density. Further, the functional $F_{\text{HK}}[n]$ is not known in general. Therefore, the density functional theory as formulated by Hohenberg and Kohn is of minor practical relevance.

Kohn and Sham proposed in 1965 to replace the full interacting many-body problem with a simpler, non-interacting auxiliary problem [67]. Their ansatz rests on the assumption that the ground state density of the interacting system can be expressed by the ground state density of a properly chosen non-interacting system. The key idea is to re-introduce orbitals for non-interacting electrons and put the many-body problem into an exchange-correlation functional of the density. This way, the Hohenberg-Kohn functional $F_{\text{HK}}[n]$ becomes simply the kinetic energy of the non-interacting fictitious electrons.

The auxiliary Kohn-Sham Hamiltonian, replacing (3.1), is defined by

$$H_{\text{KS}}^{\sigma}(\mathbf{r}) = -\frac{1}{2}\nabla^2 + V_{\text{KS}}^{\sigma}(\mathbf{r}), \quad (3.6)$$

where σ denotes the spin-index. The $N = N^{\uparrow} + N^{\downarrow}$ electrons occupy orbitals $\psi_i^{\sigma}(\mathbf{r})$ with the lowest eigenvalues ε_i^{σ} determined by the Schrödinger-like Kohn-Sham equations

$$(H_{\text{KS}}^{\sigma} - \varepsilon_i^{\sigma}) \psi_i^{\sigma}(\mathbf{r}) = 0. \quad (3.7)$$

The density of the Kohn-Sham system is given by

$$n(\mathbf{r}) = \sum_{\sigma} \sum_{i=1}^{N_{\sigma}} |\psi_i^{\sigma}(\mathbf{r})|^2, \quad (3.8)$$

and the Kohn-Sham kinetic energy is

$$T_s = \frac{1}{2} \sum_{\sigma} \sum_{i=1}^{N_{\sigma}} |\nabla \psi_i^{\sigma}(\mathbf{r})|^2. \quad (3.9)$$

The classical Coulomb interaction energy of the electron density with itself is given by the Hartree energy

$$E_{\text{Hartree}}[n] = \frac{1}{2} \int d^3r \int d^3r' \frac{n(\mathbf{r})n(\mathbf{r}')}{|\mathbf{r} - \mathbf{r}'|}. \quad (3.10)$$

With these ingredients, the Hohenberg-Kohn total energy functional (3.4) can be rewritten as

$$E_{\text{KS}} = T_s[n] + E_{\text{Hartree}}[n] + \int d^3r V_{\text{ext}}(\mathbf{r})n(\mathbf{r}) + E_{\text{nn}} + E_{\text{xc}}[n] \quad (3.11)$$

The many-body effects of exchange and correlation are put into the exchange-correlation functional $E_{\text{xc}}[n]$. Now, the Kohn-Sham potential $V_{\text{KS}}^{\sigma}(\mathbf{r})$ can be expressed in terms of variations with respect to the density as

$$V_{\text{KS}}^{\sigma}(\mathbf{r}) = V_{\text{ext}}(\mathbf{r}) + \frac{\delta E_{\text{Hartree}}}{\delta n(\mathbf{r}, \sigma)} + \frac{\delta E_{\text{xc}}}{\delta n(\mathbf{r}, \sigma)} =: V_{\text{ext}}(\mathbf{r}) + V_{\text{Hartree}}(\mathbf{r}) + V_{\text{xc}}^{\sigma}(\mathbf{r}). \quad (3.12)$$

As (3.12) depends on the density computed from the solution of (3.7), one has to iterate the equations to self-consistency, starting from an initial guess (from, e.g., a superposition of atomic densities).

3.1.3 The Exchange-Correlation Functional

The Kohn-Sham ansatz is an exact way to find the exact ground-state density and total energy, no approximations have been made yet. Unfortunately, the exchange-correlation functional is not known. The major obstacle of solving the full many-body problem has been reformulated with the Kohn-Sham equations, so that most of the total energy of the electron system is calculated correctly. Only a small fraction of the total energy, the exchange-correlation energy, has to be approximated. Two different paradigms for the derivation of the

approximations can be distinguished: empirical and non-empirical. While empirical functionals are constructed to match experimental datasets as good as possible, non-empirical functionals are constructed based on known physical constraints, which the functional has to obey.

Local spin density approximation (LSDA)

The simplest approach to the problem of the exchange-correlation functional is to use only local quantities. Usually it is split into a sum of exchange and correlation contributions, which are derived from the homogeneous electron gas (HEG),

$$E_{xc}^{\text{LSDA}}[n^\uparrow, n^\downarrow] = \int d^3r n(\mathbf{r}) \left[e_x^{\text{HEG}}(n^\uparrow(\mathbf{r}), n^\downarrow(\mathbf{r})) + e_c^{\text{HEG}}(n^\uparrow(\mathbf{r}), n^\downarrow(\mathbf{r})) \right]. \quad (3.13)$$

The exchange contribution is known analytically, and the correlation term is typically a parametrized expression based on Monte-Carlo simulations. Various parametrizations have been proposed, named after their authors. A popular form is that proposed by Perdew and Wang (PW92), which is improved over earlier forms [68].

One can expect the LSDA to work best in systems that are close to the HEG, like simple metallic solids. Surprisingly, it does even perform quite well for molecules, though it has a tendency to overbind, i.e., binding energies are too large and bond lengths are too short. Thus it is not good enough to be useful for thermochemistry, still it provides very good structural properties.

Generalized gradient approximation (GGA)

In addition to the local density, one can add information about the gradient of the density to get better approximations for systems with strongly varying density. Functionals that take into account gradients are called generalized-gradient approximations (GGA). They take the general form

$$E_{xc}^{\text{GGA}}[n^\uparrow, n^\downarrow] = \int d^3r n(\mathbf{r}) e_{xc}^{\text{GGA}}(n^\uparrow(\mathbf{r}), n^\downarrow(\mathbf{r}), |\nabla n^\uparrow(\mathbf{r})|, |\nabla n^\downarrow(\mathbf{r})|), \quad (3.14)$$

and are typically referred to as semi-local functionals. The standard GGA functional of the non-empirical type is the Perdew-Burke-Ernzerhof (PBE) functional, which largely corrects the overbinding of LSDA and usually overestimates the bond lengths slightly [69].

Non-collinear spin density

Usually, the spin density has a common axis; it is collinear. Non-collinear calculations, with a spin axis that varies in space, involve a modified treatment of the Kohn-Sham equations and the exchange-correlation functional. The Kohn-Sham Hamiltonian becomes a 2×2 matrix, to which the exchange-correlation potential contributes off-diagonal components. By finding the local axis of spin quantization for every point in space, the usual form of the LSDA can be used. GGA expressions have to be modified involving the gradient of the spin axis.

3.1.4 Periodic Boundary Conditions

Periodic boundary conditions, which are naturally present in an extended crystal, allow to evaluate the Kohn-Sham equations in reciprocal space. The foundation for this is given through the Bloch theorem,

$$\hat{T}_n \psi(\mathbf{r}) = \psi(\mathbf{r} + \mathbf{T}_n) = e^{i\mathbf{k} \cdot \mathbf{T}_n} \psi(\mathbf{r}), \quad (3.15)$$

in which $\mathbf{T}_n = n_1 \mathbf{a}_1 + n_2 \mathbf{a}_2 + n_3 \mathbf{a}_3$ describes a translation along the lattice vectors \mathbf{a}_i with $|n_i| = 0, 1, 2, \dots$. Eigenfunctions of the periodic Hamiltonian can be written as

$$\psi_{\mathbf{k}}(\mathbf{r}) = e^{i\mathbf{k} \cdot \mathbf{r}} u_{\mathbf{k}}(\mathbf{r}), \quad (3.16)$$

where $u_{\mathbf{k}}(\mathbf{r} + \mathbf{T}_n) = u_{\mathbf{k}}(\mathbf{r})$. The eigenstates of the Hamiltonian can be found separately for each \mathbf{k} in the Brillouin zone, leading to bands of eigenvalues $\varepsilon_{i,\mathbf{k}}$. One finds intrinsic properties of a crystal per unit cell – such as the number of electrons, the magnetization, the total energy, etc. – by averaging over the \mathbf{k} points, where N_k is the total number of \mathbf{k} points. The density is given by

$$n(\mathbf{r}) = \frac{1}{N_k} \sum_{\mathbf{k}} n_{\mathbf{k}}(\mathbf{r}). \quad (3.17)$$

The density of states $\rho(E)$ is calculated from the energy bands $\varepsilon_{i,\mathbf{k}}$ as

$$\rho(E) = \frac{1}{N_k} \sum_{i,\mathbf{k}} \delta(\varepsilon_{i,\mathbf{k}} - E). \quad (3.18)$$

Obviously, an adequate \mathbf{k} point sampling of the Brillouin zone is crucial for numerically exact calculations. In reciprocal space calculations, the mesh of \mathbf{k} points has to be made dense enough to obtain good numerical convergence of

the quantities under investigation. Symmetry operations are applied to reduce the number of \mathbf{k} points, such that only the irreducible wedge of the Brillouin zone is used.

3.2 Implementations of DFT Used in This Work

3.2.1 The Elk FP-LAPW code

Elk is an open-source full potential linearized augmented plane waves (FP-LAPW, FLAPW) code [70]. FLAPW treats core and valence electrons simultaneously, and is generally considered the most accurate method to solve the Kohn-Sham problem.

The FLAPW method starts from the muffin-tin partitioning. The unit cell is divided into spheres, centered on the nuclei (the muffin-tins) and a region in between (the interstitial). The basis set is built from spherical harmonics in the muffin-tin spheres and plane waves in the interstitial. This is referred to as an augmented plane waves (APW) basis, which was originally suggested by Slater. Matching conditions on the muffin-tin boundary can be imposed to arbitrary order. The basis set used by Elk is a linearized version of the APW+lo method [71]. It can be expressed as

$$\phi^{\mathbf{k}}(\mathbf{r}) = \begin{cases} \sum_{\mathbf{G}} c_{\mathbf{G}} e^{i(\mathbf{G}+\mathbf{k})\cdot\mathbf{r}} & \mathbf{r} \in \text{interstitial} \\ \sum_{lm} \alpha_{lm}^{\mathbf{k}} u_l(r, E_l^1) Y_{lm}(\hat{\mathbf{r}}) & \mathbf{r} \in \text{muffin-tin} \end{cases} \quad (3.19)$$

where $r = |\mathbf{r}|$ and $\hat{\mathbf{r}} = \mathbf{r}/r$. The plane wave coefficients $c_{\mathbf{G}}$ are variational quantities, and the $\alpha_{lm}^{\mathbf{k}}$ are determined by the matching conditions at the muffin-tin boundary. Matching to zeroth order (i.e., only the value of the wave function) and obtaining the solutions $u_l(r, E_l^1)$ (one per angular momentum l) of radial Schrödinger equations at fixed energy E_l^1 is sufficient, if local orbitals are added to the APW set. The local orbitals (lo/LO) are represented by radial functions and spherical harmonics in the muffin-tin spheres and are forced to zero on the muffin-tin boundary. They do not depend on \mathbf{k} . Two types of local orbitals are added to the basis set:

$$\phi_{lm}^{\text{lo}}(\mathbf{r}) = \left(\beta_{lm} u_l(r, E_l^1) + \gamma_{lm} u_l'(r, E_l^1) \right) Y_{lm}(\hat{\mathbf{r}}) \quad (3.20)$$

$$\phi_{lm}^{\text{LO}}(\mathbf{r}) = \left(\delta_{lm} u_l(r, E_l^1) + \epsilon_{lm} u_l'(r, E_l^1) + \zeta_{lm} u_l(r, E_l^2) \right) Y_{lm}(\hat{\mathbf{r}}) \quad (3.21)$$

The local orbital coefficients β_{lm} and γ_{lm} are determined by the condition to have the local orbital wave function zero at the muffin-tin boundary and its normalization. Similarly, δ_{lm} , ϵ_{lm} , and ζ_{lm} are determined by the wave function and its derivative being zero at the muffin-tin boundary, and its normalization. The second type of local orbitals have atomic-like wave functions and are used to describe semi-core states. The local orbitals greatly improve the flexibility of the basis set at very low computational cost.

The radial functions and derivatives $u_l(r, E_l^1)$, $u_l'(r, E_l^1)$, $u_l(r, E_l^2)$ are solutions of the radial Schrödinger equation at fixed energies E_l^i , which results in a standard linear eigenvalue problem. The linearization energies E_l^1 have to be chosen approximately in the center of the valence bands. The linearization energies E_l^2 are at the approximate energy of the semi-core state, and are searched automatically. The variational coefficients c_G are obtained from the Rayleigh-Ritz variational principle.

Core level electrons are treated separately in a fully relativistic way with the radial Dirac equation. Spin-orbit coupling can be included for the valence states in a second-variational step by adding a $\boldsymbol{\sigma} \cdot \mathbf{L}$ term to the Hamiltonian.

The crystal potential $V(\mathbf{r})$ is expanded similar to the wave functions,

$$V(\mathbf{r}) = \begin{cases} \sum_{\mathbf{G}} V_{\mathbf{G}} e^{i(\mathbf{G}+\mathbf{k}) \cdot \mathbf{r}} & \mathbf{r} \in \text{interstitial} \\ \sum_{lm} V_{lm}(r) Y_{lm}(\hat{\mathbf{r}}) & \mathbf{r} \in \text{muffin-tin.} \end{cases} \quad (3.22)$$

This constitutes the full potential treatment, which is to be contrasted with a spherical approximation (usually called atomic spheres approximation). It corresponds to a truncation of the potential expansion at $l = 0$ and $\mathbf{G} = 0$. Thus, the potential in the muffin-tins would be spherically averaged, and the potential in the interstitial would be constant. The potential expansion of (3.22) allows to treat the full potential without shape approximations.

3.2.2 The Munich SPRKKR package

The Munich SPRKKR package is a spin polarized relativistic implementation of the Korringa-Kohn-Rostoker Green's function method. It determines the electronic structure of a periodic solid by means of multiple scattering theory. The method is described in detail in a review article by the authors of the code [72]. Another very instructive introduction is given by Mavropoulos and Papanikolaou [73]. Here, the main ideas are summarized in short.

One starts from a formal introduction of the Green function $G(\mathbf{r}, \mathbf{r}', E)$ through the Schrödinger equation:

$$(E - H) G(\mathbf{r}, \mathbf{r}', E) = \delta(\mathbf{r} - \mathbf{r}'). \quad (3.23)$$

$G(\mathbf{r}, \mathbf{r}', E)$ has the following spectral representation:

$$G(\mathbf{r}, \mathbf{r}', E) = \lim_{\eta \rightarrow +0} \sum_v \frac{\psi_v(\mathbf{r}) \psi_v^*(\mathbf{r}')}{E - E_v + i\eta}, \quad (3.24)$$

where E_v are the eigenvalues of the Hamiltonian H , and η is a small positive real number. From the Green function, the density of states $\rho(E)$ and the charge density $n(\mathbf{r})$ are obtained as

$$\rho(E) = -\frac{1}{\pi} \text{Im} \int d^3r G(\mathbf{r}, \mathbf{r}, E), \quad (3.25)$$

$$n(\mathbf{r}) = -\frac{1}{\pi} \text{Im} \int^{E_F} dE G(\mathbf{r}, \mathbf{r}, E). \quad (3.26)$$

The Green function contains all information which is given by the eigenfunctions, both are equivalent. All physical properties of the system can be found, if the Green function is known.

There are several ways of calculating the Green function, the most important and flexible of which is multiple scattering theory (MST). The solution of the electronic structure problem is broken up in two parts, a potential related one and a geometry related one.

In the full-potential formulation, the unit cell is divided into Wigner-Seitz polyhedra, centered on the nuclei. The potential of site n is expanded in spherical harmonics, $V^n(\mathbf{r}) = \sum_L V_L^n(r) Y_L(\hat{\mathbf{r}})$, with $L := (l, m)$. The potential of site n is zero outside its polyhedron. In contrast to FLAPW there is no interstitial region.

In a first step, the single-site scattering problem, i.e. the scattering of a plane wave on the potential of site n , is solved individually for all sites. The scattering solutions $\psi^n(\mathbf{r}, E)$ for the isolated potential wells $V^n(\mathbf{r})$ are obtained from the Lippmann-Schwinger equation, an integral form of the Schrödinger equation:

$$\psi^n(\mathbf{r}, E) = \psi_0(\mathbf{r}, E) + \int d^3r' G_0(\mathbf{r}, \mathbf{r}', E) V^n(\mathbf{r}') \psi^n(\mathbf{r}', E), \quad (3.27)$$

with the free-electron wave function $\psi_0(\mathbf{r}, E) = e^{i\mathbf{k} \cdot \mathbf{r}}$ and the corresponding Green function

$$G_0(\mathbf{r}, \mathbf{r}', E) = -\frac{e^{-i\sqrt{E}|\mathbf{r}-\mathbf{r}'|}}{4\pi |\mathbf{r} - \mathbf{r}'|}. \quad (3.28)$$

The scattering behaviour of the potential $V^n(\mathbf{r})$ can be expressed in terms of a t^n -operator,

$$t^n = V^n + V^n G_0 t^n \quad (3.29)$$

$$= V^n (1 - G_0 V^n)^{-1}, \quad (3.30)$$

where the arguments have been dropped for clarity. It is related to the radial part of the scattering solution outside the polyhedron of site n .

Instead of working with the Lippmann-Schwinger equation, one can write a Dyson equation (in operator form) for the single-site scattering problem:

$$\hat{G}^n(E) = \hat{G}_0(E) + \hat{G}_0(E) \hat{V}^n \hat{G}^n(E) \quad (3.31)$$

$$= \hat{G}_0(E) + \hat{G}_0(E) \hat{t}^n(E) \hat{G}_0(E). \quad (3.32)$$

Analogous equations are found in the multiple-scattering case:

$$\hat{G}(E) = \hat{G}_0(E) + \hat{G}_0(E) \hat{V} \hat{G}(E) \quad (3.33)$$

$$= \hat{G}_0(E) + \hat{G}_0(E) \hat{T}(E) \hat{G}_0(E), \quad (3.34)$$

where the multiple-scattering T -matrix operator has been introduced. It can be expanded as

$$\hat{T}(E) = \sum_{nm'} \hat{\tau}^{nm'}(E). \quad (3.35)$$

The scattering path operator $\hat{\tau}^{nm'}(E)$ is defined to transfer an electron wave incoming at site n' into a wave outgoing from site n with all possible scattering events in between incorporated. In an angular momentum basis (denoted by underlines), $\underline{\hat{\tau}}^{nm'}(E)$ has the following equation of motion:

$$\underline{\underline{\tau}}^{nm'}(E) = \underline{t}^n(E) \delta_{nm'} + \underline{t}^n(E) \sum_{m \neq n} \underline{\underline{G}}_0^{nm} \underline{\underline{\tau}}^{mm'}(E). \quad (3.36)$$

For a finite system, this equation is solved by matrix inversion,

$$\underline{\underline{\tau}}(E) = \left[\underline{\underline{t}}(E)^{-1} - \underline{\underline{G}}_0(E) \right]^{-1}. \quad (3.37)$$

The double underlines denote matrices with respect to angular momentum and sites. The matrix in square brackets is known as the real-space KKR matrix. For a periodic solid with sites n at positions \mathbf{R}_n , one finds by Fourier transformation

$$\underline{\underline{\tau}}^{nm'}(E) = \frac{1}{\Omega_{\text{BZ}}} \int_{\Omega_{\text{BZ}}} d^3k \left[\underline{t}(E)^{-1} - \underline{\underline{G}}_0(\mathbf{k}, E) \right]^{-1} e^{i\mathbf{k} \cdot (\mathbf{R}_n - \mathbf{R}_{n'})}, \quad (3.38)$$

with the (reciprocal space) structure constants matrix $\underline{G}_0(\mathbf{k}, E)$ being the Fourier transformed of the real-space structure constants matrix $\underline{G}_0(E)$.

The formalism outlined above is very general with respect to the Hamiltonian H . In practice, the Kohn-Sham equations are solved in the usual iterative way, to self-consistency.

A major advantage of the Green's function formalism is the connection of a perturbed system and a reference system through the Dyson equation:

$$\hat{G} = \hat{G}^{\text{ref}} + \hat{G}^{\text{ref}} \hat{H}^{\text{pert}} \hat{G}. \quad (3.39)$$

This equation gives also the formal background for the scheme described above, in which the free-electron system is the reference system, and the perturbation Hamiltonian is given by the potential of the system under investigation. Because MST separates the electronic structure problem into a geometric and a potential part, it is easy to treat impurities in a perfect host material without using supercells or large clusters, as in other methods:

$$\underline{\tau}^{\text{imp}} = \left[(\underline{\tau}^{\text{host}})^{-1} - (\underline{t}^{\text{host}})^{-1} + (\underline{t}^{\text{imp}})^{-1} \right]^{-1}. \quad (3.40)$$

Similarly, disordered systems are treated within the so-called coherent potential approximation (CPA). An auxiliary CPA medium is introduced, in which the concentration average of the constituents causes no additional scattering. For a binary alloy with concentrations x_A, x_B , this can be expressed with the scattering path operator matrices:

$$x_A \underline{\tau}^{A_{nn}} + x_B \underline{\tau}^{B_{nn}} = \underline{\tau}^{\text{CPA}_{nn}}. \quad (3.41)$$

In analogy to the impurity problem, the component projected scattering path operator matrices are given as

$$\underline{\tau}^{\alpha_{nn}} = \left[(\underline{\tau}^{\text{CPA}})^{-1} - (\underline{t}^{\text{CPA}})^{-1} + (\underline{t}^{\alpha})^{-1} \right]^{-1}, \quad \alpha = A, B. \quad (3.42)$$

The matrix dimension of the multiple-scattering problem is $N_{\text{scatterers}} \cdot (l_{\text{max}} + 1)^2$. Therefore, one tries to keep the angular momentum cutoff as small as possible, typically $l_{\text{max}} = 3$ for d -electron systems. In principle, one would have to take the angular momentum expansion to infinity to obtain the charge density correctly. Due to the truncation, the charge density is somewhat incomplete, leading to a slight miscalculation of the Fermi energy. This problem can be resolved by an analytically exact expression to obtain a correct charge normalization, the Lloyd formula [74, 75].

Only valence electrons are treated with the MST. Core electrons, which are well localized within the polyhedra, are treated relativistically with the Dirac equation. The Hamiltonian for the valence electrons can be chosen either scalar-relativistic (neglecting spin-orbit coupling) or fully relativistic, depending on the problem being investigated.

3.3 Curie Temperatures from an Effective Heisenberg Model

In the classical Heisenberg model of localized spins, the Hamiltonian of the spin system is given by

$$H = - \sum_{ij} \mathbf{e}_i \mathbf{e}_j J_{ij}, \quad (3.43)$$

with the Heisenberg pair exchange coupling parameters J_{ij} , and unit vectors \mathbf{e}_i pointing in the direction of the magnetic moment on site i . SPRKKR allows to calculate the exchange coupling parameters by mapping the (itinerant) system onto a Heisenberg Hamiltonian. The parameters are determined within a perturbative real-space approach using the theory by Liechtenstein *et al.* [76]. In this approach, the energy difference $\Delta E_{ij} = J_{ij} (1 - \cos \theta)$ associated with a rotation of the spins on sites i, j in opposite directions $\pm \theta/2$ is mapped onto the Heisenberg Hamiltonian via

$$J_{ij} = - \frac{1}{4\pi} \text{Im} \int^{E_F} dE \text{Tr} (t_{i\uparrow}^{-1} - t_{i\downarrow}^{-1}) \tau_{\uparrow}^{ij} (t_{j\uparrow}^{-1} - t_{j\downarrow}^{-1}) \tau_{\downarrow}^{ji}, \quad (3.44)$$

where \uparrow, \downarrow denote the up- and down-spin t and τ operators as discussed in the previous section (note the changed indices for better legibility). The real-space calculation gives direct access to the distance-dependence of the pair exchange coupling parameters. A necessary condition for the applicability of this approach is the locality of the spin moments, i.e., the magnitude of the moments should not change on rotation. This condition is not fulfilled in itinerant systems.

From the J_{ij} the Curie temperatures can be calculated within the mean field approximation (MFA). For a single-lattice system the Curie temperature is given within the MFA by

$$\frac{3}{2} k_B T_C^{\text{MFA}} = J_0 = \sum_j J_{0j}. \quad (3.45)$$

In a multi-sublattice system, denoted by indices μ, ν , (as, e.g., the Heusler compounds with four sublattices) one has to solve the coupled equations

$$\begin{aligned} \frac{3}{2}k_B T_C^{\text{MFA}} \langle e^\mu \rangle &= \sum_\nu J_0^{\mu\nu} \langle e^\nu \rangle \\ J_0^{\mu\nu} &= \sum_{r \neq 0} J_{0r}^{\mu\nu} \end{aligned} \quad (3.46)$$

where $\langle e^\nu \rangle$ is the average z component of the unit vector e_r^ν pointing in the direction of the magnetic moment at site (ν, r) . The coupled equations can be rewritten as an eigenvalue problem:

$$\begin{aligned} (\Theta - T \mathbf{I}) \mathbf{E} &= 0 \\ \frac{3}{2}k_B \Theta_{\mu\nu} &= J_0^{\mu\nu} \end{aligned} \quad (3.47)$$

with a unit matrix \mathbf{I} and the vector $E^\nu = \langle e^\nu \rangle$. The largest eigenvalue of the Θ matrix gives the Curie temperature [43, 77]. To converge the Curie temperature with respect to the real-space cluster radius, one has to compute pair exchange coupling parameters up to typically $r_{\text{max}} = 3.0 a$, where a is the lattice constant.

To estimate the accuracy of our method for the Curie temperature determination of Heusler compounds, we calculated the Curie temperatures of some compounds at their respective experimental lattice parameters. The calculated and experimental values are given in Table 3.1. Further values, obtained using the same method, can be found in Ref. [80]. For the Co-based ferromagnetic compounds, the calculated mean-field values are in good agreement with experiment. However, in the case of the two ferrimagnetic Mn-based compounds, the MFA Curie temperature is about 25 % lower than the experimental one. The latter compounds might have more itinerant character, similar to the case

	MFA	expt.	Ref.
Co ₂ MnSi	1049 K	985 K	[51]
Co ₂ TiSn	383 K	355 K	[78]
Mn ₂ VAI	605 K	760 K	[11]
Mn ₂ VGa	560 K	783 K	[79]

Table 3.1: Calculated and experimental Curie temperatures of some Heusler compounds.

of fcc Ni, where the MFA value is about 380 K, in contrast to the experimental value of 630 K [76].

3.4 X-Ray Absorption Spectra from Electronic Structure

3.4.1 General Considerations

In a first approximation, one can describe the absorption of x-rays by a medium as a single-step process: electrons from an occupied core orbital are excited into unoccupied states above the Fermi energy, such that the energy dependence of the absorption is governed by the structure of the unoccupied states. In first order perturbation theory with the electric dipole approximation, we can express the energy-dependent optical (and x-ray) absorption spectra $\mu^\alpha(\omega)$ with Fermi's Golden Rule:

$$\mu^\alpha(\omega) \propto \sum_{i,f} \left| \langle \psi_f | \mathbf{p}^\alpha | \psi_i \rangle \right|^2 \delta(E_f - E_i - \omega), \quad (3.48)$$

where α denotes the polarization, ω the photon energy, i, f label the initial and final wave functions, $E_{i,f}$ the corresponding energy levels, and $\mathbf{p}^\alpha = -i\nabla^\alpha$ the momentum operator with direction α . If only a single initial state – as in the case of x-ray absorption – is considered and the momentum matrix elements $|\langle \psi_f | \mathbf{p}^\alpha | \psi_i \rangle|^2$ are assumed as energy-independent, this expression reduces to the density of states, modified by the dipole selection rules. Absorption from s states probes the p -projected density of states, absorption from p states probes s and d states.

First order perturbation theory assumes an infinitesimal depletion of the initial state during the absorption process. This approximation is, however, often not justified. When a photon is absorbed by a core-level electron, it is promoted to the valence states, leaving a core-hole. The propagating electron can interact with the core-hole, as well as all other electrons. All effects of this kind are condensed in the expression core-hole correlations. The extent, to which these correlations have to be taken into account depends on the absorption edges, the absorbing atom and the system, in which it is embedded. This will be discussed in more detail later.

3.4.2 Elk

A more general formulation of optical properties is given through the optical conductivity tensor $\sigma_{\alpha\beta}(\omega)$ [81]:

$$\sigma_{\alpha\beta}(\omega) = \frac{i}{\Omega} \sum_{\mathbf{k}} \sum_{i,f} \frac{1}{\omega_{if,\mathbf{k}}} \left(\frac{\Pi_{if,\mathbf{k}}^{\alpha} \Pi_{fi,\mathbf{k}}^{\beta}}{\omega - \omega_{if,\mathbf{k}} + i\eta} + \frac{(\Pi_{if,\mathbf{k}}^{\alpha} \Pi_{fi,\mathbf{k}}^{\beta})^*}{\omega + \omega_{if,\mathbf{k}} + i\eta} \right), \quad (3.49)$$

where α, β denote the polarization, Ω the unit cell volume, $\omega_{if,\mathbf{k}} = E_{f,\mathbf{k}} - E_{i,\mathbf{k}}$ the transition energy. The parameter η smooths the poles of the sum with a Lorentzian and can be interpreted as a phenomenological (inverse) lifetime broadening. The dipolar transition matrix elements $\Pi_{if,\mathbf{k}}^{\alpha}$ are determined by

$$\Pi_{fi,\mathbf{k}}^{\alpha} = \int \psi_{f,\mathbf{k}}^*(\mathbf{r}) \mathbf{p}^{\alpha} \psi_{i,\mathbf{k}}(\mathbf{r}) \, d\mathbf{r}. \quad (3.50)$$

The optical conductivity tensor and the dielectric tensor $\varepsilon_{\alpha\beta}(\omega)$ are related by

$$\varepsilon_{\alpha\beta}(\omega) = \delta_{\alpha\beta} + \frac{4\pi i}{\omega} \sigma_{\alpha\beta}(\omega) \quad (3.51)$$

with the Kronecker delta $\delta_{\alpha\beta}$; in the high-frequency limit, the diagonal components converge to 1 and the off-diagonal components go to zero. The x-ray absorption, x-ray magnetic circular dichroism, and x-ray magnetic linear dichroism of a cubic material with magnetization along the z-axis (which is not necessarily parallel to one of the crystal axes) can be calculated as

$$\text{XAS}(\omega) = \frac{1}{3} \text{Tr}[\text{Im}(\varepsilon(\omega))] \quad (3.52)$$

$$\text{XMCD}(\omega) = \text{Im}(\sigma_{xy}(\omega)) \quad (3.53)$$

$$\text{XMLD}(\omega) = \text{Im}(\varepsilon_{zz}(\omega) - \varepsilon_{xx}(\omega)). \quad (3.54)$$

This very general formulation is adopted in the Elk code, and also includes a spin-orbit correction term in the dipolar transition matrix elements. The code does not consider transitions from core orbitals, so that the orbitals of interest have to be described as valence by the local orbitals method.

3.4.3 SPRKKR

SPRKKR treats the x-ray absorption on a fully relativistic level, such that spin-orbit effects are naturally included. In the KKR formalism, it is convenient to

rewrite (3.48) using the identity

$$-\frac{1}{\pi} \text{Im} G(E) = \sum_f |\psi_f\rangle \langle \psi_f| \delta(E_f - E) \quad (3.55)$$

for the Green's function to obtain

$$\mu^\alpha(\omega) \propto \sum_i \langle \Phi_i | X_\alpha^* \text{Im} G(E_i + \omega) X_\alpha | \Phi_i \rangle \theta(E_i + \omega - E_F). \quad (3.56)$$

The Φ_i are the core level wave functions of the initial states, and $X_\alpha = -\frac{1}{c} \mathbf{j}_{\text{el}} \cdot \mathbf{A}_\alpha$ represents the coupling of the electronic current density to the radiation vector potential. X-ray absorption and circular dichroism are computed following their definitions:

$$\text{XAS}(\omega) = \frac{1}{2} (\mu^+(\omega) + \mu^-(\omega)) \quad (3.57)$$

$$\text{XMCD}(\omega) = \mu^+(\omega) - \mu^-(\omega). \quad (3.58)$$

3.4.4 The FEFF9 code

The FEFF9 code is an implementation of the relativistic real-space multiple-scattering Green's function method within the muffin-tin approximation [82]. Correspondingly, most of the mathematics described in 3.2.2 apply here as well. The muffin-tin approximation (not to be confused with the muffin-tin partitioning in FLAPW) assumes spherical potentials in the muffin-tins and a constant potential outside. The first versions of FEFF were designed to compute the extended x-ray absorption fine structure (EXAFS) of molecules and solids, which originates from multiple scattering of the excited photoelectron from the surrounding atoms. Therefore, it was naturally based on multiple-scattering theory, but employed a scattering path expansion for the Green's function:

$$G^{\text{sc}} = \bar{G}_0 T \bar{G}_0 + \bar{G}_0 T \bar{G}_0 T \bar{G}_0 + \dots \quad (3.59)$$

The Green's function of the system is given as the sum of the central (absorber) atom and the multiple-scattering contribution above, $G = G^c + G^{\text{sc}}$. The Green's function \bar{G}_0 refers to the damped free-electron Green's function, as calculated with a complex self-energy and core hole lifetime. The expansion is a very efficient and fast way to compute EXAFS, which are relevant at energies about 10 eV above the absorption threshold up to a few hundred eV.

For low energies, i.e., very distant scattering events, the convergence of the expansion is bad, such that the near-edge region (x-ray absorption near edge structure, XANES) is not described correctly. For this region, the full multiple-scattering (FMS) as described by Eq. (3.37) has to be considered. Further, a self-consistent potential is required for accurate results. Both the FMS as well as the self-consistency are implemented in FEFF9, allowing accurate XANES calculations. However, the spin treatment is not self-consistent. One has to impose a particular magnetic moment for a given site in the cluster, which is then adjusted by a rigid shift of spin up and down densities. The computation of circular dichroism is accordingly limited to cases, where the rigid shift is a good description of the actual band structure.

The major advantage of the FEFF code is a self-consistent treatment of core hole effects. The x-ray absorption can be described in the final state approximation, removing an electron from the initial state and adding it to the final states. This gives rise to a redistribution of the bands, often improving the agreement between experiment and calculation, in particular for K edges. It is difficult to treat these effects in reciprocal space methods (large supercells have to be constructed), whereas the treatment in a real space cluster approach is quite natural.

3.4.5 More Advanced Treatment of the Core-Hole–Photoelectron Interaction

As indicated above, self-consistent inclusion of a core hole improves agreement between experiment and calculation in many cases. However, this is just an approximate treatment of the excited state, and some problems remain. One of the most prominent examples of failure of the standard independent particle approximation (IPA) of x-ray absorption as outlined above is the $L_{3,2}$ absorption of $3d$ transition metals. Within the IPA, the branching ratio of the two absorption peaks corresponds to the statistical 2:1 ratio, due to the occupation of the $2p_{3/2}$ level with four electrons and of the $2p_{1/2}$ level with two electrons. However, in light $3d$ transition metals, such as Sc or Ti, this ratio is close to 1:1, whereas for Ni it is larger than the statistical ratio. More recent computation schemes go beyond the simple IPA and can partly resolve these problems.

Two major approaches to treat the core-hole–photoelectron interaction in a more sophisticated way have been developed: the time-dependent density functional theory (TD-DFT) and an explicit many-body perturbation the-

ory (MBPT) calculation with the Bethe-Salpeter-Equation. Neither of these approaches has been used in this work, but for completeness they shall be outlined briefly.

In the TD-DFT one finds the linear interacting density response function χ from a Dyson equation relating it to the non-interacting χ_S via

$$\chi(\mathbf{r}, \mathbf{r}', \omega) = \chi_S(\mathbf{r}, \mathbf{r}', \omega) + \int \int d^3x d^3x' \chi_S(\mathbf{r}, \mathbf{x}', \omega) K(\mathbf{x}, \mathbf{x}', \omega) \chi(\mathbf{x}', \mathbf{r}', \omega). \quad (3.60)$$

Here, the TD-DFT Kernel K has been introduced, which consists of the Coulomb interaction and a frequency-dependent exchange-correlation kernel:

$$K(\mathbf{r}, \mathbf{r}', \omega) = \frac{1}{|\mathbf{r} - \mathbf{r}'|} + f_{xc}(\mathbf{r}, \mathbf{r}', \omega). \quad (3.61)$$

Similarly as in the DFT, the major problem here is to approximate the unknown exchange-correlation kernel f_{xc} . Different approximations have been proposed, with varying success [83, 84, 85]. To date, no universal Kernel is known that is equally well suited for all systems of interest.

The Bethe-Salpeter-Equation (BSE) is derived from many-body perturbation theory, and is commonly written as an eigenvalue problem in reciprocal space [86]:

$$\sum_{h'e'k'} H_{hek,h'e'k'}^{e-h} A_{h'e'k'}^\lambda = E^\lambda A_{hek}^\lambda. \quad (3.62)$$

The electron-hole interaction Hamiltonian consists of a diagonal part, a direct (Coulombic) term and an exchange term,

$$H^{e-h} = H^{\text{diag}} + H^{\text{dir}} + H^{\text{x}}, \quad (3.63)$$

which can be expressed as

$$H_{hek,h'e'k'}^{\text{diag}} = (\varepsilon_{hk} - \varepsilon_{ek}) \delta_{hh'} \delta_{ee'} \delta_{kk'}, \quad (3.64)$$

$$H_{hek,h'e'k'}^{\text{dir}} = - \int d^3r d^3r' \psi_{hk}(\mathbf{r}) \psi_{ek}^*(\mathbf{r}') W(\mathbf{r}, \mathbf{r}') \psi_{h'k'}^*(\mathbf{r}) \psi_{e'k'}(\mathbf{r}'), \quad (3.65)$$

$$H_{hek,h'e'k'}^{\text{x}} = \int d^3r d^3r' \psi_{hk}(\mathbf{r}) \psi_{ek}^*(\mathbf{r}) \bar{v}(\mathbf{r}, \mathbf{r}') \psi_{h'k'}^*(\mathbf{r}') \psi_{e'k'}(\mathbf{r}'), \quad (3.66)$$

with the Kohn-Sham eigenvalues $\varepsilon_{(e,h),k}$, the screened Coulomb potential $W(\mathbf{r}, \mathbf{r}')$ and the short-range part of the bare Coulomb potential $\bar{v}(\mathbf{r}, \mathbf{r}')$ [86].

The imaginary part of the dielectric function is calculated from the eigenvalues E^λ and the coupling coefficients $A_{h\mathbf{k}}^\lambda$:

$$\text{Im } \varepsilon^{xx}(\omega) = \frac{8\pi}{\Omega} \sum_{\lambda} \left| \sum_{h\mathbf{k}} A_{h\mathbf{k}}^\lambda \frac{\langle h\mathbf{k} | -i\nabla_x | e\mathbf{k} \rangle}{\varepsilon_{c\mathbf{k}} - \varepsilon_{h\mathbf{k}}} \right|^2 \cdot \delta(E^\lambda - \omega) \quad (3.67)$$

The BSE gives a physically transparent picture of the absorption process: excitonic effects, i.e. excited states in the band gap of insulators, are due to the direct term (describing the Coulomb attraction of the valence states by the core-hole); spectral weight transfers, as in the above mentioned case of $L_{3,2}$ absorption, are caused by the exchange term, which mixes the various transition channels [86]. The excitonic effects are partly accounted for by the final state approximation.

The BSE is currently the state-of-the-art treatment of the optical and x-ray absorption process. However, its use is restricted to small systems with a few atoms, because the calculation of the matrix elements in the BSE Hamiltonian and its diagonalization are very cumbersome.

4 Ab initio prediction of ferrimagnetism, exchange interactions and Curie temperatures in Mn_2TiZ Heusler compounds

4.1 Introduction

In this chapter, *ab initio* calculations of the properties of the (hypothetical) Mn_2TiZ compounds, crystallized in the $L2_1$ structure, are discussed. No experimental data are available for this system, and only Mn_2TiAl has been studied theoretically before [87]. However, it is expected that parts of this series will exist in the $L2_1$ structure, seeing that Mn_2VAl and Mn_2VGa , as well as parts of the Co_2TiZ series have been prepared [79, 88, 89].

The calculations presented in this study were performed within two different density functional theory-based band structure codes: the full-potential linearized augmented plane waves (FLAPW) package Elk (Chapter 3.2.1) and the full-potential Korringa-Kohn-Rostoker *Munich* SPRKKR package (Chapter 3.2.2). Although both methods are in principle equivalent for crystalline systems, there are subtle differences associated with their numerical implementations, and thus it is worth to compare both methods on the rather complex intermetallic system Mn_2TiZ .

Elk was used to determine the theoretical lattice parameters and the total energy differences between ferrimagnetic and nonmagnetic states. These calculations were carried out on a $12 \times 12 \times 12$ \mathbf{k} point mesh (72 points in the irreducible wedge of the Brillouin zone). The muffin-tin radii of all atoms were set to 2.0 a.u. to avoid overlaps at small lattice parameters. The equilibrium lattice parameters a were determined using a third-degree polynomial fit to the total energies. To obtain accurate magnetic moments and densities of states, the calculations were performed at the equilibrium lattice parameter using a $16 \times 16 \times 16$ \mathbf{k} -mesh (145 points in the irreducible wedge) and nearly touching muffin-tin spheres.

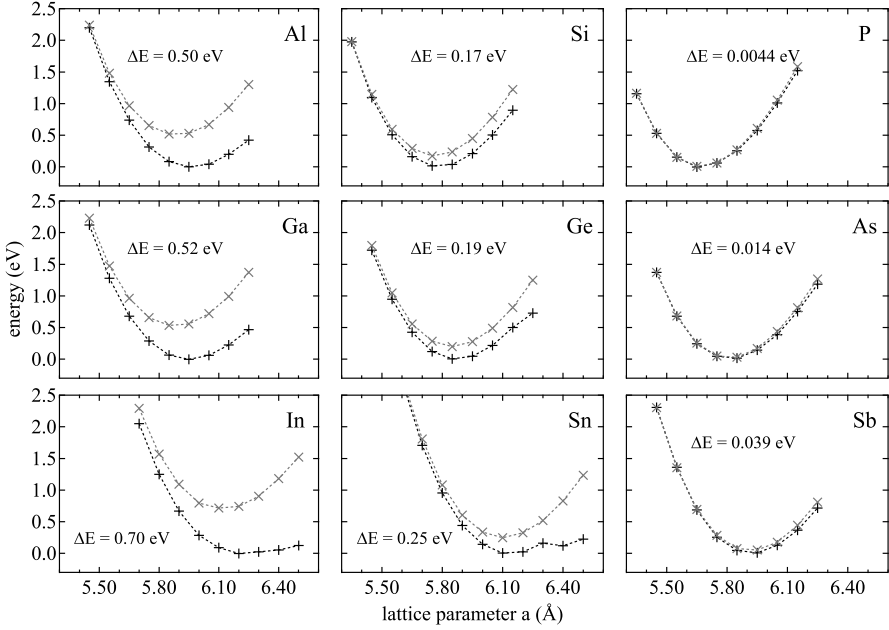


Figure 4.1: Total energies of the investigated compounds in dependence of their lattice parameters. The results for the ferrimagnetic and the non-magnetic states are represented with + and ×, respectively.

The SPRKKR calculations were performed on the theoretical equilibrium lattice parameters determined with Elk. The calculations were carried out in the full-potential mode with an angular momentum cutoff of $l_{max} = 3$ on a $22 \times 22 \times 22$ \mathbf{k} point mesh (289 points in the irreducible wedge of the Brillouin zone). Both the full potential as well as the increased angular momentum cutoff are necessary to ensure accurate results. The DOS were calculated on a denser mesh of 1145 \mathbf{k} points with 0.5 mRy added as the imaginary part to the energy.

The exchange-correlation potential was modeled within the generalized gradient approximation of Perdew, Burke, and Ernzerhof in both schemes [69]. The calculations were converged to about 0.1 meV. All calculations were carried out in the scalar-relativistic representation of the valence states, thus neglecting the spin-orbit coupling.

Heisenberg pair exchange coupling parameters and MFA Curie temperatures were obtained as described in Chapter 3.3. In order to separate the two Mn lattices, the calculations were run in $F\bar{4}3m$ space group, in which the Mn atoms are not equivalent by symmetry. The \mathbf{r} -summation in Eq. (3.46) was taken to a radius of $R_{\max} = 3.0 a$, which has been shown to be sufficient for half-metallic Heusler compounds [90, 80].

4.2 Results

4.2.1 Energy minimization and lattice parameters

Three types of magnetic starting configurations were tested: ferro-, ferri-, and nonmagnetic. It was found for all compounds that the ferromagnetic configurations were unstable and converged into the ferrimagnetic state. Fig. 4.1 displays the total energies of the ferrimagnetic and the nonmagnetic configurations in dependence on the lattice parameters a . We find that the ferrimagnetic state has always lower energy than the non-magnetic state; the difference in total energy reduces with increasing number of valence electrons, but it increases within the groups with the atomic number. The lattice parameters follow roughly a linear dependence on the atomic radius of the Z element with

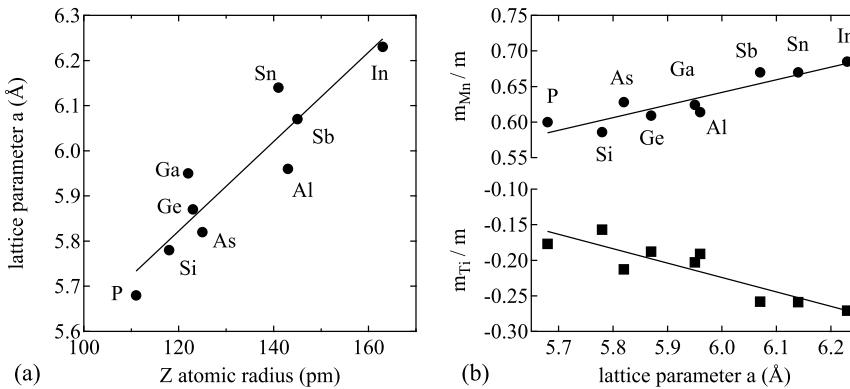


Figure 4.2: (a): Dependence of the lattice parameter a on the atomic radius of the Z element. (b): Normalized magnetic moments of Mn and Ti in dependence of the lattice parameter.

Mn_2TiZ	Elk					SPRKKR			
	a (Å)	m	m_{Mn}	m_{Ti}	P (%)	m	m_{Mn}	m_{Ti}	P (%)
Al	5.96	2.98	1.83	-0.57	21	2.98	1.76	-0.49	82
Ga	5.95	2.95	1.84	-0.60	45	2.97	1.77	-0.53	79
In	6.23	3.17	2.17	-0.86	7	3.08	1.98	-0.82	32
Si	5.78	1.98	1.16	-0.31	94	1.98	1.13	-0.26	87
Ge	5.87	1.97	1.20	-0.37	94	1.97	1.16	-0.33	89
Sn	6.14	1.97	1.32	-0.51	97	2.00	1.25	-0.48	93
P	5.68	0.30	0.18	-0.05	-3	—	—	—	—
As	5.82	0.94	0.59	-0.20	84	0.97	0.61	-0.22	58
Sb	6.07	0.97	0.65	-0.25	88	0.98	0.62	-0.24	79

Table 4.1: Results of the ground state properties calculations with Elk and SPRKKR. The total magnetic moments are given in μ_B per formula unit, the atomic magnetic moments are given in μ_B per atom. The SPRKKR results for Mn_2TiAs were obtained with $a = 5.95$ Å (see text).

the correlation coefficient of $r = 0.92$ (Fig. 4.2 (a)). Some compounds show a strong asymmetry of the total energy curve in the ferrimagnetic configuration and even kinks in the curves for very large a . This is caused by a steep increase of the magnetic moments for increasing a which causes a stronger binding. However, this effect is never strong enough to shift the equilibrium lattice parameter to such a high- m state. The equilibrium lattice parameters are summarized in Table 4.2.1. Typically we find the equilibrium lattice parameters of Heusler compounds obtained with Elk to be accurate within $\pm 0.5\%$ compared to experiment.

4.2.2 Magnetic moments and densities of states

The results of this subsection are summarized in Table 4.2.1 and Fig. 4.3.

Mn_2TiAl , Mn_2TiGa , Mn_2TiIn

From the rule $m = N_V - 24$ we expect to find a magnetic moment of $3 \mu_B / f.u.$ for these compounds. The FLAPW calculations show small deviations from this rule, indicating that the compounds are not perfect half-metals. This is

confirmed by the DOS, which show spin polarizations at the Fermi level below 50 %, and in particular only 7 % for Mn_2TiIn , where the magnetic moment is enhanced to $3.17 \mu_{\text{B}}/\text{f.u.}$. This arises from the large lattice parameter and the fact that all three compounds do not form a gap in the DOS. The Fermi level for Mn_2TiAl and Mn_2TiGa is in a region with low DOS for both spin channels (see insets in Fig. 4.3), but both of them have a very large empty minority spin DOS right above E_{F} . Small variations of the lattice parameter would thus lead to strong variations of the spin polarization.

The calculations performed with SPRKKR reproduce the magnetic moments obtained in Elk very well. Although the total moments are practically equal, a larger deviation is found for the atom-resolved moments. The Fermi energy is found at slightly different positions in the DOS, and the detailed structures observed in Elk around E_{F} are less pronounced, especially the dip in the spin-down states at E_{F} . This leads to significantly higher spin polarization values in SPRKKR. However, the trend that Mn_2TiIn has the lowest polarization within this group is reproduced.

Mn_2TiSi , Mn_2TiGe , Mn_2TiSn

According to the “rule of 24” a total magnetic moment of $2 \mu_{\text{B}}/\text{f.u.}$ is expected. Again, small deviations from this rule are observed; all moments are lower by about 1.5 %. In Elk, the three compounds are found to form a half-metallic gap in the majority spin states slightly above E_{F} . The gap onset above E_{F} (width) is 0.16 eV (0.49 eV) for Si, 0.24 eV (0.25 eV) for Ge, and 0.19 eV (0.01 eV) for Sn. Nevertheless, the spin polarization is above 90 % in these calculations. The structure of the DOS around E_{F} leads to a stable spin polarization and magnetic moment upon isotropic lattice compression or expansion. For this series, having the same valence electron counts and nearly half-metallic DOS, one can observe clearly a narrowing of the bands, i.e., the DOS are contracted towards E_{F} , while the Fermi level itself moves upwards. This is directly associated with the gradually increasing lattice parameter in this series, which reduces the overlap of the 3d orbitals and thereby reduces the itinerancy of the system. An increased localization of the electrons provides also an explanation for the increasing atomic magnetic moments along this series. Similar behavior has been observed earlier for Co_2MnZ , with $Z = \text{Si, Ge, Sn}$ [91, 92] and Ni_2MnSn [93]. In the first case the Mn moment is increased and the Co moment is lowered along the series, keeping the total moment integer. Calculations on Co_2MnSi with increased lattice parameter reproduced this behavior. In the

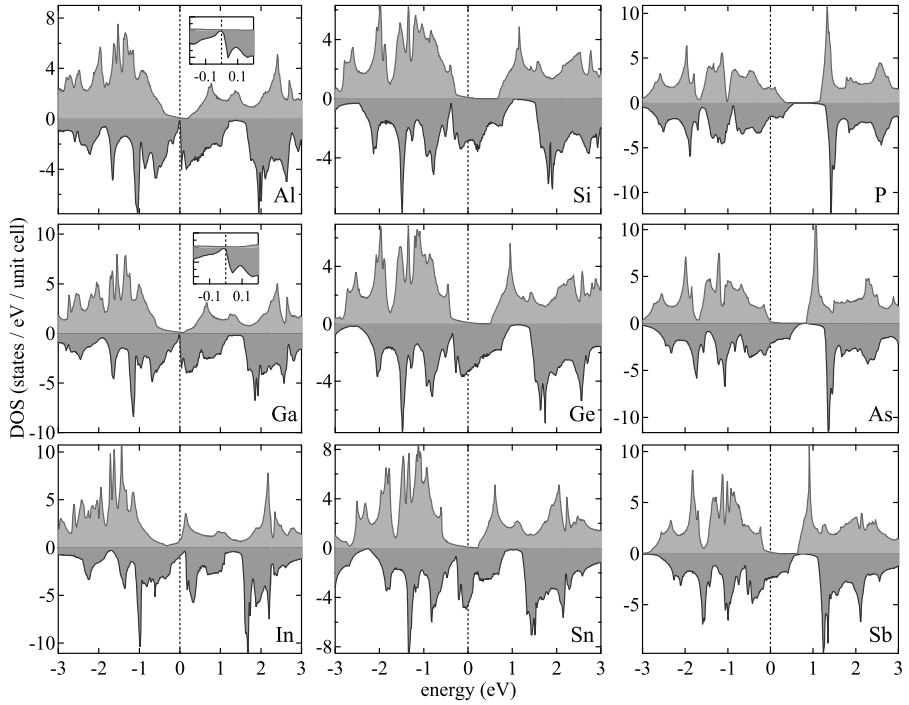


Figure 4.3: Densities of states calculated with Elk. The majority DOS is pointing up, the minority DOS is pointing down. The insets for Al and Ga show the region around the Fermi energy.

second case, the pressure dependence of the moments was studied. Under increasing pressure, i.e., with reduced lattice parameter, both the Ni and the Mn moment decrease, and thus the total moment decreases. However, Ni_2MnSn is not a half-metal, hence the total moment is not restricted to an integer value. Consequently, both observations on quite different ferromagnetic Heusler compounds are in accord with our case of (nearly) half-metallic ferrimagnetic Heusler compounds.

The magnetic moments and DOS from SPRKKR are in very good agreement with the ones obtained from Elk. However, the Fermi level is found at a lower position, giving rise to the slightly reduced polarization values.

Mn₂TiP, Mn₂TiAs, Mn₂TiSb

In these cases a total magnetic moment of only $1 \mu_B/\text{f.u.}$ is expected. Because of the very small lattice parameter of Mn₂TiP, its spin-splitting is small with only $0.3 \mu_B/\text{f.u.}$ in the Elk calculation. The situation of Mn₂TiAs and Mn₂TiSb is similar to that of Mn₂TiSi and Mn₂TiGe. A majority spin gap is formed above the Fermi level with onset (width) of 0.29 eV (0.53 eV) for As and 0.19 eV (0.44 eV) for Sb. Though not being half-metallic, both compounds have spin polarizations of more than 80 %.

Finally, the magnetic moments of Mn₂TiSb in SPRKKR agree very well with those obtained with Elk. But again, the Fermi level is lower and the spin polarization is reduced. For Mn₂TiP and Mn₂TiAs the situation is quite different. They can not be converged into ferrimagnetic states at the equilibrium lattice parameters determined by Elk; instead, they are found to be nonmagnetic. This is caused by the tiny energy difference between the ferrimagnetic and the nonmagnetic configuration, which leads to a numerical instability of the ferrimagnetic state. By increasing the lattice parameter of Mn₂TiAs by about 2 % to 5.95 Å, the separation is increased artificially to about 30 meV/f.u. and the calculation converges into the ferrimagnetic state. Because of this, the properties obtained with SPRKKR for this compound have to be taken with care: in all other cases the individual atomic moments are slightly lower in SPRKKR than those from Elk; here instead, larger moments are found. However, the same procedure can not be applied to Mn₂TiP, within a reasonable range of lattice parameters.

General remarks

It is worth to note that the magnetic moments of the *Z* component are always below $0.06 \mu_B$ and that they are always parallel to the Ti moment. In detail, the values are Al $0.044 \mu_B$, Ga $0.052 \mu_B$, In $0.058 \mu_B$, Si $0.034 \mu_B$, Ge $0.035 \mu_B$, Sn $0.034 \mu_B$, P $0.0062 \mu_B$, As $0.018 \mu_B$, and Sb $0.017 \mu_B$.

Another property worth noting is the fact that the ratios m_{Mn}/m and m_{Ti}/m follow a linear dependence (with correlation coefficients of $r \approx 0.9$ in both cases for the Elk data) on the lattice parameter (and hence the interatomic distances) independently on the *Z* type, see Fig. 4.2 (b). As mentioned above, with increasing lattice parameter the itinerant character of the system is reduced and localizes the moments gradually on the atoms. Therefore, the influence of the *Z* component in Mn₂TiZ is twofold. First, it determines the lattice

parameter of the compound and following from that, the degree of electron localization. And second, the total magnetic moment is determined via the number of electrons supplied, if the lattice parameter does not exceed a certain range (which is not the case for P and In).

4.2.3 Exchange interactions and Curie temperatures

The exchange interactions are investigated here for Mn_2TiGa , Mn_2TiGe , and Mn_2TiSb , which are representative compounds for their respective Z group. Fig. 4.4 (a) displays the J_{ij} calculated for the intra-sublattice interaction $Mn^{1(2)}-Mn^{1(2)}$ and the inter-sublattice interactions $Mn^{1(2)}-Mn^{2(1)}$ and Mn-Ti of the three compounds. All other interactions are very small and can be neglected for the following discussion.

In all three cases it is clear that the $Mn^{1(2)}-Mn^{2(1)}$ inter-sublattice interaction provides the largest contribution to the exchange. Further, the nearest neighbor interaction of Mn-Ti is always negative, hence all compounds are ferrimagnets. All interactions are mostly confined within a radius of $1.5a$. Apart from these similarities, there are many interesting differences.

First, we discuss the details of the dominating inter-sublattice interaction $Mn^{1(2)}-Mn^{2(1)}$. The first and second nearest neighbors provide a large, positive exchange. The second nearest neighbors have two different values of J_{ij} . This is a feature that is not observed in frozen-magnon calculations (see, e.g. [43]), because the Fourier transform that is necessary to obtain the exchange parameters involves a spherical averaging. Instead, with the real-space approach used here we observe a difference for Mn atoms with a Ti atom or a Z atom in between. We found larger values on the Mn atoms mediated via Ti and lower values on the Z mediated ones. The nearest Mn neighbors have a distance of about 2.95 \AA , and the exchange is apparently indirect. For direct exchange, one would expect a scaling with the magnetic moments, which is not observed here. It rather oscillates with the sp electron number. A similar result has been obtained earlier on other half and full Heusler compounds [94]. The ratio of the nearest and second nearest neighbor coupling is significantly reduced with increasing electron concentration, and the nearest neighbor interaction dominates in Mn_2TiSb .

The antiferromagnetic Mn-Ti interaction is only significant for the nearest neighbors. Accordingly, the interaction between Mn and Ti, which have a distance of about 2.55 \AA , is essentially given by direct exchange coupling and the scaling with the Ti moment corroborates this assumption.

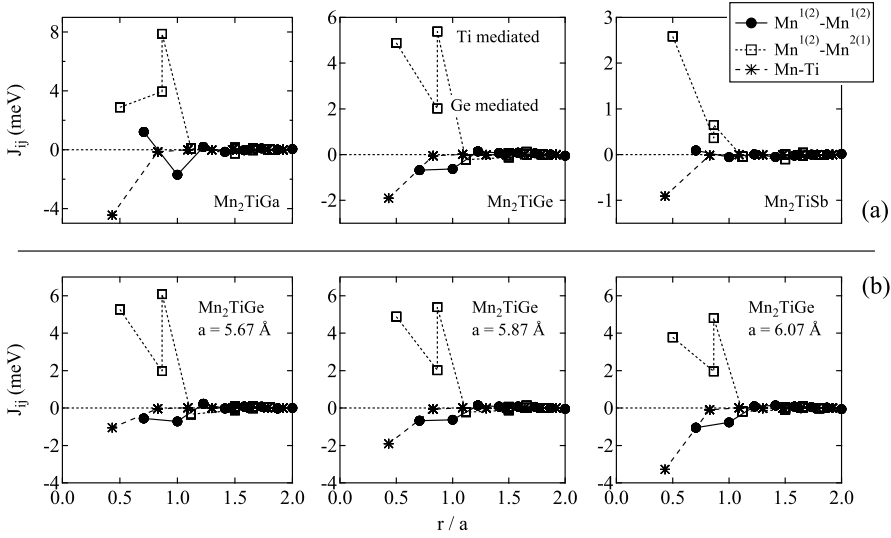


Figure 4.4: Heisenberg exchange parameters J_{ij} in dependence on the normalized distance r/a . (a): J_{ij} for Mn_2TiGa , Mn_2TiGe , Mn_2TiSb for their respective equilibrium lattice parameters. (b): J_{ij} for Mn_2TiGe with different lattice parameters. Note the different scales of the vertical axes in the top row.

The intra-sublattice interaction of $\text{Mn}^{1(2)}-\text{Mn}^{1(2)}$ exhibits a notable oscillatory behavior. In the two cases with odd valence electron number it is positive for the nearest neighbors, negative for the second, and again positive for the third nearest neighbors. For Mn_2TiGe with its even electron count the first two neighbors have negative and the third neighbor has positive interaction. So in the latter case, the total Mn-Mn intra-sublattice interaction is effectively antiferromagnetic.

In order to study the dependence of J_{ij} on the lattice parameter as a possible explanation for the differences discussed above, additional calculations on Mn_2TiGe have been performed with lattice parameters of $(5.87 \pm 0.2) \text{ \AA}$. This compound was chosen because of the wide (pseudo-)gap for the spin-up states, which warrants a stable total magnetic moment and minimal band structure effects over the range of a used here.

The results from these calculations are given in Fig. 4.4 (b). Obviously, the changes here are rather subtle and can not account for the the large differ-

ences discussed above. However, we note a reduction of the nearest neighbor $Mn^{1(2)}-Mn^{2(1)}$ interaction and of the Ti mediated second nearest $Mn^{1(2)}-Mn^{2(1)}$ neighbor. Meanwhile, the Mn-Ti interaction increases, in agreement with increased Mn and Ti moments.

The strong confinement of the exchange interactions to a sphere with a radius of about $1.5a$ is reflected in the Curie temperature calculated as a function of the cluster radius which is nearly converged at $r \gtrsim 1.5a$, see Fig. 4.5 (a). At larger radii a weak oscillation of T_C^{MFA} is observed, indicating long-ranged RKKY-like behaviour.

A deeper discussion of the exchange interaction is beyond the scope of this work. However, it was recently shown for numerous half and full Heusler compounds that various exchange mechanisms—such as RKKY, superexchange and Anderson s-d mixing—contribute to the indirect exchange interactions [94].

The relevant contributions to the J_0 matrix in Eq. (3.46) are displayed in Fig. 4.5 (b). In agreement with the previous discussion it is found that the inter-sublattice interaction $Mn^{1(2)}-Mn^{2(1)}$ provides the largest contribution, followed by the Mn-Ti interaction, which can become as large as the $Mn^{1(2)}-Mn^{2(1)}$ interaction in Mn_2TiIn . The intra-sublattice interaction $Mn^{1(2)}-Mn^{1(2)}$ is generally weak, positive for Al, Ga, In, and negative for Si, Ge, Sn. All other inter- and intra-sublattice contributions are below 1 meV. A negative intra-sublattice contribution means that the interaction acts against the ferromagnetic order on this lattice and thus reduces the Curie temperature.

Table 4.2 summarizes our calculated Curie temperatures. They are well above room temperature for the compounds with 21 and 22 valence electrons, but considerably lower for Mn_2TiAs and Mn_2TiSb . The Curie temperature scales roughly linear with the total magnetic moment. Within one group, the Curie temperatures are comparable, though a trend to decrease with increasing atomic number of the Z component is clear for 21 and 22 valence electrons.

The Curie temperatures of Mn_2TiAl , Mn_2TiGa and Mn_2TiIn are quite similar. The slightly reduced T_C^{MFA} of Mn_2TiIn is caused by the steep reduction of

Mn_2TiZ	Al	Ga	In	Si	Ge	Sn	P	As	Sb
T_C^{MFA} (K)	665	663	630	424	398	354	—	132	156

Table 4.2: Curie temperatures T_C^{MFA} calculated in the mean-field approximation.

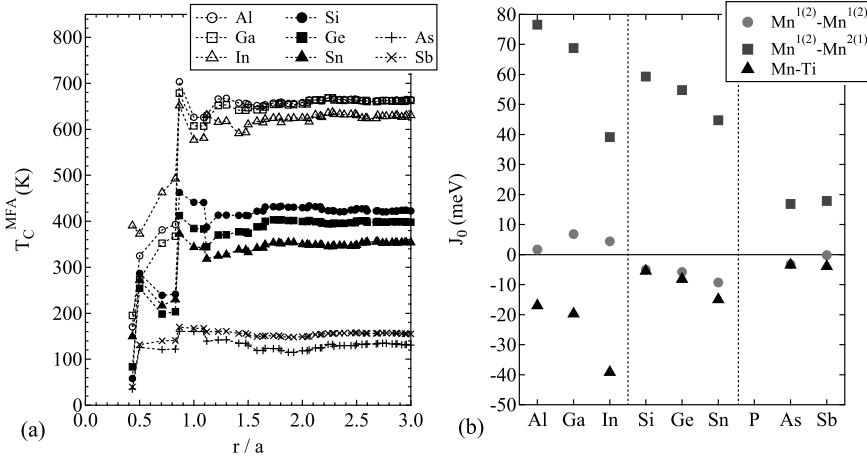


Figure 4.5: (a): The Curie temperature T_C^{MFA} in dependence on the normalized cluster radius r/a taken into the summation. (b): r -summed exchange coupling parameters J_0 .

the $\text{Mn}^{1(2)}\text{-Mn}^{2(1)}$ interaction. On the other hand, a simultaneous increase of the Mn-Ti interaction stabilizes T_C^{MFA} at a still high level (see Fig. 4.4 (b)). In the series $\text{Mn}_2\text{TiSi} - \text{Mn}_2\text{TiGe} - \text{Mn}_2\text{TiSn}$ the $\text{Mn}^{1(2)}\text{-Mn}^{2(1)}$ interaction decreases, but here the increase of the Mn-Ti interaction can not compensate this and hence the Curie temperature decreases. In any case, the $\text{Mn}^{1(2)}\text{-Mn}^{2(1)}$ interaction provides the dominant contribution to T_C^{MFA} , only in Mn_2TiIn the Mn-Ti interaction is dominant. The significantly lower Curie temperature of Mn_2TiAs with respect to Mn_2TiSb can be attributed to the artificially increased lattice parameter used in the calculation.

The dependence of the exchange parameters and T_C^{MFA} on the lattice constant was studied for Mn_2TiGe . The corresponding terms of the J_0 matrix, the Curie temperature and the magnetic moments are presented in Fig. 4.6 (a)-(c). A decrease of the $\text{Mn}^{1(2)}\text{-Mn}^{2(1)}$ interaction and simultaneously of T_C^{MFA} with increasing a is observed, although both m_{Mn} and m_{Ti} increase. Obviously, the individual moments play only a minor role in the exchange and the interatomic distances are more important. The Mn-Ti as well as the $\text{Mn}^{1(2)}\text{-Mn}^{1(2)}$ interactions become stronger with increasing a , but they nearly compensate each other. In agreement with a direct exchange coupling, the Mn-Ti interaction scales with the magnetic moments. The changes in J_0 reproduce very well the

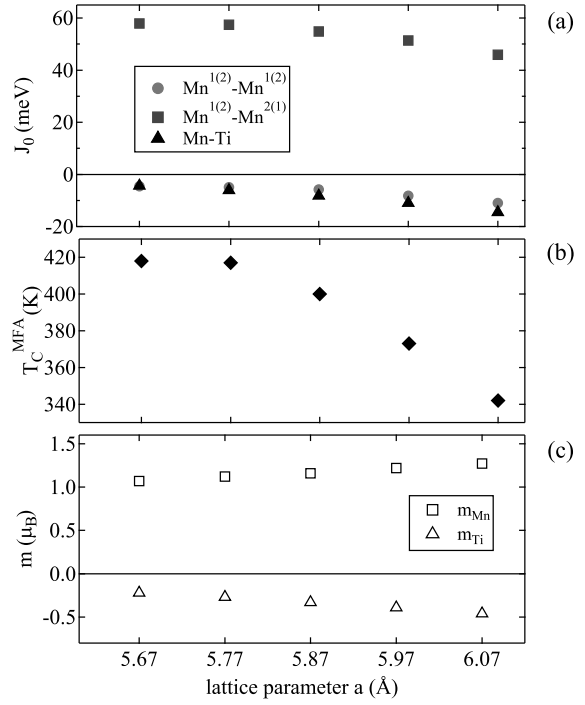


Figure 4.6: Dependence of J_0 (a), T_C^{MFA} (b) and magnetic moments (c) on the lattice parameter in Mn_2TiGe .

changes observed in Fig. 4.5 (b) for the Si – Ge – Sn series.

Put in terms of a pressure dependence, we observe $dT_C / dp > 0$, i.e., the Curie temperature increases with increasing pressure. Kanomata *et al.* proposed an empirical interaction curve for Ni_2MnZ and Pd_2MnZ full Heusler compounds that suggests $dT_C / dp > 0$ for these compounds [95]. The origin of this behavior is attributed to the Mn-Mn distance and the indirect exchange between the Mn atoms, which fully carry the magnetism of the compounds. Hence, all other interactions can be neglected. A numerical confirmation by first principles of this interaction curve was given recently [93]. For half-metallic Heusler compounds of type Co_2YZ Kübler *et al.* analyzed the dependence of T_C on the valence electron number, which is approximately linear, and scales thus with the total magnetic moment [96]. Further it was also proposed for Co_2MnZ compounds to have $dT_C / dp > 0$, although the Co atom participates significantly in the exchange interactions [92]. Experimentally this dependence on the lattice parameter was even observed for the Co_2TiZ series

(with $Z = \text{Si, Ge, Sn}$), where the Ti atoms have nearly vanishing magnetic moment [88].

Interestingly, the magnetic moments of Mn and Ti in Mn_2TiGe vary within the same range as the moments for different compounds shown in Fig. 4.2(b), while the total moment remains fixed at $2 \mu_{\text{B}} / \text{f.u.}$ These findings demonstrate the strong influence of the lattice parameter, while the details of the electronic structure of the Z element are less important. Consequently, the Z element influences the properties of the Mn_2TiZ compound mainly via its number of valence electrons and its atomic radius, which determines the equilibrium lattice parameter.

5 Exchange interactions and Curie temperatures of Mn_2CoZ compounds

5.1 Introduction

In the literature it has been noted that the Mn_2YZ inverse Heusler compounds with Hg_2CuTi structure are dominated by direct exchange between the nearest neighbor Mn atoms, but direct calculations of the exchange interactions are missing. It is the scope of this chapter to provide these calculations for the Mn_2CoZ compounds. We focus on this compound series because it has been experimentally synthesized, and band structure calculations suggested very large atomic moments and half-metallicity in most cases.

The half-metallicity of Mn_2CoZ is constituted by two processes [28]. First, a broad covalent gap of Mn(B) is created by covalent hybridization with Co and Mn(C), which form the (double tetrahedral) nearest neighbor shell. However, the final size of the minority gap is determined by the e_u-t_{1u} splitting in the hybridization of Co and Mn(C), which form each other's (octahedral) second nearest neighbor shells. Mn(B) states do not contribute to this hybridization because of the different symmetry transformations. Thus, the band gap is a $d-d$ gap [97]. This situation is similar to the one in the Co_2MnZ Heusler compounds, where the e_u-t_{1u} splitting of the Co-Co hybridization governs the minority gap [23].

The calculations were performed with the spin-polarized relativistic Korringa-Kohn-Rostoker package *Munich SPRKKR*, see Chapter 3.2.2. The calculations were carried out in the full-potential mode with an angular momentum cutoff of $l_{\text{max}} = 3$ on a $28 \times 28 \times 28$ \mathbf{k} point mesh (564 points in the irreducible wedge of the Brillouin zone). In order to further improve the charge convergence with respect to l_{max} , we employed Lloyd's formula for the determination of the Fermi energy [74, 75]. The exchange-correlation potential was modeled within the generalized gradient approximation of Perdew, Burke, and Ernzerhof [69]. All calculations were carried out in the scalar-relativistic representation of the valence states, thus neglecting the spin-orbit coupling.

Mn ₂ CoZ	a (Å)	m_{total}	m_{Co}	$m_{\text{Mn(B)}}$	$m_{\text{Mn(C)}}$	m_Z
Al	5.84	1.99	0.94	2.69	-1.59	-0.05
Ga	5.86	2.01	0.93	2.88	-1.78	-0.03
In	6.04 ^a	1.95	0.99	3.16	-2.18	-0.02
Si	5.70	2.99	0.84	2.66	-0.50	-0.01
Ge	5.80	2.98	0.87	2.83	-0.72	0.01
Sn	5.96 ^a	2.98	0.83	2.96	-0.81	-0.01
Sb	5.90	3.97	0.88	2.95	0.15	0.00

^a exp. lattice parameters: Mn₂CoIn 6.14 Å, Mn₂CoSn 6.06 Å

Table 5.1: Lattice parameters used for the calculations and resulting total and site resolved magnetic moments. The total magnetic moments are given in μ_B per formula unit, the atomic magnetic moments are given in μ_B per atom.

Heisenberg pair exchange coupling parameters and MFA Curie temperatures were obtained as described in Chapter 3.3. The r -summation in Eq. (3.46) was taken to a radius of $r_{\text{max}} = 3.0a$, where a is the lattice constant.

The lattice parameters were taken from Liu *et al.* [28], who provide experimental values for $Z = \text{Al, Ga, In, Ge, Sn, Sb}$. For Mn₂CoSi we assumed the Mn₂CoGe parameter reduced by 0.1 Å, which is observed, e.g., for Co₂MnSi – Co₂MnGe [51]. The calculations of Mn₂CoIn and Mn₂CoSn were unstable at the experimental lattice parameters, but could be stabilized with slightly reduced values. All lattice parameters used here are summarized in Table 5.1.

5.2 Results

5.2.1 Magnetic moments

The electronic structure calculations yield a half-metallic ground state in all cases with the exception of Mn₂CoGa and Mn₂CoIn. Our results for the total and site resolved magnetic moments are summarized in Table 5.1. The total magnetic moments closely follow the Slater-Pauling rule for half-metallic Heusler compounds, so that we have magnetic moments of 2, 3, or 4 μ_B / f.u. if Z is a group III, IV, or V element, respectively. Small deviations from the integer values arise from the angular momentum truncation at $l_{\text{max}} = 3$, which

gives rise to a very small DOS in the minority gap. This is a typical observation when using the KKR method on ferromagnetic half-metals (see, e.g., Galanakis *et al.* [23]). The magnetic moment of the Co atom is nearly constant for different Z materials, being about $0.9 \mu_B$. Similarly, the Mn(B) atom has a nearly constant magnetic moment in the range of 2.69 to $3.16 \mu_B$. In contrast, the moment of the Mn(C) atom changes considerably with the valence electron number and determines finally the total moment. All Mn_2CoZ compounds are ferrimagnetic due to the Mn(C) atom with the exception of Mn_2CoSb , which is a ferromagnet. In all cases the Z atom is nearly unpolarized. Only small changes are observed for the site resolved moments when Z is changed within one group. The increase of the absolute value of the Mn moments within one group can be traced to the lattice parameter change upon Z change. The orbital overlap is reduced with increasing lattice parameter, giving rise to weaker hybridizations (which is also the reason for the gap width reduction). Because of this reduction of itinerancy the quenching of the atomic moments is less effective and the moments become more atomic-like, i.e., larger. This situation is similar to the one described in Chapter 4.

Our results differ considerably from those given by Liu *et al.* [28], who used the full potential linearized augmented plane waves (FLAPW) method. The total magnetic moments are in very good agreement, but the atomic moments are smaller in our calculations by 0.3 to $0.7 \mu_B$ for Mn(B) and Mn(C). In contrast, the magnetic moments of the Co atoms are nearly equal. Most notably, in our calculations Mn_2CoSb is ferro- instead of ferrimagnetic. Therefore, we have checked our SPRKKR results with the FLAPW package Elk [70]. Our FLAPW results are concordant with the SPRKKR data, leaving the discrepancies with Liu *et al.* unexplained.

Apart from these differences, the DOS are in good agreement with [28] and all conclusions about the electronic structure given there are transferable to our calculations.

5.2.2 Exchange interactions and Curie temperatures

Figure 5.1 shows the Heisenberg exchange coupling parameters obtained from our calculations. To ease the following discussion, refer to Table 5.2 for the atomic coordinations.

We start with the discussion of the Al–Ga–In series. It is notable that the exchange interactions are tightly confined to clusters of radius $r \leq a$. In particular, the inter-sublattice interactions have significant contributions only for the

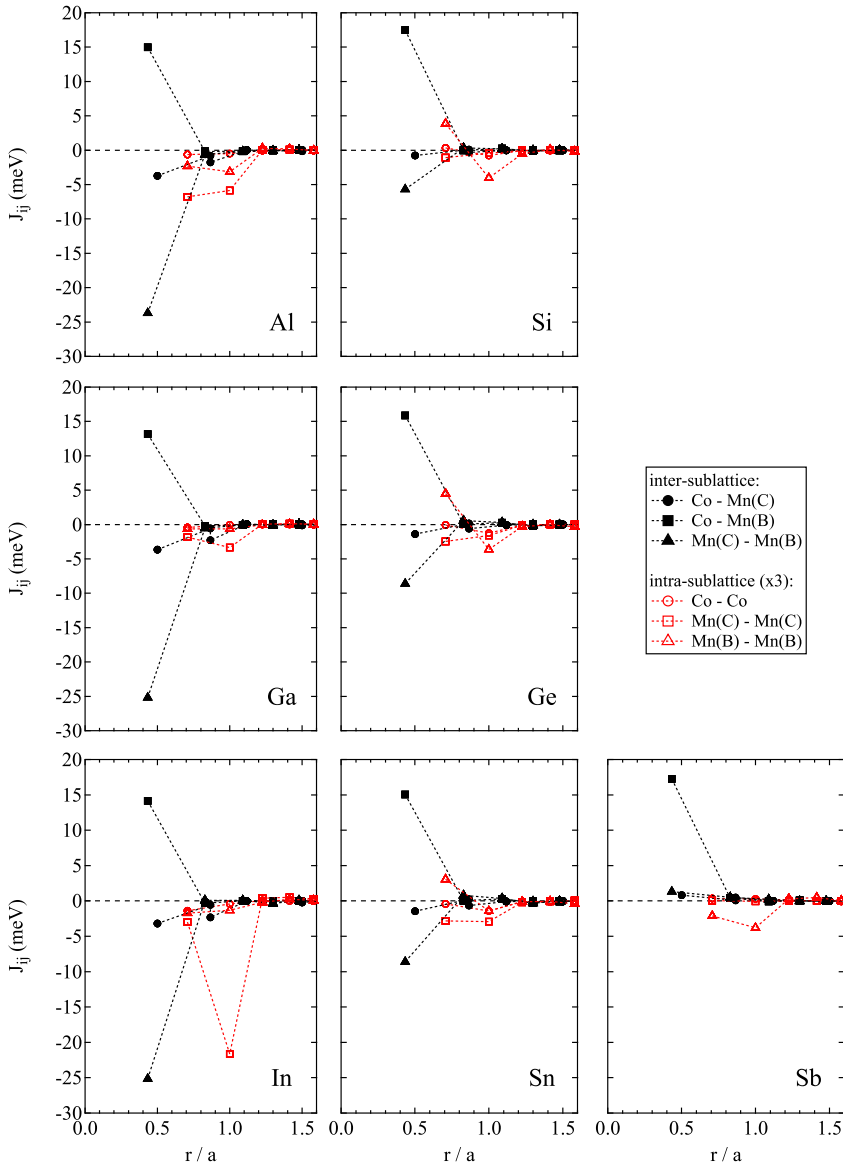


Figure 5.1: Heisenberg exchange coupling parameters J_{ij} for the Mn_2CoZ compounds as a function of the interatomic distance r . Note that the intra-sublattice interactions have been multiplied by 3 for clarity.

distance (r/a)	0.433	0.50
symmetry	T_d	O_h
Co	Mn(B) / Z	Mn(C)
Mn(B)	Mn(C) / Co	Z
Mn(C)	Mn(B) / Z	Co
Z	Mn(C) / Co	Mn(B)

 Table 5.2: Nearest and second nearest neighbor coordinations in Mn_2CoZ .

nearest and second nearest neighbors, while the intra-sublattice contributions are significant up to $r = a$. An exponential damping of the exchange interactions is expected for half-metals [90]; in the cases of Ga and In the damping is also present, but not as efficient as in the half-metallic case of Al. One observes clearly the dominating Co-Mn(B) and Mn(C)-Mn(B) nearest neighbor interactions, where the Mn(C)-Mn(B) interaction is clearly the stronger one. The Co-Mn(B) (second nearest neighbor interaction) is much weaker in comparison. In the graphs we omit the interactions with Z, because these are effectively zero for all distances. Co and Mn(C) couple antiferromagnetically to Mn(B), while Co and Mn(B) couple ferromagnetically. Hence, the antiparallel alignment of the Mn(C) moment is stable with respect to Mn(B) *and* Co. On the other hand, the intra-sublattice interactions are negative, which leads to a destabilization of the parallel alignment of the moments on one sublattice. It should be noted that in the Al-Ga-In series the Mn(C)-Mn(C) interaction is reduced on the first shell, while it is increased on the second shell at $r = 1$, where it becomes larger than the Co-Mn(C) inter-sublattice interaction.

For the Si-Ge-Sn series some differences to the previous results are notable. The most evident one is the much lower Mn(C)-Mn(C) interaction, but also the Co-Mn(B) interaction is significantly reduced. In particular, the Mn(C)-Mn(B) interaction is reduced by a factor of about 3, in very good agreement with the reduction of the Mn(B) moment. This indicates a strong direct exchange interaction, which is feasible because of the small Mn(B)-Mn(C) distance of typically 2.53 Å. It is remarkable that the Co-Mn(B) interactions are even slightly increased with respect to the Al-Ga-In series, although the site-resolved magnetic moments are systematically lower. The additional loosely bound *sp* electron augments the direct exchange coupling here. Finally, the intra-sublattice inter-

Mn ₂ CoZ	Al	Ga	In	Si	Ge	Sn	Sb
T_C^{MFA} (K)	890	886	845	578	579	536	567

Table 5.3: Curie temperatures T_C^{MFA} calculated in the mean-field approximation.

action of Mn(B)-Mn(B) is found to be positive in all three compounds on the first shell, but the other intra-sublattice parameters are still negative.

Mn₂CoSb is special in this respect, since it is a ferromagnet with a small positive magnetic moment on the Mn(C) site. Accordingly, the Co-Mn(C) and Mn(C)-Mn(B) interactions are positive, and their values are in reasonable agreement with the reduction of the Mn(C) moment. In contrast, the Co-Mn(B) interaction is still large and is with the exception of Mn₂CoSi the largest one among all discussed compounds. The Mn(B)-Mn(B) interaction is negative again on the first and second shells. Such a periodicity with respect to the valence electron count of the system has been predicted by Şaşıoğlu for some full Heusler compounds and occurs in the presence of indirect exchange interactions mediated by the conduction electrons [94].

From the exchange coupling parameters described above we calculated the Curie temperatures within the mean field approximation (see Table 5.3). The series Al–Ga–In has surprisingly high values of more than 800 K, even reaching almost 900 K for Mn₂CoAl. For the Si–Ge–Sn series we found moderate values between 500 and 600 K. The Curie temperature of Mn₂CoSb is similar as for the Si–Ge–Sn series. This is surprising at a first glance, because the Mn(C)-Mn(B) exchange interaction is so small here. It can be understood if we neglect all interactions but Mn(C)-Mn(B) and Co-Mn(B). In this case, $J_0^{\mu\nu}$ becomes a singular 3×3 matrix with two nonzero eigenvalues, which have the form of a root mean square of the Co-Mn(B) interaction and the Mn(C)-Mn(B) interaction. Obviously, if one interaction is significantly larger than the other (as, e.g., in Mn₂CoSn), then the eigenvalues will be dominated by the larger interaction. This and the increased Co-Mn(B) exchange interaction explain the unexpected behaviour.

However, what is most exciting about these results is the fact that Mn₂CoAl, Mn₂CoGa, and Mn₂CoIn have the possibly highest Curie temperature among all ferrimagnetic intermetallic compounds reported to date. The Curie temperature decreases from one Z group to another, although the total moment

increases. A behaviour like this is unique to the Mn_2 based inverse Heusler compounds. The Co_2 - and Mn_2 -based genuine Heusler compounds show a scaling of the Curie temperature roughly proportional to the total moment upon change of the Z element, see Ref. [96] and Chapter 4. Nevertheless, the Mn_2CoZ compounds can be related to the Co_2 -based Heusler compounds with the sum of the absolute values of the site resolved magnetic moments \tilde{m}_{total} : in, e.g., Mn_2CoAl we have $\tilde{m}_{total} = 5.27 \mu_B$, which is close to the value of ferromagnetic Co_2MnSi ($5 \mu_B$). The latter has a Curie temperature of 985 K [51], which is close to T_C^{MFA} of Mn_2CoAl . Further, the Curie temperature and \tilde{m}_{total} are decreased with increasing Z electron number in Mn_2CoZ .

Naturally, the question about the accuracy of our Curie temperature calculation arises here. For the Mn_2CoZ series only few data are available. Lakshmi *et al.* reported $T_C = 605$ K for disordered Mn_2CoSn [31]. Dai *et al.* reported 485 K for disordered Mn_2CoSb [32]. Hence, the T_C^{MFA} value underestimates the measured value in Mn_2CoSn and overestimates it for Mn_2CoSb , so no systematic trend can be stated here. It is *a priori* not clear which type of disorder can increase or decrease the Curie temperature, since the exchange interactions are highly site specific and quite complex. However, the calculated values reproduce the measured data within ± 100 K.

In Figure 5.2 we show the calculated Curie temperatures in dependence on the cluster radius taken into the summation in Equation (3.46). As expected from the J_{ij} plots in Figure 5.1, T_C^{MFA} is already determined by the nearest neighbor interactions in all compounds. Only weak changes are observed with increasing cluster radius and T_C^{MFA} is well converged at $r = 1.5a$. This plot helps us to identify the origin of the reduced Curie temperatures of Mn_2CoIn and Mn_2CoSn , which is apparently not the same. For Mn_2CoIn we can assign the jump at $r = a$ to the strong antiferromagnetic intra-sublattice interaction of Mn(C)-Mn(C). In Mn_2CoSn , the reduced ferromagnetic Mn(B)-Mn(B) intra-sublattice interaction on the third neighbor shell at $r = 0.707a$ is responsible for the reduction.

In order to shed some more light on the character of the exchange interactions and their dependence on the site specific magnetic moments, we calculated the ground states and exchange coupling parameters for Mn_2CoGe in the range of $a = 5.60 \dots 5.95$ Å. Thereby we can separate the influence of the Z valence electron count and the binding energy from geometric effects. The compound is a ferrimagnetic half-metal over the whole range, so we can expect minimal band structure effects on the calculations.

On the other hand, the site resolved magnetic moments change considerably

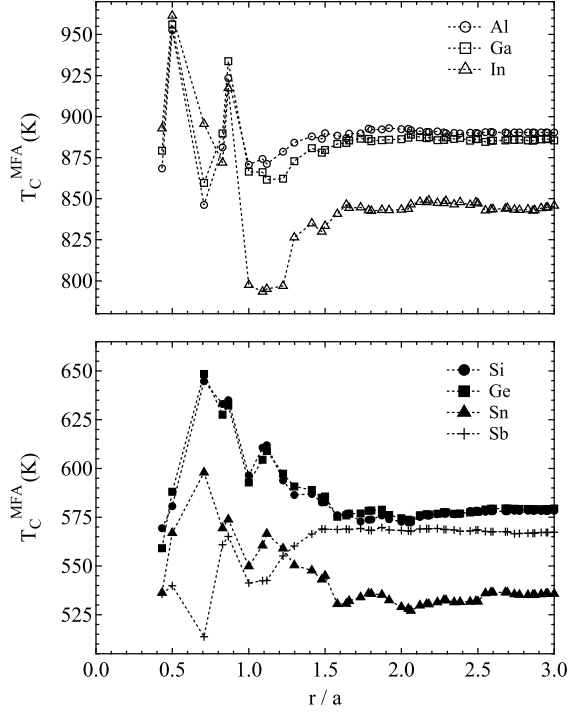


Figure 5.2: Curie temperatures T_C^{MFA} as a function of the cluster radius taken into account.

with the lattice parameter (Figure 5.3 (a)). Their absolute values increase with increasing lattice parameter as already explained above. All moments vary approximately linearly such that the total moment remains at $3 \mu_B / \text{f.u.}$ The moment of Mn(C) changes within the investigated range by more than a factor of three, from -0.34 to $-1.12 \mu_B$. The compensation comes mostly from the Mn(B) site, and the Co moment remains fairly constant.

To display the exchange interactions in a compact form, we show the relevant contributions to the $J_0^{\mu\nu}$ matrix (Equation (3.46)) in Figure 5.3 (b). The Co-Mn(B) interaction sum is nearly constant, although the magnetic moments increase. The nearest neighbor interaction remains nearly constant, but the weak longer-ranging interaction is significantly decreased and accounts for the decrease in the interaction sum. The constant nearest-neighbor interaction

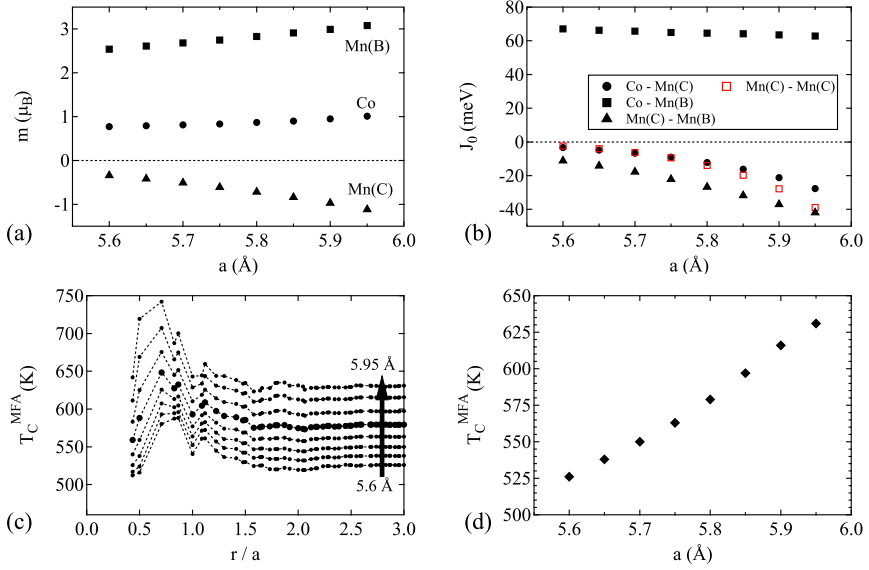


Figure 5.3: Lattice parameter dependencies in Mn_2CoGe . (a): Site resolved magnetic moments. (b): J_0^{HV} contributions. (c): Curie temperatures T_C^{MFA} in dependence on the cluster radius. (d): Curie temperatures T_C^{MFA} .

is a result of two opposing processes, namely the increase of the moments and the reduction of exchange efficiency due to longer interatomic distances. In contrast, the interactions involving Mn(C) change considerably with the interatomic distance. The Mn(C)-Mn(B) exchange interactions increase by a factor of four, in agreement with the product $m_{\text{Mn(B)}} \cdot m_{\text{Mn(C)}}$. Further, the Co-Mn(C) interaction increases more than linearly with the lattice parameter, but the interaction is presumably indirect and no simple dependence is obvious. All these interactions lead to an increase of the Curie temperature with the lattice parameter. In contrast, the antiferromagnetic Mn(C)-Mn(C) exchange interaction counteracts the ferrimagnetic order in the compound and reduces the Curie temperature. This influence is, however, negligible at small lattice parameter, but becomes quite large at the highest values, even compensating the Mn(C)-Mn(B) interaction. Notably, the Mn(C)-Mn(C) interaction is entirely governed by the nearest neighbor interaction and depends approximately on $m_{\text{Mn(C)}}^2$.

Figure 5.3 (c) displays the Curie temperature in dependence on the cluster radius. The general features of the exchange interactions are the same for all lattice parameters considered. However, there are some subtle differences on the second and third shells at $r = 0.5a$ and $r = 0.707a$, respectively. The change on the second shell can be traced back to the increased Co-Mn(C) interaction. Relative to the second shell, the contribution of the third shell is reduced. This arises from the increased antiferromagnetic Mn(C)-Mn(C) interaction discussed above. For clarity, Figure 5.3 (d) shows that the resulting Curie temperature T_C^{MFA} increases from 526 K to 631 K with increasing lattice parameter.

In terms of a pressure dependence, the Curie temperature of Mn_2CoGe is thus predicted to decrease upon hydrostatic pressure, i.e., $dT_C/dp < 0$. This situation is very different from that in Heusler compounds, where usually $dT_C/dp > 0$ is found. However, it is in agreement with Castelliz' [98] and Kanomata's [95] empirical interaction curves. They propose a negative pressure coefficient of T_C for short Mn-Mn distances as in hexagonal MnAs or MnSb, but a positive coefficient at larger distances as in the Heusler compounds $X_2\text{MnZ}$. *Ab initio* calculations by Yamada *et al.* on hexagonal MnAs [99] and by Şaşıoğlu *et al.* on the Heusler compound Ni_2MnSn [93] are in agreement with the experimentally observed pressure dependencies. As shown in Chapter 4, we have also calculated a positive pressure coefficient of T_C in the (hypothetical) Mn_2TiZ Heusler compounds. The Mn-Mn distance in the Mn_2CoZ compounds is even smaller than in the hexagonal MnAs or MnSb compounds, so a strong negative pressure dependence of T_C is in good agreement with the available experimental data.

Since the lattice parameter dependence of the Curie temperature is positive, the reduction of T_C^{MFA} in Mn_2CoIn and Mn_2CoSn (which have the largest lattice parameters within their groups) can be ascribed to a binding energy effect due to the high-lying valence states in In and Sn.

6 Electronic structure of fully epitaxial Co_2TiSn thin films

6.1 Introduction

Co_2TiSn has been the subject of many experimental and theoretical studies. The ground state properties obtained by density functional theory (DFT) depend sensitively on the choice of the DFT method [23, 38, 39, 100, 101, 102, 103, 104]. The potential has strong non-spherical components and thus only a full-potential treatment in connection with the generalized gradient approximation (GGA) to the density functional yields a half-metallic ground state [38, 101].

Experiments conducted on bulk CTS find a lattice parameter of 6.07 Å, a magnetic moment of about $1.95 \mu_B/\text{f.u.}$ and a Curie temperature (T_C) around 355 K [38, 88, 105]. Further, it is found to have a strongly anomalous temperature dependence of resistivity, the temperature coefficient becomes negative above the Curie temperature. A large negative magnetoresistance reveals the importance of spin fluctuations in the compound [78].

A rather new development aims at the thermoelectric properties of Co_2TiSn , which has a large and constant Seebeck coefficient of $-50 \mu\text{V}/\text{K}$ above T_C in the bulk [88]. There have been some efforts to understand the unusual transport properties of CTS by *ab initio* band structure and semi-classical transport theory [88, 106]. These properties make CTS interesting for a possible application in spin caloritronics, which attempt to make use of the interactions between heat and spin. An implementation into thin films is of particular importance for such applications.

Only two studies on thin films of CTS are available as far as we know. Gupta *et al.* applied pulsed laser ablation to grow CTS on Si (001) substrates from a stoichiometric target at growth temperatures up to 200°C [107]. The authors found off-stoichiometric, polycrystalline films with (011) texture. Suharyadi *et al.* utilized an atomically controlled alternate deposition technique based on electron beam evaporation [108]. They have grown (001) oriented, $L2_1$ ordered films on Cr buffered MgO (001) substrates at growth temperatures up to 600°C

and investigated them by nuclear resonant scattering.

In this chapter we present a successful preparation technique based on DC magnetron co-sputtering. We present data on the structural and magnetic properties of our films. Further, we characterize the electronic transport properties which make CTS a particularly interesting compound. Finally we discuss the electronic structure of our CTS films based on soft x-ray absorption spectroscopy and *ab initio* electronic structure calculations.

6.1.1 Experimental details

The samples were deposited using the BESTEC UHV sputtering system, see Chapter 2.1. With the quartz sensor and x-ray reflectometry (XRR), the film stoichiometry of a compound can be set up with a relative accuracy of about $\pm 10\%$. Inductively coupled plasma optical emission spectroscopy (ICP-OES) was used to fine-tune the sputter parameters. For the samples deposited at high temperature we checked the stoichiometry by energy dispersive x-ray analysis (EDX) in an electron microscope and found no deviation from the stoichiometry of room temperature deposited films of same thickness. The sputtering power ratios were 1 : 1.67 : 0.34 (Co:Ti:Sn). The voltages were constantly monitored during the deposition, which remained constant throughout all deposition processes, ensuring the reproducibility of the method. Cross-talk effects on the Sn target constituted a serious problem for the deposition process due to the low sputtering power applied to the source. This was suppressed by a chimney-like cylinder put around the source, such that there was no line-of-sight from this target to another. The compound was deposited at a rate of 1.5 \AA/s . Sample rotation was set to 28 rpm, making sure that with each turn only one primitive cell was deposited. All elemental targets had 4N purity. The sputtering pressure was set to $2 \cdot 10^{-3}$ mbar. With this technique we have fabricated thin film samples with a precisely set up stoichiometry of $\text{Co}_{2.0}\text{Ti}_{1.0}\text{Sn}_{1.0}$, with errors of $< 3\%$ for the individual constituents.

All samples used in this study had the following stack sequence: MgO (001) / MgO 5 nm / CTS 18 nm / MgO 2 nm. The lower MgO was deposited by RF sputtering at $2.3 \cdot 10^{-2}$ mbar to ensure good crystallinity of the buffer. The upper MgO was deposited by e-beam evaporation from single crystal MgO slabs after cooling the samples to less than 100°C . The base pressure during deposition with the heated substrate was always below $5 \cdot 10^{-8}$ mbar.

Resistivity was measured in standard in-line four-probe DC geometry in a closed-cycle He cryostat and a vacuum furnace. The resistivity ρ is calculated

from the film thickness d , the voltage U and the current I as $\rho = d \cdot (\pi / \ln 2) \cdot (U/I)$. Magnetoresistance was measured with a variable permanent magnet (coaxial Halbach cylinder configuration, Magnetic Solutions Multimag) with a maximum field strength of 10 kOe in the cryostat. The data were taken by driving full magnetization loops and then averaging the points for each field magnitude.

The Seebeck coefficient was determined in a home built setup in air. The sample was contacted with platinum tips. It was measured at an average temperature of $\bar{T} = 310$ K with a temperature gradient of $\Delta T = 10$ K.

Magnetic measurements were taken using a superconducting quantum interference device (SQUID) at temperatures in the range of 5 K to 400 K in magnetic fields of up to 50 kOe.

X-ray diffraction (XRD) and reflectometry (XRR) have been performed in the Philips X'Pert Pro MPD in Bragg-Brentano configuration. Texture characterization was additionally performed with collimator point focus optics on the open Eulerian cradle.

Temperature dependent x-ray absorption spectroscopy (XAS), x-ray magnetic circular dichroism (XMCD) and x-ray magnetic linear dichroism (XMLD) was performed at BL 6.3.1 and BL 4.0.2 of the Advanced Light Source in Berkeley, USA. The element-specific magnetic properties were investigated at the Co- and Ti- $L_{3,2}$ edges in surface-sensitive total electron yield mode (TEY)[56] for temperatures between 20K and 370K.

For XMCD, the sample was saturated by applying a magnetic field of max. ± 20 kOe along the x-ray beam direction using elliptically polarized radiation with a polarization of $P_{hv} = \pm 60\%$ (BL 6.3.1) and $P_{hv} = \pm 90\%$ (BL 4.0.2), respectively. The x-rays angle of incidence with respect to the sample surface was $\alpha = 30^\circ$ (BL 6.3.1) and $\alpha = 90^\circ$ (BL 4.0.2), respectively. I^+ and I^- denote the absorption spectra (normalized to the x-ray flux measured by the total electron yield of a Au grid in front of the sample) for parallel and anti-parallel orientation of the photon spin and the magnetization of the sample. The XAS and XMCD spectra are defined as $\text{XAS}^c = (I^+ + I^-)/2$ and $\text{XMCD} = (I^+ - I^-)$, respectively. To calculate the element-specific spin and orbital magnetic moments from the data we applied sum-rule analysis, see Chapter 2.4.2.

Anisotropic XMLD spectra were taken at BL 4.0.2 with 100% linearly polarized light in normal incidence using the eight-pole electromagnet end station [109]. The magnetic field for switching the magnetization of the sample was applied parallel and orthogonal to the polarization vector of the incoming light,

the according absorption spectra normalized to the x-ray flux are denoted as I^{\parallel} and I^{\perp} . The XAS and XMLD spectra are then defined as $XAS^l = (I^{\parallel} + I^{\perp})/2$ and $XMLD = (I^{\parallel} - I^{\perp})$, respectively. Spectra were taken with magnetic fields aligned along the [100] and the [110] directions of the Co_2TiSn films. The applied magnetic field of 4.5 kOe was canted out of the surface plane by 10° to improve the electron yield signal. However, the XMLD results are nearly unaffected by this because the demagnetizing field perpendicular to the film plane is so strong that the magnetization is tilted out-of-plane by less than 5° (measured by analyzing the XMCD asymmetry for different tilting angles).

The XMCD and XMLD spectra were taken by switching the magnetic field at each energy point. To remove non-dichroic artifacts we performed measurements for positive and negative polarization (XMCD) or different spatial orientations of the polarization vector (XMLD) and averaged the corresponding spectra.

6.1.2 Theoretical approach

The electronic structure probed by x-ray absorption spectroscopy has been investigated in direct comparison with *ab initio* electronic structure calculations. We used two different approaches to this end. First, electronic structure calculations were performed with the *Munich* SPRKKR package, see Chapter 3.2.2. And second, in order to take care of the excited state band structure, which is actually probed in XAS, spectrum simulations were carried out in FEFF9, see Chapter 3.4.4.

In SPRKKR, the band structure and the ground state properties were calculated in the fully-relativistic representation of the valence states, thus including spin-orbit coupling. The angular momentum cutoff was set to $l_{\max} = 3$ (*spdf*-basis) and the full potential was taken into account. The bulk lattice parameter of $a = 6.07 \text{ \AA}$ was used. The exchange-correlation potential was modeled with

$m_{\text{spin}}^{\text{Co}}$	$m_{\text{orb}}^{\text{Co}}$	N_h^{Co}	$m_{\text{spin}}^{\text{Ti}}$	$m_{\text{orb}}^{\text{Ti}}$	N_h^{Ti}
0.96	0.04	2.06	-0.03	0.01	7.65

Table 6.1: Results of band structure calculations with SPRKKR. The magnetic moments are given in μ_B / atom.

the generalized gradient approximation (GGA) in the Perdew-Burke-Ernzerhof parametrization.

The resulting atomic magnetic moments were then used as input parameters to FEFF9, which is not spin self-consistent. The self-consistent potential was obtained on a cluster of 59 atoms and the x-ray absorption near edge spectroscopy (XANES) was calculated on a cluster of 229 atoms. The complex Hedin-Lundqvist self-energy was applied and the calculations were done with the final state rule, including a full screened core hole on the absorber. The angular momentum for the full multiple scattering was taken to $l_{\max} = 3$.

The ground state described by the SPRKKR calculation is not half-metallic with the experimental lattice parameter, in contrast to calculations with full potential linearized augmented plane-waves codes [38, 104]. The Fermi energy is slightly above the minority spin gap; a small increase of the lattice parameter would move E_F into the gap. This is due to the angular momentum truncation at $l_{\max} = 3$, which is insufficient to capture the non-spherical components of the density. For technical reasons, it can not be taken to higher values. However, this does not significantly change the shape of the calculated XAS spectrum. The total spin moment is $1.9 \mu_B / \text{f.u.}$ and the total orbital moment is $0.09 \mu_B / \text{f.u.}$. The atom-resolved magnetic moments and the numbers of holes for Co and Ti are given in Tab. 6.1. The negative Ti spin moment indicates a weakly ferrimagnetic behavior of CTS.

6.2 Experimental results

6.2.1 Structure

XRD and XRR were utilized to investigate the structure of the films. Figure 6.1 displays a set of data that were extracted from the measurements. As is clearly visible in Figure 6.1 (a), the films show Laue oscillations on the (002) reflection that become more pronounced with increasing deposition temperature. Laue oscillations are only observed if the crystalline coherence is very good and the roughness is small. While the two films deposited at lower temperatures show only weak oscillations, the two films deposited at higher temperature exhibit pronounced fringes. Only weak asymmetry of the fringes is observed for $T_S = 700^\circ\text{C}$, indicating nearly homogeneous (or no) strain along the growth direction.

Four intense (111) reflections have been observed in pole figure analysis at

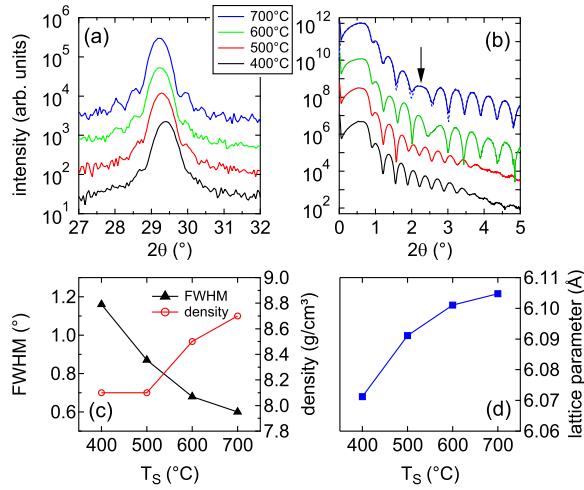


Figure 6.1: (a): X-ray diffraction scans of the (002) reflections showing Laue oscillations. (b) X-ray reflectometry (XRR) scans. The dashed line represents the best fit to the experimental curve with $T_s = 700^\circ\text{C}$. (c): Full-widths at half-maximum (FWHM) of the rocking curves and effective density determined by XRR. (d): Out-of-plane lattice parameter c .

the expected tilt angle of $\Psi = 54.74^\circ$ for all samples. The intensity increases considerably with increasing deposition temperature. The epitaxial relationship is $\text{Co}_2\text{TiSn [100]} \parallel \text{MgO [110]}$, which is commonly observed for Heusler compounds on MgO (001) substrates.

The out-of-plane lattice parameter c measured on the (004) reflection, displayed in Figure 6.1 (d), is found to increase with increasing deposition temperature and converges for the highest deposition temperatures. For 700°C , we find a lattice parameter of $c = 6.105 \text{ \AA}$.

The full-width at half-maximum (FWHM) of the rocking curves measured on the (004) reflections are displayed together with the density determined by XRR in Figure 6.1 (c). For high deposition temperature the rocking curve FWHM is found to be as low as 0.6° , which demonstrates the narrow orientation distribution of the individual film grains.

XRR provides indirect information on the film morphology. The density determined by XRR has to be seen as an effective density, which only reflects

the real film density if the surface roughness is low with a Gaussian distribution on a small lateral scale. In Fig. 6.1 (b) we present the XRR curves of our samples. The roughness is high for the two samples with lower growth temperature, which is identified by a quick vanishing of the Kiessing fringes. The MgO cover layer does not show up as an individual resonance. We find an increase in the XRR density for deposition with 600°C and more, while the roughness is greatly reduced and the MgO cover layer becomes visible (see arrow). The XRR roughness of the film with $T_S = 700^\circ\text{C}$ is 0.3 nm. The scans for the two lower deposition temperatures can not be fit with the Parratt algorithm [54]. They show two main Fourier components at 18 nm and 23 nm, and a difference component at 5 nm. A columnar growth with high and low grains that have 18 ± 5 nm thickness can be inferred from this. At higher temperatures, the growth changes to a mode with large and smooth grains of equal height. This behavior has been confirmed by atomic force microscopy.

From Thornton's model[110] of film growth for sputtered films it is expected to find a transition from a fine-grained columnar structure to a regime with large grains governed by bulk diffusion and recrystallization at about half the melting temperature, $T_S/T_m \approx 0.5$. In fact, the melting point of Co_2TiSn is 1720(20) K,[111] i.e., this transition is expected around 600°C .

With the experimental bulk lattice parameter $a = 6.07\text{\AA}$, the density of the compound is calculated to be 8.446 g/cm^3 . If one assumes a perfect, strained epitaxial growth on the MgO substrate, the lattice will be distorted tetragonally, with an in-plane lattice parameter $a = \sqrt{2} \cdot 4.21\text{\AA} = 5.95\text{\AA}$ and accordingly expanded out-of-plane. If the volume remained constant, the out-of-plane lattice parameter would be 6.32\AA . For the film deposited at 700°C , we measured $c = 6.105\text{\AA}$. Recalculating the density for this tetragonal configuration gives $\rho = 8.74\text{ g/cm}^3$, which is in close agreement with the measured density of $\rho = 8.7\text{ g/cm}^3$. This result supports the growth model discussed above. Further, we have shown in a recent paper by *ab initio* theory that a tetragonal distortion of Co_2TiSn can easily occur because of the low energy associated with the distortion [104]. It is of the order of 50 meV / f.u. , and is thus easily activated during the growth. However, at lower temperatures this constitutes a metastable state.

6.2.2 Magnetism

SQUID measurements taken on the sample with $T_S = 700^\circ\text{C}$ give a magnetic moment of $m = 1.6(1) \mu_B / \text{f.u.}$ and a Curie temperature of $T_C = 375(5) \text{ K}$ (Fig. 6.2). The Curie temperature is higher than in bulk samples, where it has been reported to be about 355 K. The coercive field is 160 Oe at 20 K and 150 Oe at room temperature. Since the magnetization declines sharply at T_C , we can conclude that the films consist of a single magnetic phase.

6.2.3 Electronic transport

Resistivity and magnetoresistance have been measured on a sample deposited at $T_D = 700^\circ\text{C}$; the data are shown in Fig. 6.3. The resistivity shows clearly the cusp-type resistivity anomaly that is also observed for bulk samples of Co_2TiSn at T_C . Details of the transition can be found by analyzing the first and second derivatives of the resistivity curve. We define the onset of the as the first inflection point of the resistivity; it is found at 350(5) K. The maximum of the resistivity is at 395(5) K, i.e., 20 K above T_C . The offset of the transition, given by the second inflection point, is at 440(5) K. At $T_C = 375(5) \text{ K}$ we find the maximal change rate of the resistivity's slope, identified by a clear minimum of the second derivative.

By plotting the logarithm of the resistivity against $1/T$ for the data points above the second inflection point, we find the effective gap width of the param-

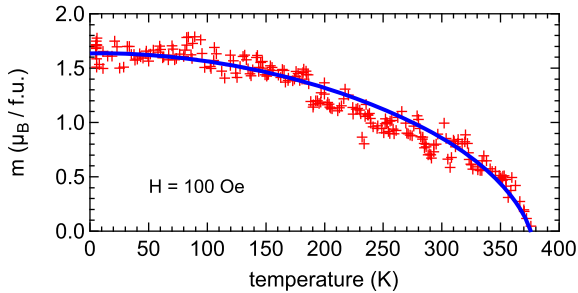


Figure 6.2: Magnetization in dependence of the sample temperature (markers). It was taken as a temperature sweep with a constant field of 100 Oe. The solid line is a guide to the eye.

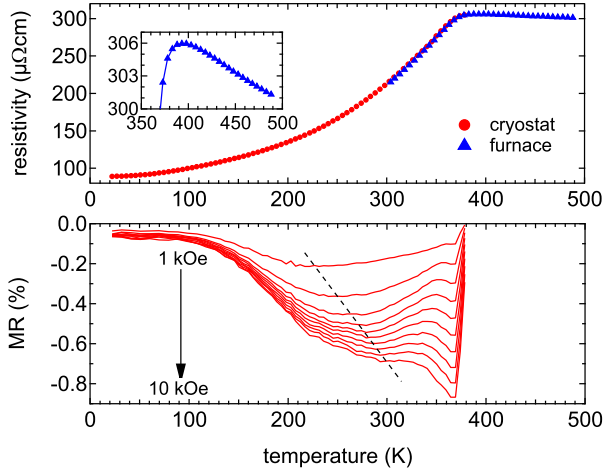


Figure 6.3: Top: Resistivity of a Co_2TiSn film deposited at $T_S = 700^\circ\text{C}$ on a MgO single crystal. The inset shows the region around the ferrimagnet-paramagnet transition. Bottom: Corresponding magnetoresistance for fields of 1 kOe to 10 kOe with the magnetic field \vec{H} in the sample plane and the current $\vec{j} \perp \vec{H}$.

agnetic state to be $E_g = 6.5 \pm 0.5$ meV. This is considerably smaller than the gap width of 12.7 ± 1 meV reported for bulk samples. However, it has been argued by Barth *et al.* that an actual transition to a semiconductor is improbable. They found significant differences for the calculated conductivity tensors between spin-polarized and unpolarized calculations. By mixing the states weighted by a molecular field approximation for the magnetization, they could partly explain the anomalous behavior of the resistivity [88].

Compared with bulk samples, we also find a notably lower residual resistivity $\rho(20\text{K}) = 89 \mu\Omega\text{cm}$ and a total resistivity amplitude $(\rho_{\text{max}} - \rho_{\text{min}}) = 216 \mu\Omega\text{cm}$, compared to 310 and $205 \mu\Omega\text{cm}$ [78], or 245 and $135 \mu\Omega\text{cm}$ [88], respectively. The residual resistivity of a metal is mainly given by its defect density, i.e., dislocations, disorder, impurities and grain boundaries. In a thin film, one has to take the interfacial scattering into account. Our thin films have very low residual resistivity compared to bulk samples, which might indicate that their crystalline properties are superior to those of bulk samples. We attribute this to large, flat grains and good chemical order.

The temperature dependence of the resistivity is well described by a T^2 term up to 180 K, which is mainly attributed to electron-electron scattering. Above 180 K up to the first inflection point the curve is better fit by a T^3 law. In bulk samples, the parabolic shape of the resistivity curve at intermediate temperatures is less pronounced than in our films. However, the overall shape is in agreement with the curves found by other authors.

The magnetoresistance (MR) of the film, defined by $\text{MR}(H, T) = (\rho(H, T) - \rho(0, T)) / \rho(0, T)$, shows strongly nonlinear behavior. At low temperature only weak MR is found. With increasing temperature an increasing MR is observed, which is negative over the whole temperature range, i.e., the resistivity is lower if a magnetic field is applied. It has a pronounced, nonlinear dependence on the applied magnetic field. With an available magnetic field of 10 kOe the MR was by far not saturated. A distinct extremum is observed at large fields right below T_C , being the global minimum of the curve at fields larger than 7 kOe. Above T_C the MR vanishes. The appearance of the extremum and its amplitude are in agreement with the data published by Majumdar *et al.* [78]. The MR can be explained in terms of spin fluctuations and associated spin-flip scattering: at low temperature, the fluctuations are nearly zero and a small magnetic field is sufficient to saturate the film. With increasing temperature, fluctuations become more important, but can be suppressed by enforcing a particular spin orientation in a strong field. This picture is supported by the shift of the first minimum with increasing magnetic field, denoted by the dashed line in Fig. 6.3. The MR is enhanced at T_C because the spin fluctuations are strongest at the transition temperature and the ferrimagnetic state is stabilized in a large field. Furthermore, the MR has no traceable anisotropic MR (AMR) contribution: the typical inversion of the MR at zero field for $\vec{j} \perp \vec{H}$ compared to $\vec{j} \parallel \vec{H}$ is missing.

The Seebeck effect has been measured on the same sample as the resistivity. It was $S = -14 \pm 2 \mu\text{V} / \text{K}$ at 310 K, which is about 2.6 times lower than in the bulk ($-37 \pm 2 \mu\text{V} / \text{K}$) [88]. This is in agreement with the much lower resistivity of our films compared to bulk samples. Barth *et al.* point out that the Seebeck coefficient can be enhanced by scattering on grain boundaries or impurities, [88] which appear to be rarer in the films. On the other hand, the Seebeck coefficient is proportional to ν / σ , with the electrical conductivity σ and the thermal conductivity ν . Thus, the lower S may also indicate a lower heat conductivity of the film.

6.2.4 Interfacial chemistry

XMCD and XAS^c measurements were performed at BL 6.3.1 at 20K and at RT for films deposited on MgO single crystalline substrates ($T_S=400^\circ\text{C}$, 500°C , 600°C , 700°C , and post-annealed samples).

The Co XMCD signals for different deposition temperatures show two notable trends: the Co magnetic moment, measured at 20 K, and the ratio of the Co XMCD signals measured at RT and at 20K increase with increasing T_S . This implies that the chemical order improves with increasing substrate temperature, resulting in higher saturation magnetization and higher Curie temperature. That is in agreement with SQUID measurements on the same samples.

At $T_S = 400, 500^\circ\text{C}$ we found multiplet structures on the Ti $L_{3,2}$ edges, which indicate formation of interfacial TiO_2 [112]. These structures almost vanish at $T_S = 600^\circ\text{C}$ and are not traceable at $T_S = 700^\circ\text{C}$ anymore. The spectral shapes of the XMCD signals on Co and Ti do not change on the other hand, only the amplitude is reduced at lower deposition temperature. The large roughness of the films deposited at the lower temperatures leads to an incomplete covering with the protective MgO layer. The CTS compound is thus oxidized in air, which is particularly observed as surfacial TiO_2 , which is not magnetic.

In vacuum post-annealed samples have been additionally investigated for their interfacial chemistry. Annealing at temperatures above 350°C resulted in formation of interfacial TiO_2 . Naturally, this will also happen at the lower interface to the MgO substrate. Because of the high growth temperatures, we can expect an oxide thickness of several nanometers. This effect may account for the low average magnetization measured in the SQUID. An oxidized bottom layer of 3 nm thickness can account for the deviation from the nearly $2 \mu_B / \text{f.u.}$ measured in the bulk and predicted theoretically.

Using the results from this systematic analysis we chose two samples for in-detail investigations described in the next section.

6.2.5 Element specific magnetization

Highly resolved XMCD and XMLD spectra were taken at BL 4.0.2 at 20K for the samples deposited at 400°C and 700°C , respectively (see Fig. 6.4 and 6.5). Whereas the XAS^c spectra show significant differences for the two deposition temperatures for Co and Ti, the shape of the XMCD spectra does not depend on the deposition conditions. For Co the deposition at higher temperature results

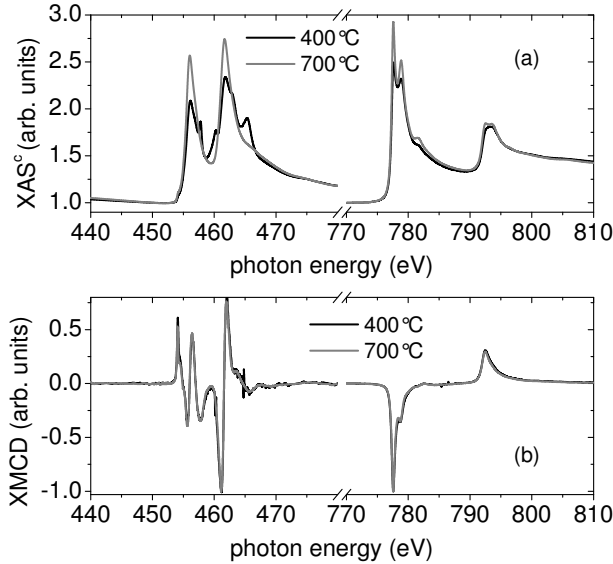


Figure 6.4: Normalized XAS^c and XMCD spectra of Ti and Co measured at 20K for samples deposited on MgO single crystals at 400°C and 700°C, respectively.

in a more pronounced fine structure, consisting of a double peak at the L_3 resonance and a shoulder about 4 eV above the resonance. These structures are also reflected in the L_2 resonance, but less pronounced. Klaer *et al.* investigated Co_2TiSn bulk samples (*in situ* fractured in UHV for XMCD investigation) [113]. They also observed a double peak structure at the L_3 resonance, but less pronounced compared to our sample deposited at 700°C. Moreover, the double peak structure at the L_2 edge was not found in these bulk samples. Yamasaki *et al.* [114] have also investigated bulk samples (*in situ* scraped in vacuum for XMCD investigation), but in contrast to the results by Klaer *et al.* and us they observed three separated peaks at the L_3 edge and only one broad peak at the L_2 resonance. Obviously, their samples had a different electronic structure.

Our Co XMCD spectra also show the double peak structure at the L_3 edge, while at the L_2 edge only a shoulder is visible. Again, the structures in our XMCD spectra are sharper than those given by Klaer *et al.* and Yamasaki *et al.*. Our Ti XMCD spectra shown in Fig. 6.4b are similar to the data by Klaer *et al.*; Yamasaki *et al.* do not provide data on the Ti L-edges. However, the shape is

very different compared to data collected by Scherz *et al.* [115] on the system Fe/Ti/Fe(110). Therefore the relative alignment of the Co and Ti magnetic moments is not obvious from a comparison with their reference data.

In order to get further insight into the element specific magnetic properties, we applied the XMCD sum rules (Chapter 2.4.2). The results of the sum-rule analysis for the Co XMCD spectra are summarized in Tab. 6.2.

The Co spin moment is close to $1\mu_B$ for a deposition temperature of 700°C . For the deposition at 400°C the Co spin moment is a factor of two smaller, but the orbital to spin moment ratio is nearly identical for both deposition temperatures; the orbital moment is parallel to the spin moment. Both the spin and orbital moments are in very good agreement with the theoretical results. The number of d -holes is lower than for pure Co metal (1.75 and 1.5 for Co_2TiSn deposited at 700°C and 400°C , respectively, and 2.4 for pure Co[61]), which indicates a rather large charge transfer to the Co d states in Co_2TiSn . It is actually even a bit lower than the theoretical value of 2.06.

While the sum rules work well for Co, core-hole - photoelectron interaction and dynamical screening effects of the x-ray field prohibit their direct application to the early 3d transition metals [84]. The interaction leads to an intermixing of the L_3 and L_2 resonances, which is the reason for the deviation from the statistical branching ratio of 2:1 for the two edges. The intermixing, also known as jj-mixing of the $2p_{1/2}$ and $2p_{3/2}$ levels, leads to wrong results when the sum rules are applied to the early 3d transition metals. It has been suggested by Scherz that one can estimate the Ti spin moment by multiplying the result from the sum rule analysis by a factor of 4 [61]. This result has been obtained on the Fe/Ti/Fe(110) trilayer system. On the other hand, it must be expected that this correction factor itself depends on the actual electronic structure and thus the screening strength. The direct result from the sum rule

Table 6.2: Results of the sum rule analysis of the Co XMCD spectra measured at 20K for the samples deposited at 400°C and 700°C , respectively.

T_S	m_{spin}	m_{orb}	m_{orb}/m_{spin}	N_h
400°C	$0.48\mu_B$	$0.025\mu_B$	5.2%	1.50
700°C	$0.98\mu_B$	$0.055\mu_B$	5.6%	1.75

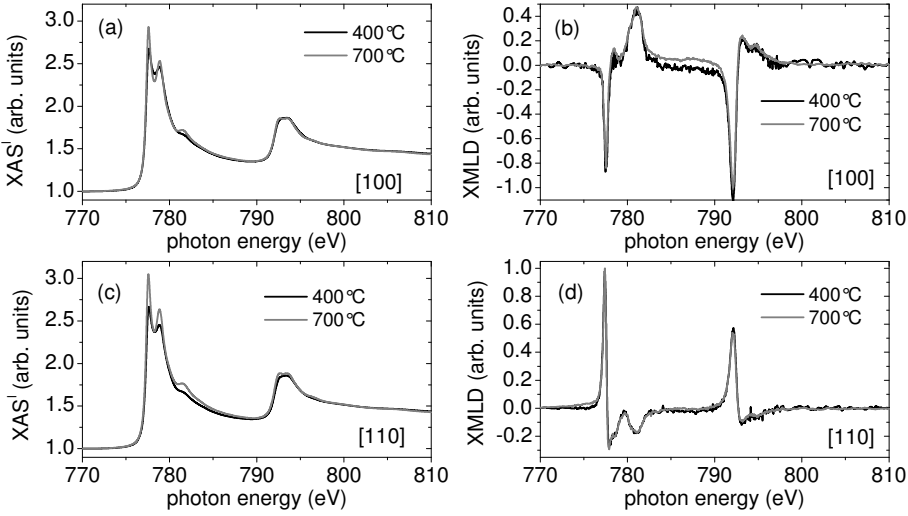


Figure 6.5: Normalized XAS^I and XMLD spectra of Co measured at 20K in the [100] (a and b) and [110] (c and d) directions for samples deposited on MgO single crystals at 400°C and 700°C, respectively.

analysis is $m_{spin} = -0.038 \mu_B$ for the sample deposited at 700°C, which is in good agreement with the theoretical result. In particular, an anti-parallel alignment with the Co spin moment is found. It is worth to mention, that the Ti orbital moment (the apparent value is $m_{orb} = 0.022 \mu_B$) is aligned anti-parallel to the Ti spin moment. The latter is in accordance with Hund's rules, which expect an anti-parallel alignment of the spin and orbital moment, because the Ti 3d shell is less than half filled. Because of the formation of interfacial TiO₂ the XMCD data can not be quantified for $T_S = 400^\circ\text{C}$. However, all qualitative conclusions with respect to the alignment of the Co and Ti orbital and spin moments are preserved for lower deposition temperatures, because the shapes of the Co and Ti XMCD spectra do not depend on T_S . In summary, the XMCD results are in very good agreement with theoretical expectations.

In general it is expected, that the XMLD signal is proportional to the square of the total magnetic moment of the individual atoms ($\text{XMLD} = \beta_l \cdot \langle m_{\text{total}} \rangle^2$), whereas the XMCD signal should be directly proportional to the magnetic moment ($\text{XMCD} = \beta_c \cdot \langle m_{\text{total}} \rangle$) [62]. Comparing the XMCD and XMLD signals (normalized to the post-edge jump height η , because the number of 3d-holes

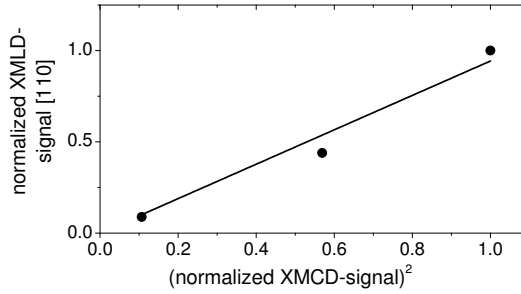


Figure 6.6: Normalized Co XMLD signal for the [110] direction as a function of the square of the normalized XMCD signal. The data points correspond to measurements taken at 20K, 300K and 370K. The sample was deposited on MgO single crystals at 700°C.

N_i is different for the samples deposited at 400°C and 700°C, respectively) for Co, it is interesting to note that $\text{XMLD}/\text{XMCD}^2$ is about 65% larger for the sample deposited at 400°C than for the 700°C sample. In the simple picture that the proportionality factors β_c and β_l are the same for both deposition temperatures, this means that in the disordered 400°C sample some of the Co atoms are anti-ferromagnetically coupled to the other Co atoms. On the other hand it is known, that the XMLD effect can become quite large in systems with localized electrons. The magnitude of the XMLD is given essentially by the magnetic moment and the $2p$ level exchange splitting, which itself is proportional to the magnetic moment. Actually, without the exchange splitting of the $2p$ levels, the XMLD would vanish. Localized $3d$ electron states increase the $2p$ - $3d$ exchange interaction, giving rise to an enhanced XMLD [63]. Therefore, the decrease of $\text{XMLD}/\text{XMCD}^2$ with the deposition temperature could also hint to a higher degree of localization of the Co moments for the 400°C sample. This is in agreement with an oxidized surface, in which the electrons should be more localized. However, the fine structure at the Co- L edges becomes more pronounced for higher deposition temperature (see Fig. 6.4a, 6.5a and 6.5c) which might indicate a higher degree of localization for higher deposition temperatures. The electron localization would give the Co a more atomic character, and atomic multiplets would become important, giving rise to a fine structure on the x-ray absorption spectrum. On the other hand, this would contradict the XMLD result. The maximum amplitude of the XMLD

for $T_S = 700^\circ\text{C}$ is 5.7% at the Co L_3 edge in the [110] direction. Thus, the Co $3d$ states take an intermediate position between the elemental ferromagnets Co and Fe, that have around 2%, and strongly localized systems like Mn in (Ga, Mn)As, which has about 12% [63]. Obviously, this discrepancy needs to be investigated by direct *ab initio* calculations of the absorption spectra, which will be discussed in Sec. 6.3.

For the sample deposited at 700°C the XMCD and XMLD effect was studied also at elevated temperatures. The normalized XMCD signals of Co and Ti have the same shape at 20 K, 300 K and 370 K. Furthermore, the Ti XMCD asymmetry changes by the same factor as the Co asymmetry between 20K and 370K. Therefore the ratio between the Ti and Co magnetic moments is not significantly changed at elevated temperatures. The temperature dependence of the XMLD signal was measured for the [110] direction. As shown in Fig. 6.6, the XMLD signal scales well with XMCD^2 , which was also found for other materials like (Ga,Mn)As [63] in accordance with the above mentioned expectation.

6.3 Electronic structure

As discussed above, the fine structure observed at the Co $L_{3,2}$ edges can have its origin in atomic multiplet effects related to electron localization or simply in the particular (itinerant) electronic structure of Co_2TiSn . The experimental XAS and XMCD spectra are compared to calculations with SPRKKR and FEFF9 in Fig. 6.7.

The SPRKKR spectra show broad edges and some weak shoulders on the high energy side of the white lines. Further, the ratio of the L_3 and L_2 XMCD signals is incorrect, the L_3 XMCD is too small.

Bekenov *et al.* have calculated the XAS/XMCD spectra of CTS *ab initio* using the spin polarized relativistic linear-muffin-tin-orbital (SPR LMTO) method.[116] Their simulations do not reproduce the double-peak structures and are rather similar to our SPRKKR spectra.

In FEFF9, the SPRKKR spectrum can be principally reproduced when the ground state density is used. Instead, if the density in the presence of a screened core hole is calculated, we find a structure that is very similar to the experimental spectrum. Because the self-consistency algorithm of FEFF9 is only accurate within 1 eV in its determination of the Fermi energy, one can use a small energy shift for fitting, thereby moving E_F within the density of

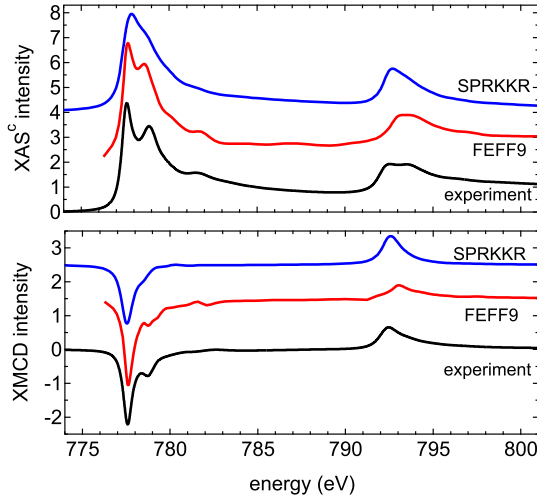


Figure 6.7: Comparison of the calculated Co $L_{3,2}$ XAS and XMCD spectra carried out in FEFF9 and SPRKKR to experimental spectra. The XMCD signals have been scaled to 90% to account for the experimental polarization degree. The experimental and the FEFF9 spectra are scaled to 1 in the post-edge region. The SPRKKR spectra are scaled to match the experimental L_3 resonance. The theoretical spectra are aligned in energy with the experimental spectrum.

states (DOS). With a shift of -0.2 eV we obtained the spectrum shown in Fig. 6.7. Obviously, both the double-peak structure of the white line as well as the small shoulder 4 eV above the white line are reproduced. Also the double-peak structure of the XMCD signal is well reproduced. Notably, not only the shape of the spectrum is basically correct, but also the intensities match the experimental data very well. However, the double-peak splitting of the L_3 line is calculated as 1.3 eV, compared to a measured splitting of 1.5 eV.

Since FEFF9 is based on the local density approximation within the density functional theory—and thus relies on single-particle theory—it does not account for atomic multiplet effects, which naturally are many-body effects arising from wave-function coupling. Consequently, we conclude that the features observed in our experimental spectra do not arise from multiplet effects and electron localization. Instead, they are features arising from the excited state band structure due to the presence of a core-hole. This is consistent with

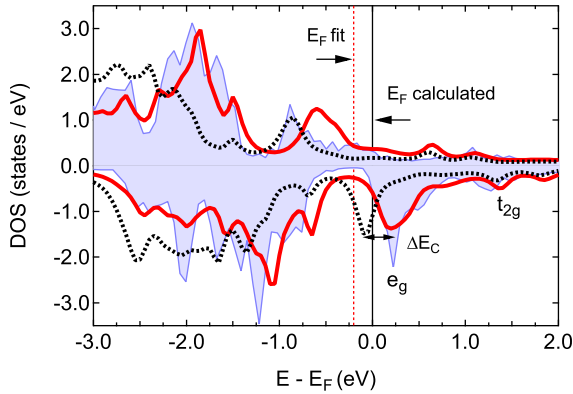


Figure 6.8: Comparison of the calculated Co site projected d DOS from SPRKKR (shaded blue area) and FEFF9 in the ground state (solid red line) and with an L_3 core hole (dotted black line).

the XMLD measurements discussed above, which indicate rather itinerant moments.

Our conclusion is further supported by the analysis given by Klaer *et al.*, who found that the observed structures can not be explained by charge-transfer multiplet theory [113]. They state that the splitting arises from a nearly pure Co e_g state above E_F giving rise to the first peak, and from a Co-Ti hybrid state of t_{2g} character, which results in the second peak. Since the t_{2g} states have more itinerant character, the core hole is more screened by the surrounding atoms, while the e_g states are significantly lowered in energy. This core-hole correlation energy ΔE_C was assumed to be 0.5 eV and confirmed by a measurement on Co_2TiSi . Neglecting the (only weak) energy dependence of the transition matrix elements, and using this core-hole correlation energy and spectral deconvolution, they finally found that the Fermi level of Co_2TiSn is at the edge of the minority valence band, i.e., Co_2TiSn would be on the verge of being a half-metal. With the same method, they found that Co_2MnSi has half-metallic character for the unoccupied density of states.

Using the FEFF9 calculations, we can invert this procedure. From *ab initio* calculations we found the Fermi energy by fitting the experimental spectrum. Now we can use the same Fermi energy and investigate the ground state DOS calculated by FEFF9. The Co site projected d DOS are shown together with the

SPRKKR calculation in Fig. 6.8. First, we shall note that the ground state DOS from FEFF9 and the SPRKKR calculation produce principally the same features, but FEFF9 underestimates the splitting between the bonding and the anti-bonding states. This is because of the spherical potential approximation and the use of the von Barth-Hedin exchange correlation potential. The unoccupied DOS are however in good agreement. Because of finite cluster size effects, the DOS from FEFF9 is broadened. The minority states gap can be identified just below the calculated Fermi level. When comparing the DOS in presence of the core hole to the ground state, we find that the curve is mainly shifted to lower energies by $\Delta E_C \approx 0.3$ eV. In the unoccupied DOS, this is best seen for the minority e_g peak, which shifts below the calculated E_F . Instead, the Co-Ti t_{2g} peak at 1.4 eV remains essentially unaltered. That is in remarkable agreement with the procedure given by Klaer *et al.*. When the same Fermi level is applied to the ground state density as to the excited state density, we can conclude from our data that Co_2TiSn has half-metallic character with E_F right below the minority valence band (see dotted energy level in Fig. 6.8).

Finally, we shall discuss the limitations of our model. As mentioned above, the *ab initio* calculation underestimates the double-peak splitting of the XAS by about 0.2 eV. This introduces an uncertainty in the Fermi energy determination by spectral fitting of the order of the correction itself. With the currently available level of *ab initio* theory this issue can not be resolved and it remains unclear if Co_2TiSn is a half-metallic ferrimagnet. At least, a full potential treatment would be desirable, and spin self-consistency with more advanced exchange correlation functionals may help to resolve problems with the exchange splitting. On the other hand, the SPRKKR calculation finds the t_{2g} peak at slightly lower energy than FEFF9. Thus it is possible that a more accurate calculation of the XAS requires approaches going beyond DFT.

7 Ferrimagnetism and disorder of epitaxial $\text{Mn}_{2-x}\text{Co}_x\text{VAI}$ Heusler compound thin films

7.1 Introduction

In this chapter, we attempt to test Galanakis' prediction of a full magnetic compensation in the $\text{Mn}_{2-x}\text{Co}_x\text{VAI}$ (MCVA) system [40]. For many practical applications it is necessary to prepare high quality thin films of the magnetic materials. Therefore one has to find suitable deposition techniques and optimize the parameters. The parent compounds Mn_2VAI and Co_2VAI [117, 118] have been successfully synthesized in the bulk and epitaxial growth of Mn_2VAI films with $L2_1$ ordering on MgO (001) single crystals was also demonstrated [119, 120]. Experimental results on the structural and magnetic properties of epitaxial $\text{Mn}_{2-x}\text{Co}_x\text{VAI}$ thin films are presented here.

Disorder is a major concern when dealing with half-metallic Heusler compounds. The presence of disorder has been repeatedly demonstrated for Co_2 -based Heusler bulk and thin films (see, e.g., [121, 122, 123, 124]). Theoretical studies have investigated the impact of disorder on the magnetic properties and the half-metallicity of the compounds [39, 125, 126, 127, 128, 129]. For some compounds major impact of disorder on the half-metallicity is observed, which also depends on the type of disorder. Particularly, Picozzi *et al.* [125] found that a Mn atom substituting a Co atom in Co_2MnSi , which has Mn as nearest neighbors, would couple antiparallel to the surrounding Mn atoms, and thus reduce the total magnetization drastically. The strong dependence of the magnetic moment of Mn on its chemical and magnetic environment has been demonstrated by, e.g., Rader *et al.* [130]. Hence, disorder bringing Mn into nearest-neighbor positions has to be controlled.

7.2 Methods

7.2.1 Experimental details

The samples were deposited with the BESTEC sputter system (Chapter 2.1). Elemental targets of Mn, Co, V, and Al of 99.95% purity were used. The sputtering pressure was set to $2 \cdot 10^{-3}$ mbar. The correct sputter power ratios were set up using a combined x-ray reflectivity and x-ray fluorescence technique.

All samples used in this study had the following stack sequence: MgO (001) single crystal / $Mn_{2-x}Co_xVAl$ 18 nm / Mg 0.5 nm / MgO 1.5 nm with $x = 0 / 0.5 / 0.9 / 1.0 / 1.1 / 1.5 / 2$. The upper MgO was deposited by e-beam evaporation. Diffraction measurements on Mn_2VAl films deposited at various temperatures revealed that a substrate carrier temperature of at least 600°C was necessary to obtain good order, but temperatures above 700°C lead to strong Mn sublimation, which can not be reliably compensated by higher sputtering power (compare with [119]). Therefore all samples discussed in this paper were deposited at a carrier temperature of 700°C. The protective Mg / MgO bilayer was deposited after cooling the samples to prevent oxidation and interdiffusion.

X-ray diffraction (XRD), reflectometry (XRR), and fluorescence (XRF) were performed in the Philips X'Pert Pro MPD diffractometer with Bragg-Brentano and collimator point focus optics, the open Euler cradle and the Amptek fluorescence detector in a He enclosure.

X-ray magnetic circular dichroism (XMCD) was measured at beamline 6.3.1 of the Advanced Light Source (Berkeley, CA, USA). A magnetic field of ± 1.6 T parallel to the incoming x-ray beam was applied, the sample surfaces were inclined by 30° with respect to the incoming beam. Element specific magnetic hysteresis loops were taken with a magnetic field of up to ± 2 T. The magnetic field was switched for every energy point to obtain the dichroic signal. Data were taken at 20 K, 150 K, 200 K, and 300 K. All XMCD spectra were taken at least twice, with circular polarization degrees of +60% and -60%, respectively. Systematic measurements were performed in the surface sensitive total electron yield mode, and the visible light fluorescence of the MgO substrate was detected by a photo diode behind the sample (see Chapter 2.4). Thus, bulk information of the films could be obtained in x-ray transmission.

7.2.2 Electronic structure calculations

Electronic structure calculations of disordered compounds were performed with the *Munich* SPRKKR package, see Chapter 3.2.2. The ground state self-consistent potential calculations were performed on 834 **k** points in the irreducible wedge of the Brillouin zone. The exchange-correlation potential was approximated with the Perdew-Burke-Ernzerhof implementation of the generalized gradient approximation [69], the Fermi energy was determined using Lloyd's formula [74, 75]. The angular momentum expansion was taken up to $l_{\max} = 3$. A scalar relativistic representation of the valence states was used in all cases, thus neglecting the spin-orbit coupling. For Mn_2VAI the atomic spheres approximation was applied and Co_2VAI was treated with full potential calculations. Half-metallic ground states were obtained for Mn_2VAI and Co_2VAI with their respective bulk lattice parameters. To account for disorder, the coherent potential approximation (CPA) was used. In our calculations with the ideally ordered L2_1 structure, Mn_2VAI has a total moment of $2.01 \mu_{\text{B}}/\text{f.u.}$, with $1.54 \mu_{\text{B}}$ on Mn and $-1.03 \mu_{\text{B}}$ on V. Co_2VAI has a total moment of $1.99 \mu_{\text{B}}/\text{f.u.}$, with $0.87 \mu_{\text{B}}$ on Co and $0.28 \mu_{\text{B}}$ on V. These values are in good agreement with calculations presented by other authors [131].

7.3 Experimental results and discussion

7.3.1 Lattice structure

All MCVA films were found to be highly epitaxial with MCVA [001] || MgO [001], rocking curve widths of 0.6° to 1.5° , and an MCVA [100] || MgO [110] in-plane relation. Laue oscillations observed at the (002) reflections demonstrate the lattice and interface coherence of the films in the two limiting cases of Mn_2VAI and Co_2VAI (Fig. 7.3.1(a)). For $x = 1$, however, the oscillations are less pronounced.

Figure 7.3.1(b) displays the out-of-plane lattice parameter c as a function of x . According to Vegard's law [132], a linear decrease of the lattice parameter with increasing x can be expected for a simple substitutional model. However, a significant deviation from this law is observed at $x = 1$. This indicates, as we will see in detail later, a structural and magnetic order-disorder transition. For Mn_2VAI , c is slightly lower than the bulk value of 5.875 \AA [42]; Co_2VAI has also a slightly reduced c compared to the bulk value of 5.77 \AA [117]. This is compatible with a tetragonal distortion caused by the epitaxial matching

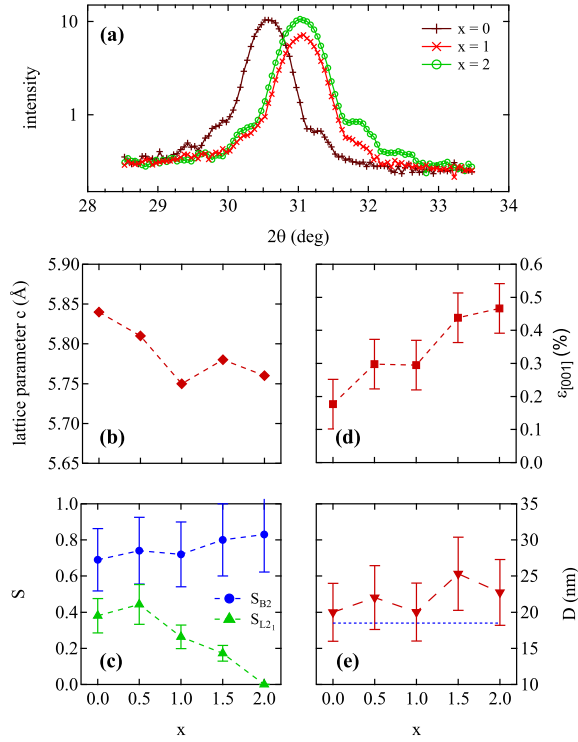


Figure 7.1: **(a)**: θ - 2θ scans of the (002) reflections of Mn_2VAI ($x = 0$), Mn_1Co_1VAI ($x = 1$), and Co_2VAI ($x = 2$). Clear Laue oscillations are visible in both cases. **(b)**: out-of-plane lattice parameter c as function of x . **(c)**: Order parameters S_{B2} and S_{L21} as functions of x . **(d)**: Microstrain $\epsilon_{[001]}$ and **(e)**: coherence length D and as functions of x . The dashed line in **(e)** denotes the film thickness.

with the substrate: the lattice is expanded in the plane and shrinks in the out-of-plane direction. For the case of Co_2TiSn we have recently performed first principles calculations of the change in total energy for this type of lattice distortion. In this case it is of the order of 25 – 50 meV, and is thus easily activated during the film growth [104]. For the compounds presented here, we expect a similar energy range.

Takamura's extended order model for Heusler compounds [133] was applied to obtain the order parameters S_{B2} and S_{L21} from the measured XRD

peak intensities. The order parameters describe the relative occupation of the individual sublattices of the structure with the "right" and "wrong" atoms. The degree of B2 order (i.e., the degree of ordering between the X and the Y/Z sublattices) is defined as

$$S_{B2} = \frac{n_{\text{Mn/Co on X-sites}} - n_{\text{Mn/Co on X-sites}}^{\text{random}}}{n_{\text{Mn/Co on X-sites}}^{\text{full order}} - n_{\text{Mn/Co on X-sites}}^{\text{random}}}. \quad (7.1)$$

Correspondingly, the degree of L2₁ ordering is defined by

$$S_{L2_1} = \frac{n_{\text{V on Y-sites}} - n_{\text{V on Y-sites}}^{\text{random}}}{n_{\text{V on Y-sites}}^{\text{full order}} - n_{\text{V on Y-sites}}^{\text{random}}}. \quad (7.2)$$

Therefore, $S_{B2/L2_1}$ is 1 if the compound is fully ordered and is reduced with increasing disorder. $S_{B2/L2_1} = 0$ means random occupation of the sublattices. The order parameters can be obtained from x-ray diffraction measurements, by comparing the experimentally observed intensity ratios with calculated ideal values, see Chapter 2.2.1 and Ref. [133] for details. Unlike Webster's model [51], Takamura's model takes the dependence of S_{L2_1} on S_{B2} into account.

The structure factors were obtained from the measured intensities by correcting for the Lorentz-Polarization term and the temperature factor with an effective Debye-Waller factor of $B_{\text{eff}} = 0.4$. S_{B2} is calculated from the four structure factor ratios of (002) and (222) versus (022) and (004), respectively. S_{L2_1} is calculated as the average of the (111) structure factor versus (022) and (004). The full atomic scattering factors including angular dependence and anomalous corrections were used in the numerical model calculations. As shown in Fig. 7.3.1(c), the Mn₂VAl films are ordered in the L2₁ structure with significant V-Al disorder ($S_{L2_1} \approx 0.4$). With increasing Co content, the L2₁ order disappears in the alloy system; Co₂VAl does not show any sign of L2₁ ordering. On the other hand, the degree of B2 order increases slightly with increasing Co content, from $S_{B2} = 0.7$ to $S_{B2} = 0.8$, i.e., 85 % to 90 % of the Co atoms are on the 8c sites. However, we note here that disorder between Co, Mn, and V can not be identified with this method, because the atomic form factors are too similar.

A Williamson-Hall analysis (Chapter 2.2.1) of the integral peak widths of the (002), (004), and (006) reflections was performed. The analysis results are displayed in Fig. 7.3.1(d) and (e). The measured coherence length matches the film thicknesses quite well within the accuracy of the measuring and fitting procedure. A clear trend of increasing strain can be observed, from 0.18 % to

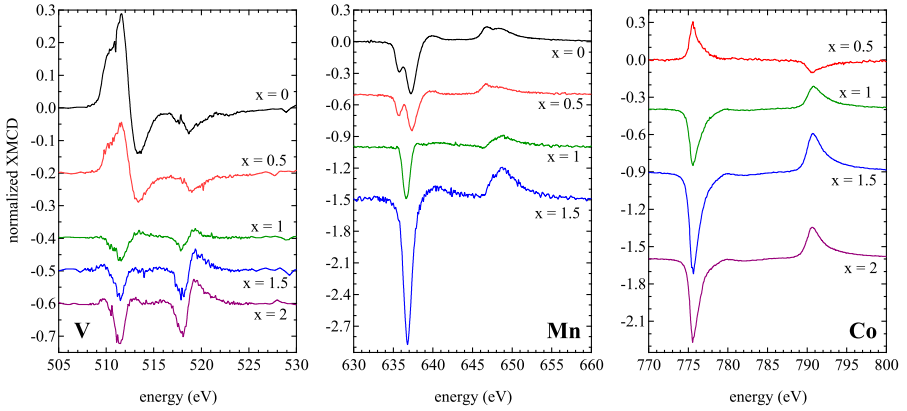


Figure 7.2: Experimental XMCD spectra for V, Mn, and Co at 20 K. The corresponding XAS spectra were normalized to a post-edge jump height of 1. The spectra for $x = 0.9, 1.1$ are similar to $x = 1$ and are omitted for clarity.

0.47 %. The lattice mismatch of Co_2VAI (3.1 %) is about 2.4 times as large as the mismatch of Mn_2VAI (1.3 %) with MgO . The same factor applies to the strain values, which verifies the high quality of the epitaxy. The lower degree of film coherence, the deviation from Vegard's law and the rather low strain in spite of the large lattice mismatch indicate an increased density of lattice defects in Mn_1Co_1VAI . The defects allow for relaxation of the film, which can reduce the microstrain at a loss of coherence.

Ziebeck and Webster found that Co_2VAI crystallizes in the $L2_1$ phase, but exhibits some preferential V-Al disorder [117]. The samples measured by them were annealed at $800^\circ C$ for 24h. The samples by Kanomata *et al.* were annealed at up to $1200^\circ C$, and still exhibited a complex grain structure consisting of $L2_1$ and B2 ordered fractions. Deposition at $700^\circ C$ may thus be insufficient to promote $L2_1$ order in Co_2VAI . However, as stated initially, a higher deposition temperature was not usable because of Mn sublimation.

7.3.2 Magnetic and electronic structure

We begin with a discussion of the XMCD spectra in dependence on x , which are shown in Fig. 7.2. For $x = 0$, i.e., for pure Mn_2VAI , we find an antiparallel alignment of the Mn and V moments, which was verified with element specific

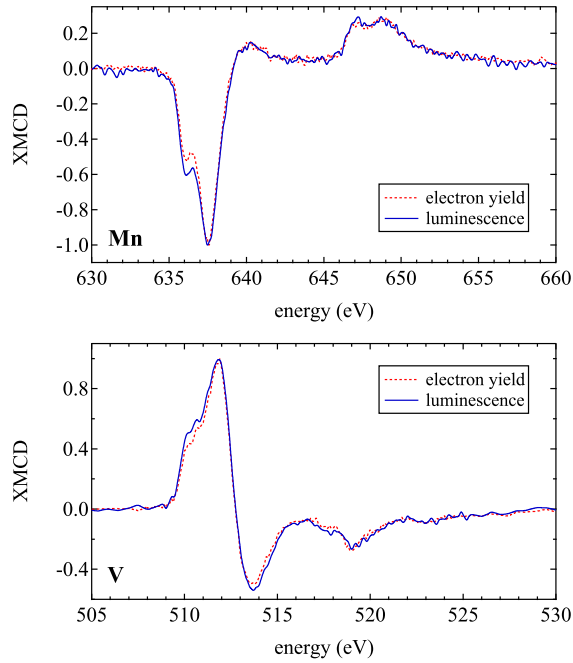


Figure 7.3: Normalized XMCD spectra of Mn and V in electron yield and luminescence detection.

hysteresis loops (not shown). This is preserved up to $x = 0.5$, going along with an antiparallel coupling of Co to Mn. Here, we find the predicted ferrimagnetic order with the Co and V moments pointing opposite to the Mn moments. With further increasing x , all magnetic moments point in the same direction; the alloys become ferromagnets. This transition is closely related to chemical disorder which is indicated by the deviation of the lattice parameter from Vegard's law. Across the stoichiometry series the shape of the spectra changes significantly. Most prominently, the splitting of the V and Mn lines vanishes at $x = 0.9$ and above. The appearance of this splitting is directly correlated with the appearance of ferrimagnetism. The line shape of the Mn XMCD for $x = 1.5$ is very similar to the Mn line shape in Co_2MnAl or Co_2MnSi [134]. For the ferrimagnetic coupling of Co and Mn, they have to be second nearest neighbors on octahedral positions. Co and Mn on tetrahedral nearest-neighbor positions

couple ferromagnetically, as in Co_2MnGe [51] and the other Co_2Mn -based Heusler compounds.

To assert that the complex shape of the Mn and V spectra is not a surface effect, we have measured the transmitted x-ray intensity in luminescence detection at room temperature for Mn_2VAl . The XMCD spectra are almost equal in total electron yield and in transmission (see Figure 7.3.2), although in both cases the L3 pre-peak is more pronounced in transmission. However, compared to the total area of the peaks, this deviation is small. The fine structure of the spectra is consequently related to the electronic structure of the films rather than to a surface effect.

Using the sum rule analysis (Chapter 2.4.2) we extracted the spin and orbital magnetic moments from the XMCD spectra. Table 7.1 summarizes the total magnetic moments obtained from sum rule analysis and provides estimates of the Curie temperatures obtained from temperature dependent XMCD for $x = 0, 1, 2$ (the spectra are not shown here). Figure 7.3.2 displays the element specific total moments in dependence on x . Because of core-hole – photoelectron interactions, the sum rules fail for the early 3d transition metals [84]. To compensate the resulting spectral mixing effects, the apparent spin magnetic moments can be multiplied with correction factors as suggested by Dürr *et al.* and Scherz *et al.*, i.e. 1.5 for Mn [135] and 5 for V [136]. Actually, the applied correction factors depend on the actual electronic structure and can not be simply transferred to different systems. However, we assume that this influence is rather small, so that quantitative results can be obtained.

In Mn_2VAl we find a lowered Mn moment ($1 \mu_B$) and an enhanced V moment ($-1.1 \mu_B$), resulting in a total magnetization of $0.88 \mu_B/f.u.$ No change of the

	m_{tot}	T_C
Mn_2VAl	0.88	$\gg RT$
$Mn_{1.5}Co_{0.5}VAl$	0.1	-
$Mn_{1.0}Co_{1.0}VAl$	1.09	$\approx 350 K$
$Mn_{0.5}Co_{1.5}VAl$	2.29	-
Co_2VAl	1.66	$\approx 210 K$

Table 7.1: Experimental total magnetic moments at 20 K (given in $\mu_B / f.u.$) and estimated Curie temperatures derived from temperature-dependent XMCD.

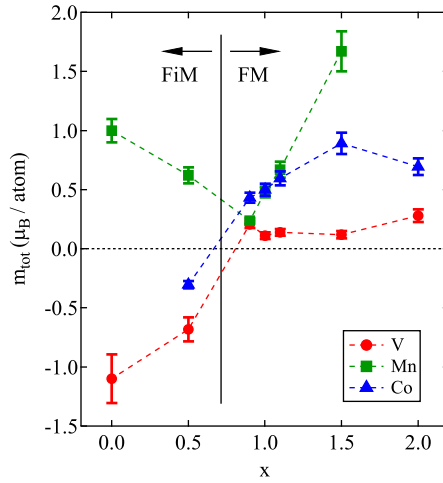


Figure 7.4: Element specific magnetic moments as functions of x . Ferrimagnetic (FiM) order is observed for $x \leq 0.5$, ferromagnetic (FM) order is observed for $x \geq 0.9$.

magnetic moments was observed at RT as compared to 20 K, hence the Curie temperature is much higher than RT. The film is not well described by a pure $L2_1$ order model. As discussed earlier, the film has some disorder between Mn and (V,Al). In this case, Mn atoms reside on sites surrounded by other Mn atoms, which couple antiferromagnetically at short distance. Indeed, by calculating the self-consistent potential in SPRKKR with 20% Mn-Al or Mn-V swap, we find antiparallel coupling of the antisites, similar to the findings by Picozzi *et al.* for Co_2MnSi [125]. For Mn-Al swap, the Mn(8a) moment is reduced to $1.22 \mu_B$ and the Mn on the Al site has $-2.48 \mu_B$. The V moment is reduced to $-0.83 \mu_B$. This results in a total magnetization of $0.85 \mu_B/\text{f.u.}$, and the average Mn moment is consequently $0.85 \mu_B$. In the case of Mn-V swap, the Mn(8a) moment remains at $1.58 \mu_B$ and the Mn on the V site has $-2.63 \mu_B$. The V moment on the 4b site is $-0.87 \mu_B$ and $+0.84 \mu_B$ on the 8a site. In this case the total moment is $1.78 \mu_B/\text{f.u.}$, with an average Mn moment of $1.16 \mu_B$. Further, the case of Mn-Al swap is energetically preferred with respect to the Mn-V swap. Seeing the low total and Mn moments and the high V moment, a preferential Mn-Al swap in Mn_2VAl is thus in good agreement with the structural and the magnetic data. Our calculations show that the 20% Mn-Al disorder and B2 disorder barely influence the half-metallic gap of Mn_2VAl . For

B2 disorder, the total magnetic moment also remains unaffected. In contrast, 20 % Mn-V disorder destroy the gap. This is in contrast to the findings by Luo *et al.*, obtained with a supercell approach in a pseudopotential code. They state that the gap is preserved under 25 % Mn-V disorder [24].

Co_2VAl has a reduced Co moment ($0.69 \mu_B$) and a V moment of $0.28 \mu_B$, giving a total magnetization of $1.66 \mu_B/f.u.$ The film has B2 order, which is expected to reduce the magnetization from the highly ordered $L2_1$ case. We find magnetic moments of $0.75 \mu_B$ for Co and $0.4 \mu_B$ for V in a B2 ordered SPRKKR calculation, with a total moment of $1.86 \mu_B/f.u.$, in good agreement with our measurements. Some additional disorder involving Co and V could explain the further reduced moments. The Curie temperature is about 210 K (see Table 7.1), which is significantly lower than the value for bulk samples (310 K [117]). A calculation of the Curie temperature with SPRKKR within the mean field approximation (Chapter 3.3) yields 352 K in the $L2_1$ case and 165 K in the B2 ordered case. The observed significant reduction of the Curie temperature in the disordered alloy is thus in agreement with theory. The half-metallic gap of Co_2VAl vanishes in the B2 structure.

At $x = 0.5$, a nearly complete magnetic compensation with a total moment of only $0.1 \mu_B/f.u.$ is observed. Remarkably, at $x = 1.5$ the total magnetic moment becomes larger than $2 \mu_B/f.u.$, caused by the high Mn moment of $1.67 \mu_B$. This is in agreement with the different Mn line shape: in, e.g., Co_2MnAl , in which Mn has a similar line shape, Mn has a moment of about $3 \mu_B$ [51]. Thus, the mechanism mainly responsible for the ferromagnetic coupling of all moments is the preferentially tetrahedral (instead of octahedral) coordination of Mn atoms with Co.

8 Itinerant and local magnetic moments in ferrimagnetic Mn_2CoGa thin films probed by x-ray magnetic linear dichroism: experiment and ab initio theory

8.1 Introduction

In this chapter, we investigate the properties of epitaxial thin films of the inverse Heusler compound Mn_2CoGa , which is investigated theoretically in Chapter 5.

Epitaxial thin films of Mn_2CoGa with (001) orientation were prepared with the BESTEC sputter machine on MgO (001) substrates. A $\text{Mn}_{50}\text{Ga}_{50}$ target and an elemental Co target were used for the deposition. The resulting Mn:Ga ratio in the films was 2.2:1, as determined by x-ray fluorescence. Co was added to match the Ga content, i.e., the stoichiometry of the unit cell can be written as $\text{Mn}_{2.1}\text{Co}_{0.95}\text{Ga}_{0.95}$.

Among the various heat treatments tested, deposition at 200°C and *in situ* post-annealing at 550°C was found to provide optimal film quality. The lattice parameter perpendicular to the surface was 5.81 \AA , which is slightly smaller than the bulk value of 5.86 \AA [28]. A small tetragonal distortion of the film is induced by the lattice mismatch with the substrate, hence the lattice is expanded in the film plane and compressed perpendicular to the plane. The bulk magnetization measured by a superconducting quantum interference device (SQUID) corresponds to $1.95(5) \mu_{\text{B}}$ / unit cell, which is very close to the bulk value. No significant change of the magnetization between 5 K and room temperature was observed, which is consistent with a Curie temperature higher than 600 K.

X-ray absorption (XAS) measurements were performed at BL4.0.2 of the Advanced Light Source in Berkeley, CA, USA. X-ray magnetic circular (XMCD)

and linear dichroism (XMLD) measurements were taken at room temperature in x-ray transmission through the film by collecting the visible and ultraviolet light fluorescence from the substrate with a photodiode. [57] The sample was saturated with a magnetic field of 0.6 T and the circular or linear polarization degree was 90 % and 100 %, respectively.

We computed the XAS, XMCD and XMLD using the Elk code (Chapter 3.4.2). The experimental bulk lattice parameter was chosen for the calculations; the small distortion and off-stoichiometry have negligible influence. The Brillouin zone integration was performed on a $16 \times 16 \times 16$ k-point mesh in the irreducible wedge, the Perdew-Burke-Ernzerhof functional [69] was chosen for exchange and correlation, and spin-orbit coupling was included in a second-variational scheme. A half-metallic ground-state was obtained with a total spin magnetic moment of $2 \mu_B$ /f.u., and site resolved spin (orbital) moments as follows: Co $1.03 \mu_B$ ($0.046 \mu_B$), Mn(B) $2.91 \mu_B$ ($0.011 \mu_B$), and Mn(C) $-1.93 \mu_B$ ($-0.019 \mu_B$). A detailed discussion of the electronic structure is given in Ref. [28].

8.2 Results

The experimental x-ray absorption and circular dichroism spectra are shown in Fig. 8.1 (a) and (b). Both x-ray absorption spectra have the typical shape of a metallic system without pronounced multiplets. However, the XMCD spectrum of Mn shows some uncommon features (see arrows in Fig. 8.1a). The Co XAS exhibits fine structures at the L_3 and L_2 resonances. There is a weak shoulder about 2.6 eV above threshold and a more pronounced one at 5 eV above threshold. The Co XMCD spectrum reflects the shoulder in the XAS. The Co and (effective) Mn moments are parallel. All these features are reproduced by the *ab initio* calculations (Fig. 8.1 (c) and (d)), which are broadened with a Lorentzian of 0.3 eV width to account for lifetime effects. We can thus identify the features in the spectra as band structure effects. The 5 eV feature in the Co XAS results from transitions into an *s-d* hybridized state of Co and Ga. It is commonly observed for Co in Co_2YZ type Heusler compounds, but its position depends on the Z element. The asymmetric line shape and the broad tails of the resonances are a consequence of $2p-3d$ *e-e* correlation [137], which is neglected in our simulations. Electron-hole correlations can significantly alter the shape of the XAS or XMCD spectra of $3d$ transition elements, even in a metallic environment (see Chapter 6). Thus, the good agreement of our

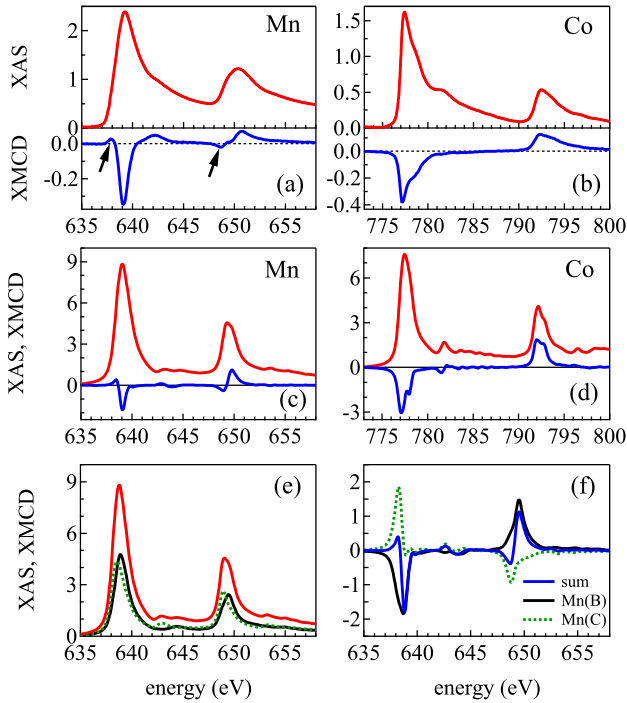


Figure 8.1: Top: experimental XAS and XMCD spectra of (a): Mn and (b): Co in Mn_2CoGa . Middle: theoretical XAS and XMCD spectra of Mn_2CoGa . (c): Mn XAS and XMCD. (d): Co XAS and XMCD. Bottom: decomposition of the Mn XAS (e) and XMCD (f) for the two inequivalent Mn sites. The theoretical spectra are normalized to 1 about 40 eV above the L_3 edge and are shifted to match the experimental absorption onset at L_3 .

calculations with the experimental spectra indicates an effective screening of the $2p$ core-hole.

In Fig. 8.1 (e) and (f) we show the decomposition of the calculated XAS and XMCD into the Mn(B) and Mn(C) components. We find that the core levels of Mn(B) and Mn(C) are slightly shifted (about 0.15 eV) against each other. The shapes of the spectra as well as the branching ratios are different, the Mn(B) branching ratio is significantly larger than the one of Mn(C). The decomposition of the XMCD spectrum shows two different signals with opposite signs. The

antiparallel Mn(C) contribution is responsible for the features marked in the experimental spectrum. These features are less pronounced in the experimental spectrum, which indicates a smaller core-level shift than the calculated one.

A sum rule analysis was performed to obtain the spin and orbital magnetic moments from the XMCD data (Chapter 2.4.2). The resulting magnetic moment ratios are: $m_{\text{spin}}^{\text{Mn}} / m_{\text{spin}}^{\text{Co}} = 0.48$, $m_{\text{orb}}^{\text{Mn}} / m_{\text{spin}}^{\text{Mn}} = -0.013$, $m_{\text{orb}}^{\text{Co}} / m_{\text{spin}}^{\text{Co}} = 0.055$. Using the bulk magnetization we derive the element specific moments. The average Mn spin moment is $0.47 \mu_B$ per atom and the Co spin moment is $0.98 \mu_B$ per atom. The average orbital moment of Mn is $-0.006 \mu_B$ per atom, being antiparallel to the spin magnetic moment. For Co we find $0.055 \mu_B$ for the orbital moment. In this analysis the apparent Mn spin moment has been multiplied by 1.5 to compensate the $2p_{1/2} - 2p_{3/2}$ channel mixing, as suggested by Dürr *et al* [135]. These values match the theoretical values within the errors. Both the positive Co orbital moment as well as the small negative Mn orbital moment are in agreement with the calculation. The orbital moments of all atoms are parallel to the respective spin moments, but the orbital moment of Mn(C) is larger than the one of Mn(B), resulting in the effectively antiparallel alignment.

The single crystalline character of epitaxial films allows to make use of the anisotropic x-ray magnetic linear dichroism, which is a sensitive probe of the local crystal field. By comparison with reference system, XMLD provides information on the locality of magnetic moments, see Chapter 2.4.3 for details.

It was shown that the Mn moment has a local character in the Heusler compounds Co_2MnSi (CMS) and Co_2MnAl (CMA).[134] Kübler *et al.* proposed an exclusion of minority d electrons from the environment of Mn, giving rise to a local moment composed of itinerant electrons [8]. A similar mechanism can give rise to a local Mn(B) moment in Mn_2CoGa [28]. Therefore, we chose CMS as a reference system with similar crystal structure for local moments. Mn_2VGa (MVG), also crystallizing in the Heusler structure, is postulated to be itinerant, and is chosen as a reference system for itinerant Mn moments.

A simple theoretical test for the (non-)locality of spin moments is based on non-collinear spin configurations. We performed self-consistent calculations for non-collinear configurations (without spin-orbit coupling) in which the magnetic moment of interest was tilted by an angle ϑ out of the common magnetization axis. Only the directions were fixed, and the magnitudes were determined self-consistently. A local moment would not change in magnitude when tilted. In Fig. 8.2 the relative changes of the magnetic moments for Mn_2CoGa and the reference systems CMS and MVG are shown. In Mn_2CoGa ,

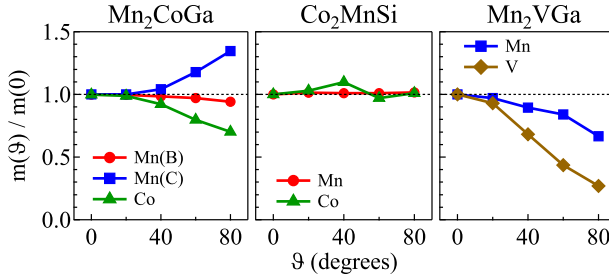


Figure 8.2: Calculated relative change of the magnetic moments for non-collinear configurations. The spin moment under investigation is tilted out of the common axis by θ .

Mn(B) has a weak dependence on θ , whereas Mn(C) and Co change significantly on tilting: Mn(B) has local character, whereas Mn(C) and Co are rather itinerant. Both the Co and the Mn moment in CMS have weak or no dependence on the tilt angle, showing clearly the locality of both moments. MVG in contrast, is an itinerant system; both the Mn and the V moment depend strongly on θ . Mn_2CoGa has a more complex magnetic structure than the reference compounds, being a hybrid between itinerant and local magnetism. Local moment systems can be described within the Heisenberg model. This has been successfully applied to explain the Curie temperatures in CMS and related compounds [80]. For MVG, this model underestimates the Curie temperature, similar to fcc Ni (Chapter 3.3). This can be seen as experimental evidence for the itinerancy of MVG. Consequently, we expect significant deviation of experimental Curie temperatures from theoretical values for Mn_2CoGa .

We have performed XMLD measurements for Co and Mn along the [110] direction of the film. In Fig. 8.3 we show the experimental and theoretical spectra of Mn_2CoGa and the reference compounds. All XMLD data were taken at the same beamline and are directly comparable in terms of energy resolution.

The Co XMLD of Mn_2CoGa is very similar in shape to the signal of CMS, all fine details are reproduced. The computed spectrum of Mn_2CoGa resembles the general shape of the experimental data, although the negative contributions are overestimated. These are in the tails of the resonances, in which e - e correlation plays a role, which we neglect as stated above. The local crystal fields are consequently similar in Mn_2CoGa and CMS, and the *ab initio* calculation is able to describe these reasonably well.

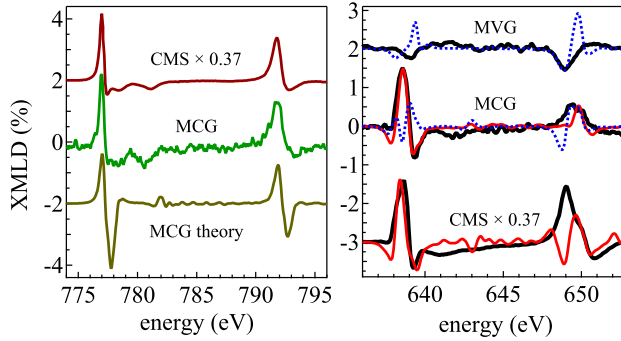


Figure 8.3: Left: Experimental and theoretical Co XMLD spectra of Mn_2CoGa and Co_2MnSi (experimental spectrum from Ref. [134]). Right: Experimental (black solid lines) and theoretical (thin lines) Mn XMLD spectra of Mn_2VGa , Mn_2CoGa and Co_2MnSi (experimental spectrum from Ref. [134]). Mn(B) type spectra are solid red, Mn(C) type spectra are dotted blue. The XMLD is normalized to the L_3 resonance height. All theoretical spectra are shifted and expanded to match the experimental absorption onset at L_3 and the $L_{3,2}$ spin-orbit splitting. They are scaled to match the experimental intensities.

For Mn, we find that the Mn_2CoGa and the CMS signals are virtually equal at L_3 . At L_2 however, they are somewhat different. Mn_2CoGa has an overall less pronounced structure and less intensity here. The MVG signal is much weaker and has an entirely different shape, which indicates different crystal fields acting on Mn on a B or C position. The computed spectra of Mn(B) in Mn_2CoGa and for CMS resemble the experimental data at L_3 very well. At L_2 , significant deviation is observed, particularly for CMS. The main peak at L_2 in CMS stems from a feature in the XAS that was assigned to an atomic multiplet, that survives the band formation and corroborates the locality of the moment [134]. In Mn_2CoGa this feature is less pronounced, leading to a better agreement of experiment and theory. Less locality of the Mn(B) moment in comparison to CMS can be inferred from that. The influence of the Mn(C) spectrum in Mn_2CoGa can not be traced in the experimental data. The calculated Mn(C) spectrum is, however, very similar to the computed XMLD of MVG. This, in turn, agrees only modestly with experiment. Because of the similarity of the computed spectra, we assume that the actual Mn(C) contribution would have similar shape as the measured MVG spectrum. The Mn_2CoGa XMLD is, in

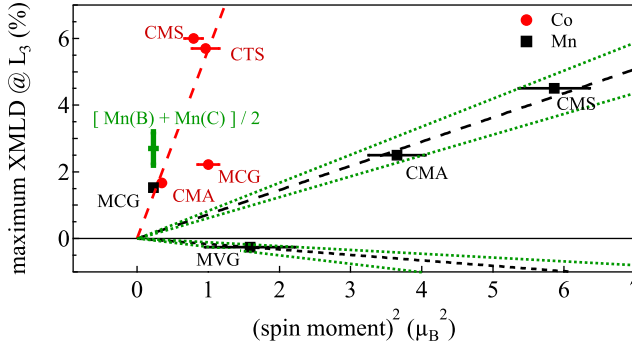


Figure 8.4: XMLD vs. m_s^2 for various Mn and Co containing (inverse) Heusler compounds: Co_2MnSi (CMS), Co_2MnAl (CMA), Co_2TiSn (CTS), Mn_2VGa (MVG), and Mn_2CoGa (MCG).

conclusion, clearly dominated by the Mn(B) signal.

Now we turn to the observed intensities of the XMLD signals. Fig. 8.4 shows a comparison of the maximum XMLD signals (defined as $(I^{\parallel} - I^{\perp})|_{\max} / [(I^{\parallel} + I^{\perp})/2]|_{\max}$) at the L_3 edges versus the squared spin magnetic moments of Co and Mn for CMS, CMA, Co_2TiSn (CTS), MVG, and Mn_2CoGa . The CTS data were taken from Chapter 6. The Co XMLD amplitudes are close to a common line for CMS, CMA, and CTS. CMS is a bit above though, indicating a stronger locality of the Co moment in CMS than in CMA or CTS. The Mn_2CoGa signal is about a factor of 2.5 smaller than expected from the references. In agreement with the locality test described above, this shows the itinerancy of the Co moment in Mn_2CoGa . Because of the antiparallel Mn moments, the Mn XMLD of Mn_2CoGa is very strong compared to the Mn spin moment, and it is far off the line given by CMS and CMA.

With the linear fits through the CMA and CMS points as a guide for local Mn moments and through the MVG point for an itinerant system we can predict the Mn XMLD amplitude of Mn_2CoGa . We treat the Mn XMLD of Mn_2CoGa as a superposition of the spectra from CMA/CMS and MVG. Our FLAPW calculation gives a Mn(B)/Mn(C) spin moment ratio of -1.5 . With this value and the measured sum $m_s^{\text{Mn(B)}} + m_s^{\text{Mn(C)}} \approx 0.94 \mu_B$ we obtain $m_s^{\text{Mn(B)}} = 2.82 \mu_B$ and $m_s^{\text{Mn(C)}} = -1.88 \mu_B$. According to the errors of the magnetic moments of the reference data, we expect an XMLD of $(2.7 \pm 0.5)\%$ for Mn_2CoGa . The measured value of 1.53% is clearly below this range; the ratio determined directly from

the XMLD is -1.7 , which leads to $m_s^{\text{Mn(B)}} = 2.28 \mu_{\text{B}}$ and $m_s^{\text{Mn(C)}} = -1.34 \mu_{\text{B}}$. Though this is still reasonable, it seems much more likely that the lower XMLD in Mn₂CoGa indicates a lower degree of Mn(B) spin moment locality than in CMS. However, the Mn(B) moment is clearly not purely itinerant.

9 Concluding remarks

Ab initio computations for the Mn_2TiZ Heusler compound series with $Z = \text{Al, Ga, In, Si, Ge, Sn, P, As, Sb}$, suggest that these compounds can exhibit ferrimagnetism in accordance with the rule $m = N_V - 24$. These calculations were performed with two different, state-of-the-art density functional theory methods: the full-potential linearized augmented plane waves method (FLAPW) and the (full-potential) spin-polarized relativistic Korringa-Kohn-Rostocker method (SPRKKR). The results are in good agreement with each other. Most of the compounds have large spin polarization and a spin-up gap forms above the Fermi energy. The Curie temperatures calculated within the mean-field approximation indicate that the compounds with 21 and 22 valence electrons will be ferrimagnetic at room temperature. A thorough understanding of the influence of the Z component on the properties of the compounds has been established on the basis of *ab initio* band structure and exchange coupling calculations. It was found that the pressure dependence of T_C is positive, in agreement with ferromagnetic full Heusler compounds. Because of their large and stable spin polarizations and their high Curie temperatures we propose in particular Mn_2TiSi , Mn_2TiGe , and Mn_2TiSn as candidates for spintronic applications.

We have performed *ab initio* band structure calculations with the SPRKKR method on the Mn_2CoZ inverse Heusler compounds with the Hg_2CuTi structure. The exchange interaction parameters obtained from the calculations are found to be governed by the Co-Mn(C) exchange, which is of direct nature. In the case of $Z = \text{Al, Ga, and In}$, the Mn(C)-Mn(C) interaction is the dominating one, which is direct as well. The indirect, long-ranged interactions are exponentially damped and thus weak, and the intra-sublattice interactions are mostly antiferromagnetic. Curie temperatures calculated within the mean-field approximation are in reasonable agreement with experimental data for Mn_2CoSn and Mn_2CoSb . The Curie temperatures show an anomalous dependence on the total moment, which is different from the full Heusler compounds. For Mn_2CoAl we predict an exceptionally high Curie temperature of 890 K, although the total moment of the compound is only $2 \mu_B / \text{f.u.}$ The dependence

of the exchange parameters on the lattice parameter in Mn_2CoGe suggests a negative pressure dependence of T_C in the Mn_2CoZ compounds, which originates from the exchange interactions of Mn(C)-Mn(B) and Co-Mn(C).

We have grown thin films of the Heusler compound Co_2TiSn by DC magnetron co-sputtering. Structural investigations revealed highly ordered, fully epitaxial growth of Co_2TiSn thin films on MgO (001) substrates at growth temperatures above 600°C . A low residual resistivity supports the conclusion of well ordered films. The resistivity has a pronounced cusp-type anomaly at T_C . A large magnetoresistance has been observed and can be explained in terms of spin fluctuations. From the XMCD measurements we find a total magnetization of $1.98 \pm 0.05 \mu_B / \text{f.u.}$, where the uncertainty arises from the unknown systematic error in the estimate of the Ti spin moment; the reduced average saturation magnetization of the best film ($T_S = 700^\circ\text{C}$, $m = 1.6(1) \mu_B / \text{f.u.}$) can be easily explained by an oxidized bottom interface layer of 3 nm thickness. The results for the element specific spin and orbital magnetic moments are in quantitative agreement with *ab initio* band structure theory. The fine structures observed for the Co $L_{3,2}$ edges were explained by direct calculations of the XAS using FEFF9. Inclusion of the core-hole potential was found to reproduce the split white lines, assessing them as band structure effects. Formation of atomic multiplets can be ruled out, in agreement with XMLD results. However, due to shortcomings of the theoretical modeling, it remains unclear whether Co_2TiSn is a half-metallic ferrimagnet or not.

Epitaxial thin films of $\text{Mn}_{2-x}\text{Co}_x\text{VAl}$ have been synthesized on MgO (001) substrates by DC and RF magnetron co-sputtering. It was intended to observe a ferrimagnetic compensation of the magnetization at $x = 1$. The films have significant chemical disorder, depending on the degree of Mn-Co substitution. Mn_2VAl was found to be $L2_1$ ordered, with a preferential Mn-Al disorder and additional V-Al disorder. The Mn-Al disorder reduces the total moment considerably, because the nearest-neighbor Mn atoms couple antiferromagnetically in this configuration. Accordingly, the magnetization of Mn_2VAl is very sensitive to disorder involving Mn. However, the band structure calculations suggest that only Mn-V disorder has an influence on the half-metallic gap. Because of the disorder, a nearly complete magnetic compensation was observed for $\text{Mn}_{1.5}\text{Co}_{0.5}\text{VAl}$. With further Co substitution, the electronic structure changes considerably, and a parallel coupling of Co, Mn, and V was observed. We suppose that Co and Mn become preferentially nearest-neighbors, which leads to a parallel coupling of their magnetic moments. The Co_2VAl films, being the second extremum of the substitutional series, had B2 order. The band structure

calculations with B2 order suggest reduced moments, but the experimentally determined moments are even lower, which indicates additional disorder involving Co. The Curie temperature was significantly reduced, which is in agreement with the trend observed in the mean field calculation. It is in principle possible to obtain a high degree of L2₁ order in bulk Co₂VAl by appropriate thermal treatment, but our maximum substrate temperature was limited by Mn evaporation. While it may be possible to obtain the correct occupation for the ferrimagnetic compensation in the bulk, it seems not possible to obtain films with a high degree of order.

We have prepared epitaxial films of the ferrimagnetic inverse Heusler compound Mn₂CoGa by co-sputtering and obtained good film quality by deposition at 200°C and *in situ* post-annealing at 550°C. We found good agreement of the experimental L_{3,2} x-ray absorption and dichroism spectra with *ab initio* calculations within independent particle theory. The total and element resolved magnetic moments are close to theoretical values. X-ray magnetic linear dichroism spectra were taken to provide information on the locality of the Co and Mn moments. Non-collinear electronic structure calculations provided the footing for the interpretation of the observed XMLD amplitudes. The locality of the Mn(B) moment is not as pronounced as in Co₂MnSi, the Co and Mn(C) moments have clearly itinerant character. Because of these findings, we expect significant deviation of experimental Curie temperatures from the predicted ones in the Mn₂CoZ compounds.

In all experimental parts of this work, density functional theory has proven to be an indispensable tool for the interpretation of the obtained data. Direct comparison of experiment and *ab initio* theory provides a much deeper understanding of the underlying physics than empirical work alone.

Bibliography

- [1] F. Heusler, *Verh. dt. phys. Ges.* **5**, 219 (1903).
- [2] A. J. Bradley and J. W. Rodgers, *Proc. R. Soc.* **57**, 115 (1934).
- [3] T. Graf, S. S. P. Parkin, and C. Felser, *IEEE Trans. Magn.* **47**, 367 (2011).
- [4] H. Itoh, T. Nakamichi, Y. Yamaguchi, and N. Kazama, *Trans. Japan Inst. Met.* **24**, 265 (1983).
- [5] Y. Nishino, M. Kato, S. Asano, K. Soda, M. Hayasaki, and U. Mizutani, *Phys. Rev. Lett.* **79**, 1909 (1997).
- [6] H. Nakamura, Y. Kitaoka, K. Asayama, Y. Onuki, and T. Komatsubara, *J. Magn. Mater.* **76**, 467 (1988).
- [7] J. Winterlik, G. H. Fecher, C. Felser, M. Jourdan, K. Grube, F. Hardy, H. von Löhneysen, K. L. Holman, and R. J. Cava, *Phys. Rev. B* **78**, 184506 (2008).
- [8] J. Kübler, A. R. Williams, and C. B. Sommers, *Phys. Rev. B* **28**, 1745 (1983).
- [9] W. E. Pickett and J. S. Moodera, *Physics Today* **54**, 39 (2001).
- [10] Y. Yoshida, M. Kawakami, and T. Nakamichi, *J. Phys. Soc. Japan* **50**, 2203 (1981).
- [11] C. Jiang, M. Venkatesan, and J. M. D. Coey, *Solid State Commun.* **118**, 513 (2001).
- [12] S. Ishida, S. Asano, and J. Ishida, *J. Phys. Soc. Japan* **53**, 2718 (1984).
- [13] R. Weht and W. E. Pickett, *Phys. Rev.* **60**, 13006 (1999).
- [14] K. Nakamura, T. Ito, and A. J. Freeman *Phys. Rev. B* **72**, 064449 (2005).
- [15] I. Galanakis, K. Özdoğan, E. Şaşıoğlu, and B. Aktaş, *Phys. Rev. B* **74**, 140408 (2006)
- [16] H. van Leuken and R. A. de Groot *Phys. Rev. Lett.* **74**, 1171 (1995).
- [17] W. E. Pickett, *Phys. Rev. B* **57**, 10613 (1998).
- [18] H. Akai and M. Ogura, *Phys. Rev. Lett.* **97**, 026401 (2006).
- [19] E. Şaşıoğlu, *Phys. Rev. B* **79**, 100406(R) (2009).

-
- [20] K. Özdoğan, I. Galanakis, E. Şaşıoğlu and B. Aktaş, *J. Phys.: Condens. Matter* **18** 2905 (2006).
- [21] S. Fujii, M. Okada, S. Ishida, and S. Asano, *J. Phys. Soc. Jpn* **77**, 074702 (2008).
- [22] S. Wurmehl, H. C. Kandpal, G. H. Fecher, and C. Felser, *J. Phys.: Condens. Matter* **18**, 6171 (2006).
- [23] I. Galanakis, P. H. Dederichs, and N. Papanikolaou, *Phys. Rev. B* **66**, 174429 (2002).
- [24] H. Luo, Z. Zhu, L. Ma, S. Xu, X. Zhu, C. Jiang, H. Xu, and G. Wu, *J. Phys. D: Appl. Phys.* **41**, 055010 (2008).
- [25] H. Luo, G. Liu, Z. Feng, Y. Li, L. Ma, G. Wu, X. Zhu, C. Jiang, and H. Xu, *J. Magn. Magn. Mater.* **321**, 4063 (2009).
- [26] H. Luo, Z. Zhu, G. Liu, S. Xu, G. Wu, H. Liu, J. Qu, and Y. Li, *J. Magn. Magn. Mater.* **320**, 421 (2008).
- [27] H. Z. Luo, H. W. Zhang, Z. Y. Zhu, L. Ma, S. F. Xu, G. H. Wu, X. X. Zhu, C. B. Jiang, and H. B. Xu, *J. Appl. Phys.* **103**, 083908 (2008).
- [28] G. D. Liu, X. F. Dai, J. L. Chen, Y. X. Li, G. Xiao, and G. H. Wu, *Phys. Rev. B* **77**, 014424 (2008).
- [29] N. Xing, H. Li, J. Dong, R. Long, and C. Zhang, *Computational Materials Science* **42**, 600 (2008).
- [30] X. P. Wei, X. R. Hu, G. Y. Mao, S. B. Chu, T. Lei, L. B. Hu, and J. B. Deng, *J. Magn. Magn. Mater.* **322**, 3204 (2010).
- [31] N. Lakshmi, R. K. Sharma, and K. Venugopalan, *Hyperfine Interactions* **160**, 227 (2005).
- [32] X. Dai, G. Liu, L. Chen, J. Chen, and G. Wu, *Solid State Comm.* **140**, 533 (2006).
- [33] R. B. Helmholdt and K. H. J. Buschow, *J. Less-Common Met.* **128**, 167 (1987).
- [34] H. Luo *et al.*, *J. Appl. Phys.* **105**, 103903 (2009).
- [35] S. T. Li, Z. Ren, X. H. Zhang, and C. M. Cao, *Physica B: Cond. Matter* **404**, 1965 (2009).
- [36] J. Winterlik *et al.*, *Phys. Rev. B* **83**, 174448 (2011).
- [37] P. Klaer *et al.*, *Appl. Phys. Lett.* **98**, 212510 (2011).

- [38] H. C. Kandpal, V. Ksenofontov, M. Wojcik, R. Seshadri, and C. Felser, *J. Phys. D: Appl. Phys.* **40**, 1507 (2007)
- [39] Y. Miura, M. Shirai, K. Nagao, *J. Appl. Phys.* **99**, 08J112 (2006)
- [40] I. Galanakis, K. Özdoğan, E. Şaşıoğlu, and B. Aktaş, *Phys. Rev. B* **75**, 092407 (2007).
- [41] M. Kawakami, Y. Yoshida, T. Nakamichi, S. Ishida, and H. Enokiya, *J. Phys. Soc. Jpn.* **50**, 1041 (1981).
- [42] T. Nakamichi and C. V. Stager *J. Magn. Magn. Mater.* **31**, 85 (1983).
- [43] E. Şaşıoğlu, L. M. Sandratskii, and P. Bruno *J. Phys.: Condens. Matter* **17**, 995 (2005).
- [44] L. Chioncel, E. Arrigoni, M. I. Katsnelson, and A. I. Lichtenstein, *Phys. Rev. B* **79**, 125123 (2009).
- [45] H. Luo, Z. Zhu, L. Ma, S. Xu, X. Zhu, C. Jiang, H. Xu, and G. Wu, *J. Phys. D: Appl. Phys.* **41**, 055010 (2008).
- [46] S. Swann, *Phys. Technol* **19**, 67 (1988).
- [47] BESTEC, BERLIN (2008).
- [48] B. D. Cullity and S. R. Stock, *Elements of X-Ray Diffraction*, Third Edition, Prentice Hall, Upper Saddle River 2001.
- [49] B.L. Henke, E.M. Gullikson, and J.C. Davis. X-ray interactions: photoabsorption, scattering, transmission, and reflection at E=50-30000 eV, Z=1-92, *Atomic Data and Nuclear Data Tables* Vol. 54 (no.2), 181-342 (July 1993).
- [50] D. T. Cromer and D. Liberman, *Acta Cryst.* **A37**, 267-268 (1981).
- [51] P. J. Webster, *J. Phys. Chem. Solids* **32**, 1221 (1971).
- [52] G. K. Williamson and W. H. Hall, *Acta Metall.* **1**, 22 (1953).
- [53] D. Attwood, *Soft X-Rays and Extreme Ultraviolet Radiation*, Cambridge University Press, Cambridge 1999.
- [54] L. G. Parratt, *Phys. Rev.* **95**, 359 (1954).
- [55] H. Ebel, *X-Ray Spectrom.* **28**, 255 (1999).
- [56] Y. U. Idzerda, C.T. Chen, H. J. Lin, G. Meigs, G.H. Ho, and C. C. Kao, *Nucl. Instrum. Methods Phys. Res. A* **347**, 134 (1994).

-
- [57] M. Kallmayer, H. Schneider, G. Jakob, H. J. Elmers, B. Balke, and S. Cramm, *J. Phys. D: Appl. Phys.* **40**, 1552 (2007).
- [58] C. T. Chen, Y. U. Idzerda, H. J. Lin, N.V. Smith, G. Meigs, E. Chaban, G. H. Ho, E. Pellegrin, and F. Sette, *Phys. Rev. Lett.* **75**, 152 (1995).
- [59] A. Thomson *et al.*: X-ray Data Booklet, Lawrence Berkeley National Laboratory, 2009, <http://xdb.lbl.gov>
- [60] J. Stöhr, *J. Elect. Spect. Rel. Phen.* **75**, 253 (1995).
- [61] A. Scherz, PhD thesis, Freie Universität Berlin (2004).
- [62] J. Kuneš and P. M. Oppeneer, *Phys. Rev. B* **67**, 024431 (2003)
- [63] A. A. Freeman, K. W. Edmonds, G. van der Laan, N. R. S. Farley, T. K. Johal, E. Arenholz, R. P. Campion, C. T. Foxon, and B. L. Gallagher, *Phys. Rev. B* **73**, 233303 (2006)
- [64] E. Arenholz, G. van der Laan, A. McClure, and Y. Idzerda, *Phys. Rev. B* **82**, 180405(R) (2010).
- [65] Richard M. Martin, *Electronic Structure*, Cambridge University Press, Cambridge 2004.
- [66] P. Hohenberg and W. Kohn, *Phys. Rev.* **136**, B864 (1964).
- [67] W. Kohn and L. J. Sham, *Phys. Rev.* **140**, A1133 (1965).
- [68] J. P. Perdew and Y. Wang, *Phys. Rev. B*, **45**, 13244 (1992).
- [69] J. P. Perdew, K. Burke, and M. Ernzerhof, *Phys. Rev. Lett.* **77**, 3865 (1996).
- [70] <http://elk.sourceforge.net>
- [71] G. K. H. Madsen, P. Blaha, K. Schwarz, E. Sjöstedt, and L. Nordström *Phys. Rev. B* **64**, 195134 (2001).
- [72] H. Ebert, D. Ködderitzsch, and J. Minar, *Rep. Prog. Phys.* **74**, 096501 (2011).
- [73] P. Mavropoulos and N. Papanikolaou, The Korringa-Kohn-Rostoker (KKR) Green Function Method I. Electronic structure of Periodic Systems, in *Computational Nanoscience: Do It Yourself!*, J. Grotendorst, S. Blügel, D. Marx (Eds.), John von Neumann Institute for Computing, Jülich, NIC Series, Vol. 31, pp. 131-158, 2006.
- [74] P. Lloyd and P. V. Smith, *Adv. Phys.* **21**, 69 (1972).
- [75] R. Zeller, *J. Phys.: Condens. Matter* **20**, 035220 (2008).

- [76] A. I. Liechtenstein, M. I. Katsnelson, V. P. Antropov, and V. A. Gubanov, *J. Magn. Magn. Mater.* **67**, 65 (1987).
- [77] P. W. Anderson, Theory of magnetic exchange interactions: exchange in insulators and semiconductors *Solid State Physics* vol 14, ed F Seitz and D Turnbull (New York: Academic), 1963, pp 99–214.
- [78] S. Majumdar, M. K. Chattopadhyay, V. K. Sharma, K. J. S. Sokhey, S. B. Roy, and P. Chaddah, *Phys. Rev. B* **72**, 012417 (2005).
- [79] K. R. Kumar, N. H. Kumar, G. Markandeyulu, J. A. Chelvane, V. Neu, and P. D. Babu, *J. Magn. Magn. Mater.* **320**, 2737 (2008).
- [80] J. Thoene, S. Chadov, G. Fecher, C. Felser, and J. Kübler, *J. Phys. D: Appl. Phys.* **42**, 084013 (2009).
- [81] H. Rathgen and M. I. Katsnelson, *Physica Scripta* **T109**, 170 (2004).
- [82] J. J. Rehr, J. J. Kas, F. D. Vila, M. P. Prange, and K. Jorissen, *Phys. Chem. Chem. Phys.* **12**, 5503 (2010).
- [83] J. Schwitalla and H. Ebert, *Phys. Rev. Lett.* **80**, 4586 (1998).
- [84] A. L. Ankudinov, A. I. Nesvizhskii, and J. J. Rehr, *Phys. Rev. B* **67**, 115120 (2003).
- [85] H. Wende, A. Scherz, C. Sorg, K. Baberschke, E. K. U. Gross, H. Appel, K. Burke, J. Minar, H. Ebert, A. L. Ankudinov, and J. J. Rehr, *AIP Conf. Proc.* **882**, 78 (2007).
- [86] R. Laskowski and P. Blaha, *Phys. Rev. B* **82**, 205104 (2010).
- [87] H. Luo, Z. Zhu, L. Ma, S. Xu, X. Zhu, C. Jiang, H. Xu, and G. Wu, *J. Phys. D: Appl. Phys.* **41**, 055010 (2008).
- [88] J. Barth *et al.*, *Phys. Rev. B* **81**, 064404 (2010).
- [89] T. Graf, J. Barth, B. Balke, S. Populoh, A. Weidenkaff, and C. Felser, *Scripta Materialia* **63**, 925 (2010).
- [90] J. Ruzs, L. Bergqvist, J. Kudrnovský, and I. Turek *Phys. Rev. B* **73**, 214412 (2006).
- [91] S. Picozzi, A. Continenza, and A. J. Freeman, *Phys. Rev. B* **66**, 094421 (2002).
- [92] Y. Kurtulus, R. Dronskowski, G. D. Samolyuk, and V. P. Antropov, *Phys. Rev. B* **71**, 014425 (2005).
- [93] E. Şaşıoğlu, L. M. Sandratskii, and P. Bruno, *Phys. Rev. B* **71**, 214412 (2005).
- [94] E. Şaşıoğlu, L. M. Sandratskii, and P. Bruno, *Phys. Rev. B* **77**, 064417 (2008).

-
- [95] T. Kanomata, K. Shirakawa, and T. Kaneko *J. Magn. Magn. Mater.* **65**, 76 (1987).
- [96] J. Kübler, G. H. Fecher, and C. Felser, *Phys. Rev. B* **76**, 024414 (2007).
- [97] C. M. Fang, G. A. de Wijs, and R. A. de Groot, *J. Appl. Phys.* **91**, 8340 (2002).
- [98] L. Castelliz, *Z. Metallkde.* **46**, 198 (1955).
- [99] H. Yamada, K. Terao, K. Kondo, and T. Goto, *J. Phys.: Condens. Matter* **2002**, 11785 (2002).
- [100] S. Ishida, S. Akazawa, Y. Jubo, J. Ishida, *J. Phys. F: Meth. Phys.* **12**, 1111 (1982).
- [101] P. Mohn, P. Blaha, K. Schwarz, *J. Magn. Magn. Mater.* **140-144**, 1, 183-184 (1995).
- [102] S.C. Lee, T.D. Lee, P. Blaha, K. Schwarz, *J. Appl. Phys.* **97**, 10C307 (2005).
- [103] M. C. Hickey, A. Husmann, S. N. Holmes, G. A. C. Jones, *J. Phys.: Condens. Matter* **19**, 2897-2903 (2006).
- [104] M. Meinert, J. M. Schmalhorst, and G. Reiss, *Appl. Phys. Lett.* **97**, 012501 (2010).
- [105] P. J. Webster and K. R. A. Ziebeck, *J. Phys. Chem. Solids* **34**, 1647 (1973).
- [106] V. Sharma, A. K. Solanki, and A. Kashyap, *J. Magn. Magn. Mater.* **322**, 2922 (2010).
- [107] P. Gupta, K. J. S. Sokhey, S. Rai, R. J. Choudhary, D. M. Phase, and G. S. Lodha, *Thin Solid Films* **517**, 3650 (2009).
- [108] E. Suharyadi, T. Hori, K. Mibu, M. Seto, S. Kitao, T. Mitsui, and Y. Yoda, *J. Magn. Magn. Mater.* **322**, 158 (2010).
- [109] E. Arenholz and S. Prestemon, *Rev. Sci. Instrum.* **76**, 083908 (2005).
- [110] J. A. Thornton, *J. Vac. Sci. Technol.* **11**, 666 (1974).
- [111] B. Balke, private communication.
- [112] R. Brydson, H. Sauer, W. Engel, J. M. Thomass, E. Zeitler, N. Kosugi, and H. Kuroda, *J. Phys.: Cond. Matt.* **1**, 797 (1989).
- [113] P. Klaer, M. Kallmayer, C. G. F. Blum, T. Graf, J. Barth, B. Balke, G. H. Fecher, C. Felser, and H. J. Elmers, *Phys. Rev. B* **80**, 144405 (2009).
- [114] A. Yamasaki, S. Imada, R. Arai, H. Utsunomiya, S. Suga, T. Muro, Y. Saitoh, T. Kanomata, and S. Ishida, *Phys. Rev. B* **65**, 104410 (2002).

- [115] A. Scherz, H. Wende, and K. Baberschke, *Appl. Phys. A* **78**, 843 (2004).
- [116] L. V. Bekenov, V. N. Antonov, A. P. Shpak, and A. N. Yaresko, *Condens. Matter Phys.* **8**, 565 (2005).
- [117] K. R. A. Ziebeck and P. J. Webster, *J. Phys. Chem. Solids* **35**, 1 (1974).
- [118] T. Kanomata, Y. Chieda, K. Endo, H. Okada, M. Nagasako, K. Kobayashi, R. Kainuma, R. Y. Umetsu, H. Takahashi, Y. Furutani, H. Nishihara, K. Abe, Y. Miura, and M. Shirai, *Phys. Rev. B* **82**, 144415 (2010).
- [119] T. Kubota, K. Kodama, T. Nakamura, Y. Sakuraba, M. Oogane, K. Takanashi, and Y. Ando, *Appl. Phys. Lett.* **95**, 222503 (2009).
- [120] P. Klaer, E. A. Jorge, M. Jourdan, W. H. Wang, H. Sukegawa, K. Inomata, and H. J. Elmers, *Phys. Rev. B* **82**, 024418 (2010).
- [121] M. P. Raphael, B. Ravel, Q. Huang, M. A. Willard, S. F. Cheng, B. N. Das, R. M. Stroud, K. M. Bussmann, J. H. Claassen, and V. G. Harris, *Phys. Rev. B* **66**, 104429 (2002).
- [122] B. Ravel, J. O. Cross, M. P. Raphael, V. G. Harris, R. Ramesh, and V. Saraf, *Appl. Phys. Lett.* **81**, 2812 (2002).
- [123] T. M. Nakatani, A. Rajanikanth, Z. Gercsi, Y. K. Takahashi, K. Inomata, and K. Hono, *J. Appl. Phys.* **102**, 033916 (2007).
- [124] K. Inomata, M. Wojcik, E. Jedryka, N. Ikeda, N. Tezuka, *Phys. Rev. B* **77**, 214425 (2008).
- [125] S. Picozzi, A. Continenza, and A. J. Freeman, *Phys. Rev. B* **69**, 094423 (2004).
- [126] K. Özdoğan, E. Şaşıoğlu, B. Aktaş, and I. Galanakis, *Phys. Rev. B* **74**, 172412 (2006).
- [127] I. Galanakis, K. Özdoğan, B. Aktaş, and E. Şaşıoğlu, *Appl. Phys. Lett.* **89**, 042502 (2006).
- [128] M. J. Carey, T. Block, and B. A. Gurney, *Appl. Phys. Lett.* **85**, 4442 (2004).
- [129] H. C. Kandpal, V. Ksenofontov, M. Wojcik, R. Seshadri, and C. Felser, *J. Phys. D: Appl. Phys.* **40**, 1587 (2007).
- [130] O. Rader, C. Pampuch, W. Gudat, A. Dallmeyer, C. Carbone, and W. Eberhardt, *Europhys. Lett.* **46**, 231 (1999).
- [131] H. C. Kandpal, G. H. Fecher, and C. Felser, *J. Phys. D: Appl. Phys.* **40**, 1507 (2007).

- [132] L. Vegard, *Zeitschrift für Physik* **5**, 17 (1921).
- [133] Y. Takamura, R. Nakane, and S. Sugahara, *J. Appl. Phys.* **105**, 07B109 (2009).
- [134] N. D. Telling *et al.*, *Phys. Rev. B* **78**, 184438 (2008); the corresponding spin magnetic moments are $m_{\text{Co}}^{\text{CMS}} = 0.89 \mu_{\text{B}}$, $m_{\text{Mn}}^{\text{CMS}} = 2.42 \mu_{\text{B}}$, $m_{\text{Co}}^{\text{CMA}} = 0.59 \mu_{\text{B}}$, $m_{\text{Mn}}^{\text{CMA}} = 1.91 \mu_{\text{B}}$. Errors of $\pm 10\%$ were assumed for these values. N. D. Telling, private communication.
- [135] H. A. Dürr, G. van der Laan, D. Spanke, F. U. Hillebrecht, and N. B. Brookes, *Phys. Rev. B* **56**, 8156 (1997).
- [136] A. Scherz, H. Wende, K. Baberschke, J. Minar, D. Benea, and H. Ebert, *Phys. Rev. B* **66**, 184401 (2002).
- [137] L. Pardini, V. Bellini, and F. Manghi, *J. Phys.: Condens. Matter* **23**, 215601 (2011).

Acknowledgements

My supervisors PROF. DR. GÜNTER REISS and DR. JAN SCHMALHORST deserve my first and deepest gratitude. It was them who offered me the opportunity to work with a new, state-of-the-art thin film deposition tool, and it was them who gave me the freedom to become what I call a “computationist”. I am thankful for many discussions, advices, for their support, and their faith in me. I thank JAN for XMCD sum rule analysis and for the many good beamtimes at the Advanced Light Source.

I am obliged to my colleagues from THIN FILMS AND PHYSICS OF NANOSTRUCTURES - D2. In particular, I thank DR. KARSTEN ROTT for his many lessons in vacuum technology and for keeping the lab equipment alive, DR. DANIEL EBKE for many helpful discussions, PETER HEDWIG for typographic advice and lessons on noise, and AGGI WINDMANN for helping me many times with the wheels of bureaucracy. I would like to express my thanks to my students HENDRIK WULFMEIER, CHRISTOPH KLEWE, CHRISTIAN STERWERF, and to the colleagues in my office, for just having a good time with them and for their support.

I am indebted for the financial support of my work by the German Bundesministerium für Bildung und Forschung (BMBF) and the Deutsche Forschungsgemeinschaft (DFG).

I thank for the opportunity to work at BL 6.3.1 and BL 4.0.2 of the Advanced Light Source, Berkeley, USA. In particular, I am very thankful for the many occasions to work and discuss with DR. ELKE ARENHOLZ.

Further, I thank DR. TANJA GRAF and TIM BÖHNERT for conducting the SQUID measurements on various samples.

Special thanks go to the developers of the DFT codes I have used for my work. Without their effort to make modern methods of DFT accessible to us experimentalists, a work like this would not have been possible. In particular, I would like to express my thanks to the group of PROF. HUBERT EBERT, and I thank them for introducing me to the SPRKKR package and to DFT in general with their workshop in Munich in June 2009. Very special thanks go to the developers of the Elk code, DR. JOHN KAY DEWHURST and DR. SANGEETA SHARMA. I thank them for bringing me closer to its maths and algorithms with the hands-on course in Lausanne in July 2011.

And finally, I am truly indebted and thankful to my girlfriend and best friend *Julia Bullik*, who supported me during all those years of my work.